

NASA Technical Memorandum 58208

The Skylab S191 Spectrometer Experiment
Analysis of Data and Their Applications
to the Earth Sciences

V. R. Wilmarth, D. A. Rainey, and W. R. Johnson

JULY 1978

NASA

PROPERTY OF NORTHROP UNIVERSITY.

NASA Technical Memorandum 58208

The Skylab S191 Spectrometer Experiment

Analysis of Data and Their Applications
to the Earth Sciences

V. R. Wilmarth
Lyndon B. Johnson Space Center
Houston, Texas

D. A. Rainey and W. R. Johnson
Lockheed Electronics Company
Houston, Texas

NASA

National Aeronautics
and Space Administration

**Scientific and Technical
Information Office**

1978

CONTENTS

Section	Page
<u>SUMMARY</u>	1
<u>INTRODUCTION</u>	2
<u>ANALYTICAL TECHNIQUES</u>	5
<u>DATA ANALYSIS</u>	6
ANGULAR DEPENDENCE OF OBSERVATIONS	8
S191 VERSUS S192 RADIANCE DATA COMPARISON	9
<u>THEORY AND ANALYSIS</u>	11
AEROSOL MODELS AND PHASE FUNCTION	11
EXACT SOLUTION	13
Doubling Method	14
Composition of Functions for Two Atmospheric Layers	17
Lambert Ground Reflectance	17
Discussion of Solutions	18
ANALYSIS AND RESULTS	19
<u>CONCLUSIONS</u>	22
<u>APPENDIX - THE TWO-STREAM APPROXIMATION</u>	71
<u>REFERENCES</u>	78

TABLES

Table		Page
I	S192 MULTISPECTRAL SCANNER PARAMETERS	23
II	DATA COLLECTED OVER NEW MEXICO AND ARIZONA	
	(a) EREP 20, White Sands, N. Mex., Aug. 12, 1973	24
	(b) EREP 27, Phoenix, Ariz., Sept. 6, 1973	25
III	SCENE DIMENSIONS AND PRECIPITABLE WATER PROFILE AT PHOENIX, ARIZONA, ON SEPTEMBER 6, 1973	26
IV	FSS AND S191 SCAN ANALYSES AS A FUNCTION OF ALTITUDE	27
V	FSS SCAN ANALYSIS FOR THREE PHOENIX SITES	28
VI	LINEAR COMPARABILITY OF TWO SITE SPECTRA	29
VII	GEOMETRICAL PARAMETERS FOR THE CURVES PRESENTED IN FIGURE 40	30

FIGURES

Figure		Page
1	S190A photograph (SL3-28-197) of lava bed near White Sands taken on August 12, 1973. Dashed line specifies S192 swath	31
2	RC8 aircraft photograph (mission 238, frame 74-0064) of lava site targeted by S191 during EREP 20 pass. Circle indicates S191 spatial resolution	32
3	RC8 aircraft photograph (mission 238, frame 74-0074) of gypsum sites. Dashed line outlines gypsum 1 and gypsum 2 as targeted by S191 VTS. Circle indicates S191 spatial resolution	33
4	S190A photograph (SL3-34-243) of Phoenix region taken on September 6, 1973. Dashed lines specify S192 swath	34
5	RC8 aircraft photograph (mission 247, frame 123-0037) of Rainbow Valley. Dashed circle outlines site as targeted by S191 VTS during EREP 27 pass. Solid circles indicate spatial resolution of the S191 and the FSS data at 1524 meters (5000 feet). (GT = location of ground-truth team, digits = location of FSS data acquisition at altitude)	35
6	RC8 aircraft photograph (mission 247, frame 123-0016) of Wittman as targeted by S191 VTS and the FSS. Circles indicate spatial resolution of S191 and FSS data taken at 1524 meters (5000 feet)	36
7	RC8 aircraft photograph (mission 247, frame 123-0055) of Old Verde Canal as targeted by S191 VTS and the FSS. Circles indicate spatial resolution of S191 and FSS data taken at 1524 meters (5000 feet)	37
8	Vinten (helicopter) photograph (mission 252, frame 003-080) of Rainbow Valley as targeted by the FSS from an altitude of 3658 meters (12 000 feet). Dashed circle outlines FSS FOV	38

9	Spectral profiles of radiance recorded by the FSS at altitudes of 1524 meters (5000 feet) and 3658 meters (12 000 feet) over Rainbow Valley on September 6, 1973. Letters A through M designate wavelengths of absorption bands of atmospheric gases. Circles show spectral resolution within the specified wavelength limits	39
10	Spectral profiles of radiance recorded by the FSS at an altitude of 1524 meters (5000 feet) and by the S191 over Rainbow Valley. (Absorption bands are defined in fig. 9.)	40
11	Spectral profiles of radiance recorded by the FSS at altitudes of 1524 meters (5000 feet) and 3048 meters (10 000 feet) over Wittman on September 6, 1973. (Absorption bands are defined in fig. 9.)	41
12	Spectral profiles of radiance recorded by the FSS at an altitude of 1524 meters (5000 feet) and by the S191 over Wittman. (Absorption bands are defined in fig. 9.)	42
13	Spectral profiles of radiance recorded by the FSS at altitudes of 1524 meters (5000 feet) and 3658 meters (12 000 feet) over Old Verde Canal. (Absorption bands are defined in fig. 9.)	43
14	Spectral profiles of radiance recorded by the FSS at an altitude of 1524 meters (5000 feet) and by the S191 over Old Verde Canal. The intersect diagram is composed of the S192 mean radiance value with standard deviations and one-half power spectral response wavelength limits. (Absorption bands are defined in fig. 9.)	44
15	Spectral profiles of radiance recorded by the S191 targeting lava (basalt) near White Sands at 14:45:37.66 UT (solid line) and 14:46:20.60 UT (dashed line). The intersect diagram is composed of the S192 mean radiance value with standard deviations and one-half power spectral response wavelength limits. (Absorption bands are defined in fig. 9.)	45
16	Spectral profile of radiance recorded by the S191 targeting desert near White Sands at 14:46:36.47 UT. (Absorption bands are defined in fig. 9.)	46

Figure	Page
17	Spectral profiles of radiance recorded by the S191 targeting gypsum 1 near White Sands at 14:47:02.60 UT and gypsum 2 at 14:47:06.33 UT. (Absorption bands are defined in fig. 9.) 47
18	Temporal comparison of the scale factor and the standard error of correlation (r^2) of consecutive S191 scans for Rainbow Valley. The dot-dashed line represents the computed scale values and the solid line is the scale trend or slope change line 48
19	The standard error of correlation between S191 and FSS data taken at an altitude of 1524 meters (5000 feet). The plotted values result from cumulative computations for data with wavelengths less than or equal to the abscissa value 49
20	Lava (basalt) at White Sands from 14:45:33.0 to 14:46:22.47 UT on EREP 20.
	(a) Angular geometry with the spacecraft at the origin. Radial measure is look angle and angular measure is azimuth difference. Plot begins at "S" with 10-second intervals . . . 50
	(b) Change of 0.7 micrometer radiance with time (Line = five-scan average) 50
21	Desert at Rainbow Valley from 21:23:47.56 to 21:24:31.38 UT on EREP 27. Plot format same as figure 20 51
22	S192 composite imagery of lava beds during EREP 20 (bands 20, 19, and 11) at White Sands. Distortion of image is due to conic scans presented as straight lines. Dashed square outlines area shown in enlarged photograph in figure 24 52
23	S192 composite imagery during EREP 27 (bands 5, 7, and 9) at Phoenix. Distortion of image is due to conic scans presented as straight lines. Solid lines outline area of pixel sampling 53
24	S192 enhanced and enlarged composite image of lava flow (bands 7, 9, and 19). Solid lines outline area of pixel sampling and S191 targeting 54

Figure	Page	
25	Comparison of S192 and S191 data by computation of band mean intensity. Data taken from observations of lava at White Sands. Wavelengths are scaled according to wave number	55
26	Typical phase function for continental haze with particle refractive index of 1.55 ($\lambda \leq 0.75$ micrometer) and 1.539 ($0.75 < \lambda \leq 1.0$ micrometer)	56
27	Example of single-scattering albedo values used in computations	57
28	Intensity of transmitted light in units of $\mu_0 K_0$ for plane containing the azimuthal differences, $\phi - \phi_0 = 0^\circ$ (forward scattering) and $\phi - \phi_0 = 180^\circ$ (backscattering). Plotted are values corresponding to two different solar zenith angles, θ_0 . The zero ordinate for $\theta_0 = 30^\circ$ is shifted downward for clarity	58
29	Intensity of reflected light in units of $\mu_0 K_0$ for planes $\phi - \phi_0 = 0^\circ$ (forward scattering) and $\phi - \phi_0 = 180^\circ$ (backscattering). Plotted are values corresponding to two different solar zenith angles, θ_0 . The zero ordinate for $\theta_0 = 30^\circ$ is shifted downward for clarity	59
30	Reflected intensity for an aerosol of optical depth, $\tau_a = 0.2$ (solid line), compared to that for a composite atmosphere of total optical depth, $\tau = 0.2$ (dot-dashed line); i.e., the layer is composed of a molecular layer ($\tau_r = 0.1$) and an aerosol layer ($\tau_a = 0.1$)	60
31	Fraction of incident flux, πK , reflected for three atmosphere-ground systems. Note the effect of layer composition and varying ground reflectances (numbers on curves)	61
32	Computed flux of transmitted and reflected energy for three solar zenith angles, θ_0 , for wavelengths 0.4 to 1.0 micrometer	62
33	Measured aerosol optical depths at Phoenix and White Sands for wavelengths from 0.4 to 1.0 micrometer	63

Figure		Page
34	Example of values of absorption optical depth used in model computations	64
35	Reflectances for the White Sands sites computed from S191 data. The dot-dashed curve is the measured reflectance for gypsum (ref. 16)	65
36	Time plot of computed surface reflectances from S191 targeting at Rainbow Valley	66
37	Reflectances for Phoenix sites computed from S191 data	67
38	Time plot of S191 radiance values recorded at 0.7 micrometer at Rainbow Valley and radiance values computed from models.	
	(a) Time plot of radiance values	68
	(b) Radiance values computed from model with ground reflectance of 0.36 and model with ground reflectance of 0.27 plus look angle effect	68
39	Spectral profiles for lava, desert, and gypsum (ref. 16).	69
40	Comparison of reflectances for Rainbow Valley (RBV) and Wittman (WTT) sites. Computations were made using S191 and FSS data taken at 1524 meters (5000 feet)	70
41	Two-stream model for helicopter spectrometer	76
42	Two-stream model for spacecraft spectrometer	77

SUMMARY

This report is a review of a study specifically initiated to review the quality of the data from the Skylab experiment S191. Experiment S191 was an infrared spectrometer designed to measure reflected and emitted radiation from a selected target.

Measurements were effected by manual operation of a viewfinder telescope to locate and "track" a target. Automatic spectral scanning (by a rotating filter wheel) at intervals of approximately 1 second provided a virtually continuous stream of observations. With changing spacecraft position, continuous sampling provided data for studying effects of changing the look angle while maintaining a relatively constant Sun angle for a variety of targets at White Sands, New Mexico, and Phoenix, Arizona, in 1973 where ground-truth teams made observations of pertinent phenomena.

The data were analyzed by two approaches. Data were first compared to one another to determine (1) whether there appeared any spurious departure from the "norm" for a particular scene (repeatability among scans), (2) whether there was any dependence shown in the data of the effects of changing the look angle, and (3) how the S191 data compared to radiometer data measured concurrently.

The second part of the analysis was a comparison to theoretical models. This approach was used not to validate models but to compare S191 data characteristics to known radiative transfer phenomena and to remove atmospheric effects. By this approach it was possible, for example, to determine that the assumption of Lambertian reflectance characteristics for the ground is generally inadequate.

The shortwave data studied were judged to be of good quality insofar as they represented measurements of the spectrum at a given target. Comparisons to spectra measured independently (and where available) were quite good even though there was no certainty about the effects of the atmosphere. Near-infrared and thermal data were not studied because there was no effort to measure near-infrared ground truth and the thermal data were unreliable.

Some potential uses for a spectrometer with operating characteristics similar to those of the S191 were reviewed. Among these were (1) intelligent selection at optimum wavelengths for use in future remote-sensing applications and (2) possible remote determination of optical depth (and, consequently, haze particle size distribution).

INTRODUCTION

Study of radiative transfer processes in the Earth's atmosphere has been conducted with data collected by balloon, aircraft, and spacecraft sensor systems. In the Skylab Program, the Earth Resources Experiment Package (EREP) contained the S191 infrared spectrometer, which was operated by the Skylab crewmen to obtain data from selected scenes and phenomena for experiments designed to determine the distribution of atmospheric constituents with altitude and the effects of the constituents on the transfer and attenuation of radiant energy and computer-processed multispectral scanner data.

Manual acquisition and tracking of targets by the Skylab crewmen permitted a unique flexibility and allowed for the intelligent selection of the "best" of a set of target choices. The S191 spectrometer had a 1-milliradian field of view (FOV) giving a scene diameter (at nadir) equal to 460 meters, tracking capabilities through angles of 45° forward to 24° backward and 20° left and right, and concurrent time-lapse photography of the scenes targeted. Spectral scanning was effected over two wide bands (0.4 to 2.5 micrometers and 6.0 to 15.5 micrometers) with one scan every 0.935 second.

This study was undertaken to determine the quality of the S191 data and to evaluate the potential use of S191 infrared spectrometers in the study of Earth phenomena and in resource surveys. The flight performance of the S191 sensor¹ has been reported by Hughes (ref. 1), Barnett,² and Potter (ref. 2).

Before the Skylab S191 experiment, the only spectrometer flown in space was the infrared interferometer spectrometer (IRIS), part of the Nimbus series of satellites. Measurements provided by IRIS were confined exclusively to the thermal region of the electromagnetic spectrum, whereas the S191 spectrometer provided thermal and visible-infrared observations, yielding a means of studying Earth spectra over a wide portion of the electromagnetic region.

The spectral resolution of the S191 is 0.0115 ± 0.0015 micrometer from a wavelength of 0.4 to 0.7 micrometer, 0.0185 ± 0.0040 micrometer from a wavelength of 0.7 to 1.4 micrometers, and increasing from 0.021 micrometer at a 1.4-micrometer wavelength to 0.0375 micrometer at a 2.5-micrometer wavelength.²

¹Richard D. Juday, Intricate Alignment and Timing Facts for S191 (in NASA Lyndon B. Johnson Space Center (JSC) memorandum dated Nov. 13, 1974).

²T. L. Barnett, Description of S191 Infrared Spectrometer and Discussion of the Sensor Products. NASA JSC Applied Physics Branch, Earth Observations Division, Jan. 18, 1974.

The data analyzed for this report were collected at test sites in Phoenix, Arizona, and White Sands, New Mexico, with the Skylab S191 spectrometer; the Skylab S192 multispectral scanner; the field spectrometer system (FSS), a modified S191 mounted in a helicopter; and ground-field surveys.

On August 12, 1973, and September 6, 1973, EREP data were acquired at White Sands (EREP pass 20) and at Phoenix (EREP pass 27), respectively. During each pass, ground-truth data were recorded by the Skylab Concentrated Atmospheric Radiation Project (SCARP) investigation teams at ground level and at several altitudes by helicopter with the FSS.

As Skylab approached each test site, the crewman operating the visual tracking system (VTS) of the S191 viewed forward 45° from nadir and began tracking a designated site, recording the spectral data, and filming the site. After approximately 45 seconds of data gathering for the first site, a second site was targeted and 12 seconds of data were obtained followed by approximately 15 seconds of data obtained at a third site. At White Sands, while targeting the third site (gypsum), a slight spacecraft roll caused the scene to shift alternately between gypsum deposits with two different spectral reflectances. Sufficient scans of each gypsum region, however, were acquired to permit an analysis. The position of the Sun during the EREP passes was different. On EREP 20 the early morning Sun was ahead and to the left of the spacecraft track, whereas on EREP 27 the afternoon Sun was directly behind the spacecraft. The significance of the wide range of Sun-target-sensor angles (solar reflection angles) is discussed in the section entitled "Angular Dependence of Observations."

Data obtained from Skylab EREP instruments over the two sites included the following:

1. Imagery data from the S190A multispectral photographic camera and the S190B Earth terrain camera (ETC)
2. S191 data on magnetic tape taken at approximately 1 scan per second
3. Data acquisition camera (DAC) film coverage of the S191 target taken at approximately 2 frames per second (black and white film)
4. S192 multispectral scanner system (MSS) data that provided measurements in 12 bands in the visible and near-infrared regions of the electromagnetic spectrum and in one band in the thermal region (table I).

Data from the helicopter were acquired by the FSS, with an FOV of 22° fixed to view at nadir. On the FSS, a Vinten camera with an FOV of 36° positioned to view at nadir acquired time-lapse photography coincident with the operation of the FSS. A mirror system implanted the mirror image of a clock on the film, allowing correlation of the FSS data with the photographed scene.

The White Sands area sensed by Skylab on EREP 20 is shown in figure 1. The sites targeted by the S191 sensor are the lava beds (A) and the desert (B). A third site in gypsum is off the photograph approximately

5 to 8 kilometers (3.1 to 5 miles) from the point designated "C." The S192 groundtrack covered only the lava bed. An aircraft photograph of the lava bed taken from an altitude of 6.6 kilometers (4.1 miles) shows the detailed surface features of the lava site targeted by the S191 (fig. 2). The area covered during the 48 seconds of S191 data acquisition is specified by the solid circle.

The two types of gypsum deposit data acquired by the S191 in the White Sands area are shown in an aircraft photograph (fig. 3) taken on June 14, 1973, 2 months earlier than the Skylab flight, at a time when a fog bank obscured the northern portion of White Sands. There was no fog at this site during S191 data acquisition, which is outlined with a dashed line in figure 3. Table II lists the data acquired for S191, FSS, and S192 for the White Sands sites.

A view from Skylab EREP pass 27 of the Phoenix, Arizona, area identifies the three S191 sites at Rainbow Valley (A), Wittman (B), and Old Verde Canal (C) (fig. 4). Helicopter FSS and Skylab S191 data were acquired for these three test sites. The left and right limits of the S192 swath are shown with dashed lines. Because of malfunctions, only 3 of the 13 bands of S192 data were recovered for the Old Verde Canal test site. A description of the data obtained for the Phoenix sites is presented in table II.

Aircraft photographs from a 6.5-kilometer (4 mile) elevation over Rainbow Valley, Wittman, and Old Verde Canal (figs. 5, 6, and 7) show the sites targeted by the S191. The spatial resolution of the S191 is indicated by solid circles, with the dashed line outlining the region over which the S191 target roamed during data acquisition. Also indicated are the locations where the FSS data were acquired. These locations are denoted as 5, 50, 90, and 120 for the flight altitudes of 152, 1524, 2750, and 3658 meters (500, 5000, 9000, and 12 000 feet).

The FSS data were taken over the sites as indicated, with the exception of the data acquired at a 3658-meter (12 000 foot) altitude at Rainbow Valley. In this case, the helicopter drifted north-northeast, and an agricultural area was included in the FSS scene photographed with the Vinten camera. This area is shown by the dashed line in figure 8.

The helicopter data consisted of tabulations of FSS radiance values acquired at the three Phoenix area sites. The data were recorded along four flight lines at each site, at four altitudes above the surface: 152, 1524, 2750, and 3658 meters (500, 5000, 9000, and 12 000 feet). At Wittman, the fourth altitude was 3048 meters (10 000 feet); the processed data at 152 meters (500 feet) over Wittman are missing. The Vinten camera product and crew flight log provided the link to ascertain the scene targeted by the FSS. Tabulations of processed FSS data did not include the entire span of the short-wavelength data. The missing spectral data were from 1.05 to 1.5 micrometers, which includes the water absorption band at 1.13 micrometers.

The objective of the SCARP experiment was to improve the understanding of radiation transfer within the Earth's atmosphere (ref. 3). Data from ground surveys and aircraft, from balloonborne instrumentation, and

from the EREP (S191, S192) were analyzed, with primary emphasis on determining the radiative transfer processes in a scattering atmosphere using a set of six modes. It was concluded that precise refractive index and optical depth values with good spectral resolution are critical to a proper determination of radiative transfer processes involving scattering media. As part of SCARP, a radiation transfer program was developed by Marlatt (ref. 4) using the S191 data. This investigation was continued and expanded to include analysis of the S191, S192, and FSS data, specifically in the 0.4- to 2.5-micrometer wavelength, to further the knowledge of the effects of atmospheric attenuation on radiation reflected from the Earth's surface and to assess the value of spectrometric data acquired on orbital platforms for Earth science. Results of this study are contained in this report. A secondary objective of this investigation was to develop techniques whereby Earth resources satellites can collect ground-truth data corrected for atmospheric effects. However, further study and experimentation is required before this goal can be achieved.

ANALYTICAL TECHNIQUES

The analytical approaches used in this study vary in sophistication, complexity, and accuracy. They are as follows:

1. A comparison of the target spectra taken at two or more levels to determine the degradation rate and gross effects due to the atmosphere.
2. A comparison of the target spectra taken at two or more angles to yield gross atmospheric effects directly.
3. A comparison of absolute radiance values taken with the S191 and S192 spectrometers to consider compatible bandwidths.

The S191 data were processed with the Control Data Corporation (CDC) Cyber 7000 series computer. The S192 data were imaged on the Aerojet Display Analysis System (DAS) to specify the location of those picture elements (pixels) representing the area targeted by the S191. The DAS processing provided histograms in each S192 band and provided statistical values which were directly converted to absolute radiance values. All radiative transfer functions including phase functions, reflection functions, and transmission and related functions were computed on the Cyber 7000 with only moderate total computer resource consumption. A large part of the final analysis was performed with the aid of a Hewlett-Packard programmable calculator (with printer), model HP-97.

The multispectral data from the S191, S192, and FSS have been analyzed and compared by directly plotting the tape data as a measure of the data quality, by assessing the effects of the look angle on the spectral quality, and by comparing the radiance values of selected frequencies for the S191 and S192 data.

DATA ANALYSIS

Direct plotting of the data from the S191 and FSS magnetic tapes gives the first visible evidence of the data quality (figs. 9 to 17). The profiles from the FSS spectral intensities recorded at the four altitudes of observation for the three Phoenix sites at Rainbow Valley, Wittman, and Old Verde Canal are shown in figures 9, 11, and 13. The consistency of repetition is evident. The major water vapor absorption bands at 0.942, 1.135, 1.400, 1.87, and 2.5 micrometers (indicated by arrows lettered E, F, H, I, and M, respectively) were dominant features in all the profiles where data were available. Less dominant but still apparent features included the oxygen bands at 0.762 and 0.690 micrometers and the weak water vapor absorption band at 0.823 micrometer (arrows C, A, and D, respectively). The weak water vapor band at 0.723 micrometer (arrow B) was not always apparent.

An anomaly in the FSS profiles appears at about 0.69 micrometer and is the result of a change in filter segment calibration functions at a filter wheel segment boundary. This problem appeared uniformly as a jump upward in the data. The data below 0.5 micrometer were considered of very poor quality. Data between 1.04 and 1.4 micrometers were also missing because of processing problems.

Examination of the S191 plots superimposed on the FSS plots (figs. 10, 12, and 14) reveals that all absorption features observed in the FSS data are also recorded in the S191 data. The overall appearance of the spectra from both instruments indicates good repeatability of sensor performance.

The predominant absorption phenomena in the interval 0.4 to 1.0 micrometer are due to water vapor. Although minor concentrations of oxygen, methane, carbon dioxide, and other gases may be present, they showed no strong absorption in this interval but were detected at wavelengths beyond 1.0 micrometer. The optical depth measurements from the SCARP provided the data on the atmospheric constituents.

A technique developed by Pitts (ref. 5) was used to ascertain its application to spectral data for the determination of the total atmospheric water vapor content in a vertical column of the atmosphere (i.e., precipitable water content). The method evaluated atmospheric water vapor by determining the strength of the 0.96-micrometer water vapor absorption band. One sample calculation made for the Phoenix sites yielded 3.08 centimeters of precipitable water compared to 3.10 centimeters derived from the radiosonde data.

One absorption feature present to some degree in both FSS and S191 spectra appeared at approximately 1.58 micrometer; however, the ground or atmospheric constituent whose absorption properties correspond to this feature was not determined.

Some variations in spectral comparisons between FSS and S191 data arose as a result of instrument differences and altitude differences. The functional differences in the two instruments were the FOV and the FSS

look angle, which was fixed at nadir, whereas the S191 had a 1-milliradian FOV and was manually aimed by the crewmen to look in any direction. The helicopter-mounted spectrometer FOV was 22°.

The effective diameters (viewed with a nadir-aimed VTS camera) of the scene subtended by the spectrometer aperture are listed in table III. The scene of the FSS at 1524 meters (5000 feet) in altitude most closely approximates the scene of the S191.

The observations made with the FSS included contamination from skylight and earthlight, which gave a misrepresentation of the data as a measure of radiance observed in a small-resolution solid angle. The errors introduced by the larger FOV of the S191 were small, by virtue of the relatively small optical depths of the increment of atmosphere lying below the helicopter. The effect of the small FOV of the FSS was illustrated at the Rainbow Valley site when the FSS scene, at an altitude of 3658 meters (12 000 feet) with a diameter of 1420 meters (4659 feet), included some irrigated fields (figs. 5 and 8), which occluded approximately 20 percent of the scene. A characteristic rise in the FSS scan at 3658 meters (12 000 feet) as compared to 1524 meters (5000 feet) (fig. 9) appeared as a rather dramatic crossing of the latter curve.

One approach chosen to objectively compare the FSS and S191 spectral data required considering the data as a whole, not by comparison of individual wavelengths. The method and examples of its applicability, including linear regression and sequential scan analysis, are described in the following paragraphs.

Two scans can compare favorably if there is a consistent relationship between them. The simplest sort of relationship is linear. Suppose $I_1(\lambda)$ and $I_2(\lambda)$ are spectra that represent different parameter sets or scenes. That is, I_2 may have been observed later than I_1 , or I_2 may have been observed from a helicopter platform, I_1 from a spacecraft platform, etc. It is assumed that I_1 and I_2 compare linearly if $I_2(\lambda) \cong bI_1(\lambda) + a$ and if the standard error of the correlation r^2 varies by no more than an arbitrary fraction from unity, where b is a scale factor and a is a displacement term. The constants a and b are meaningless when r^2 does not satisfy the criterion established for it.

Because of a great volume of data, only a few combinations of scans were used in regression analysis. At each Phoenix site, a 1524-meter (5000 foot) FSS observation was used because the $I_1(\lambda)$ scene of the FSS at this altitude most nearly resembled the scene of the S191 spectrometer. Regression analysis was completed for each helicopter altitude for which there were data from each site (table IV). Included in this analysis was a scan from the S191 that was not necessarily concurrent, either geometrically or temporally, with the helicopter experiment.

Computations for comparison parameters were made among scans for the 1524-meter (5000 foot) data to examine consistency. The mean intensity for the interval 0.4 to 2.5 micrometers and the standard error of correlation (table V) show that there are only small deviations in mean values and that r^2 does not fall below 0.99 at any site for the data analyzed. It is noted that not all possible combinations have been analyzed and only

one scan at 1524 meters (5000 feet) was used as the reference scan I_1 for computations. If I_1 is erroneous and all r^2 satisfy comparability criteria, then there is a possibility that all the data are erroneous. The reference scans that were chosen satisfied other criteria such as consistency with theory and scene uniformity.

Another approach in comparing the FSS and S191 spectral data was to use the first scan analysis at the Rainbow Valley site as reference and compare as a function of time the intensity for every scan in the Rainbow Valley sequence (fig. 18). Correlation again remains high, never falling below a 0.98 value. The scale factor shows the effect of a change in the geometry of scattering by rising just above 1, then gradually falling off.

Collection of the S191 data was not, in general, concurrent with that of the FSS data although the observations over Wittman were made with a time difference of only 94 seconds. Differences in time of data collecting correspond to different geometries of scattering and, therefore, differences in the signature are expected. The values in table IV correlating S191 to FSS data are also altered by omission of data in the interval 1.1 to 1.38 micrometers because of missing or unreliable data from the FSS.

Figure 19 shows the standard error of correlation computed for a scan analysis of each site at Phoenix using S191 and 1524-meter (5000 feet) FSS intensities. As expected, correlations are low where short-wavelength scattering is dominant and high when more long-wavelength data are included. The rise in correlation occurs very fast between 0.6 and 1.0 micrometer. Linear regression analysis proved, in general, to be a reliable means of comparing data from the two scans. The reliability of comparisons between FSS and S191 data was slightly affected by problems with missing and dubious data. Data from the FSS and S191 were processed differently, and the selection of wavelengths for output products, in addition to problems with filter-wheel voltage to wavelength calibration,³ may be the cause of errors in this analysis. Wavelengths were selected for output for their "niceness" (i.e., small but equal steps, etc.). These values were interpolated from data passed through calibration functions resulting in shifting and smoothing - an unavoidable hazard of interpolation.

ANGULAR DEPENDENCE OF OBSERVATIONS

Checking the consistency of the functional relationship of observations to variations in look geometry can provide significant information about data quality. The results of a preliminary examination of the effect of angular dependence on the quality of data are discussed in the following paragraphs.

³T. L. Barnett, Description of S191 Infrared Spectrometer and Discussion of the Sensor Products. NASA JSC Applied Physics Branch, Earth Observations Division, Jan. 18, 1974.

Figures 20 and 21 illustrate the variation of the S191 observations over the lava site at White Sands and Rainbow Valley, respectively. At the lava site the target was observed with the Sun forward and to the left of the groundtrack (i.e., looking into the Sun). The morning Sun had a large zenith angle ($63^\circ \pm 1^\circ$) with an azimuthal deflection equal to $48^\circ \pm 5^\circ$. The large variations in the data are attributed to the wandering of the instrument reticle, which corresponds to changes in the scene. The S191 scene diameter (460 meters (1509 feet)) approximated the size of the darkest portion of the lava site. Studies of the S192 data for the lava site showed a 100-percent increase in reflected radiation from the darkest region to the surrounding lava.

In contrast to the lava site, figure 21 shows, in the same format, the data for the Rainbow Valley site where the Sun was relatively high ($36^\circ \pm 1^\circ$) and almost directly behind the spacecraft. Fluctuations in the data are small, compared to the signal, and may be attributed to combinations of sensor noise, "atmospheric" noise, and slight scene variation due to reticle wander. The variation in reflection angle passes through a minimum, a feature not visible in the graph of look angle data. Despite the appearance of the minimum in the reflection angle, there seems to be no corresponding feature in the time plot of the S191 data.

Figure 18 shows the results of the comparison of each spectrum in the set for Rainbow Valley to the first spectrum in this sequence of spectral scans. Shown in the graph are the scale factors and the r^2 values. In general, the scale factor in figure 18 contains few fluctuations concurrent to the data in figure 21. Meanwhile, the plotted values of r^2 do not vary downward from 0.99 by more than 0.01 percent. By previously defined criteria, this indicates good linear comparability.

S191 VERSUS S192 RADIANCE DATA COMPARISON

The EREP passes 20 and 27 provided concurrent spectral data of a target using two different remote sensors, the S192 multispectral scanner and the S191 spectrometer. The sites were the lava beds near White Sands and a desert region just north of the Old Verde Canal. Figures 22 and 23 are color composite images generated from three blends of S192 data for these sites. The distortion of the imagery is due to conical scan data presented as straight lines. The common sites of S191 and S192 data acquisition are designated by A in each image. An enhanced, enlarged image (fig. 24) of the lava-bed site reveals the black-ridge residual within the lava flow. The individual squares seen in the enlarged image are representative of the spatial resolution of the S192.

In the analysis of the S192 imagery, the area targeted by the S191 was isolated (fig. 24), and the pixel values were histogrammed in all available bands. The statistical means and the standard deviations of the pixel values were converted to absolute radiance values. The one-half power limits and peak power wavelength of the spectral response curve for

each band (table I) were taken from the EREP calibration document.⁴ The S192 radiance values (mean and standard deviation) and the one-half power wavelength limits compose the intersect diagram for each band and are plotted on figures 14 and 15, which contain the S191 spectral plot.

The radiance values from each sensor conform relatively well; differences may be due to different calibration procedures. The slight difference in scattering angles can be due to difference in site viewing angles. The target viewing conditions were different only in the precise time of data acquisition. S191 observations at the lava bed were terminated at 14:46:23 UT (viewing angle from nadir: 18.55°) with the S192 scanning the lava beds about 14:46:40 UT. The view angle of the scanning S192 is 5.6° from nadir. The S191 data at Old Verde Canal began at 21:25:04 UT (viewing angle from nadir: -3.97°) with the S192 scanning at 21:24:52 UT. The different look angles for the two instruments were 13° and 9.5°, respectively. For the examples given, the significance of the difference in viewing angles is important only in how the reflection angle is affected. In these two cases, the reflection angle change was about 10° from the time one sensor recorded data to the time the other sensor recorded data. Although the sensor geometries are quite similar at first glance, it is probable that some small discrepancy in the observations has been recorded.

Additional comparison of the S191 and the S192 data was accomplished by integrating the S191 data over the S192 bands according to

$$S_{\lambda} = \frac{\int_B I(\lambda)\phi_B(\lambda)d\lambda}{\int_B \phi_B(\lambda)d\lambda} \quad (1)$$

where $I(\lambda)$ is the S191 spectral data, $\phi_B(\lambda)$ is the S192 response function for a specific band, and S_{λ} represents the integral mean intensity over the band. Integration is effected over the band B. A graphic comparison of S_{λ} to the S192 data is given in figure 25.

Regression analysis for comparison was made using the S_{λ} and the S192 measurements at corresponding wavelengths for the lava site at White Sands. The standard error of correlation was found to be 0.9325 with a scale factor of $b = 0.9344$ and a displacement of $a = 0.00019$.

Because of the small sample of data taken at the Old Verde Canal site, no comparison was made for that site.

⁴S191 Infrared Spectrometer Experiment. Skylab Instrumentation Calibration Data. MSC-07744, vol. 4; NASA JSC internal document, April 1973.

THEORY AND ANALYSIS

The theoretical foundations of the analysis of the S191 are discussed in this section. Derivations of phase functions and their representations and subsequent use in solutions to the problem of radiation reflection and transmission in realistic atmospheres are reviewed.

AEROSOL MODELS AND PHASE FUNCTION

Distributions of aerosol particle size by radius were derived from theoretical functions to appropriately represent layer extinction. (The actual process was fairly subjective. The fit at White Sands, for example, was not very good for any distribution tried.) The aerosol at White Sands was assumed to be composed of suspended water droplets with radii smaller than 10 micrometers and distributed according to $n(r) = ar \exp(-b\sqrt{r})$, where a is an arbitrary constant. The constant $b = 8.944$ was derived by Diermendjian (ref. 6) for his "M" haze and is used in this study. This particular model was chosen for White Sands because it exhibited a peak in the aerosol optical depth at about 0.55 micrometer that corresponded to the aerosol optical depth measured at the site. This model proved to give a flat optical depth curve and for this reason is not to be considered, by any means, the most appropriate one.

The particle size distribution model for the Phoenix region was given by

$$n(r) = \begin{cases} ar^{-5}, & r > 0.10 \\ 10^5 a, & 0.03 < r < 0.10 \\ 0, & r \leq 0.3 \end{cases} \quad (2)$$

The Phoenix aerosol particles were assumed to be silicate spheres with radii smaller than 10 micrometers. This model proved to be the best for the Phoenix test sites, because computed optical depths concurred very well with those measured.

According to Chandrasekhar (ref. 7), the phase function is the distribution of the intensity of radiation that has been scattered once through an angle θ into a small cone or solid angle $d\Omega$. In discussing the solution to the Maxwell equations of the electromagnetic field, Van de Hulst (ref. 8) considers homogeneous spheres of complex refractive index $m = m_1 - m_2i$, where m_1 is the usual Snells law and m_2 is related to the absorbing power of the medium.

The first two components of the phase matrix (ref. 8) were computed according to

$$\frac{1}{4\pi} p_{\ell}(\theta, m) = \frac{1}{\beta_{sc}} \int_0^{\infty} n(r) i_{\ell}(\theta, m, r) dr, \quad \ell = 1, 2 \quad (3)$$

where

$$\beta_{sc} = \pi \int_0^{\infty} r^2 n(r) Q_{sca}(m, r) dr$$

The functions Q_{sca} and i_{ℓ} are computed after the methods of Diermendjian, Clasen, and Vizee (ref. 9). Because the polarization of radiation was not considered in this study, the phase function finally used was normalized from $(p_1 + p_2)/2$ so that

$$\frac{1}{4\pi} \int p(\cos \theta) d\omega = 1 \quad (4)$$

where the element of solid angle may be expressed by $d\omega = \sin \theta d\theta d\phi$. The angle θ is the zenith angle measured from the outward normal to a plane-parallel atmospheric layer, and ϕ is the azimuth measured from some fixed reference.

The phase function was expanded in a series of Legendre polynomials

$$p(\cos \theta) = 1 + \sum_{m=1}^N \omega_m P_m(\cos \theta) \quad (5)$$

This representation of the phase function can be further expanded in a Fourier series

$$p(\mu, \phi; \mu_0, \phi_0) = \sum_{m=0}^N (2 - \delta_{0,m}) \sum_{\ell=m}^N \omega \frac{(\ell - m)!}{\ell(\ell + m)!} P_m^\ell(\mu) P_m^\ell(\mu_0) \cos m(\phi - \phi_0) \quad (6)$$

where

$$\delta = \begin{cases} 1, & m = 0 \\ 0, & \text{otherwise} \end{cases}$$

The function $P_m^\ell(\mu)$ is the Legendre polynomial of the first kind, order ℓ degree m . (The m here should not be confused with the refractive index.) The geometry is given by a pair of incidence angles $(\mu_0 = \cos \theta_0, \phi_0)$ and a pair of angles associated with the scattered light $(\mu = \cos \theta, \phi)$. This notation is used in all discussions.

It should be noted that the phase function is not sensitive to the constant ω selected for the particle-size function. One phase function was computed for each wavelength in the study interval. The asymmetry factor $\omega_1/3\omega_0$ did not show much variability for either haze model, nor did the forward peak show any large variation. Thus, for practical purposes, a single "representative" phase function could suffice to describe the single-scattering properties of a light haze having a relatively small optical depth at all wavelengths. Figure 26 shows examples of phase functions for the Phoenix and White Sands sites.

EXACT SOLUTION

The exact solution to the equation of transfer (ref. 7) is designated the doubling method (ref. 10) and it has a long history of reliable application with well-documented accuracy limits. The algorithm involves computation of reflection and transmission functions for very thin initial layers; it is assumed that the phase function completely describes the scattering properties of the layers. Layers are doubled or combined repeatedly until the desired optical depth is obtained. Initial layers usually provide the best doubling results for thicker layers when calculations are made using initial optical depths of 2^{-25} or less.

For the haze model, it is assumed that the scattering layers are plane-parallel slabs and that incident light is an unpolarized plane wave of intensity πK per unit area oriented perpendicularly to the incident beam. Horizontal and vertical homogeneity are also assumed for the use of a single phase function. The absorption, which was considered to have been caused exclusively by water vapor, was confined to the aerosol layer because 90 percent of the water vapor depth was concentrated in the first 3660 meters (12 000 feet) of the atmosphere.

Doubling Method

Reflection and transmission of radiation by a plane-parallel layer of atmosphere with optical depth τ is given mathematically by

$$I(\tau = 0, \mu, \phi) = \mu_0 K R(\tau; \mu, \phi; \mu_0, \phi_0) \quad (7)$$

and

$$I(\tau = \tau_0, -\mu, \phi) = \mu_0 K T(\tau; \mu, \phi; \mu_0, \phi_0) \quad (8)$$

where $I(\tau = 0, \mu, \phi)$ is the specific intensity of radiation diffusely reflected from the top of the layer, and $I(\tau = \tau_0, -\mu, \phi)$ is the intensity of radiation transmitted to the bottom of the layer. The pairs of parameters, (μ, ϕ) and (μ_0, ϕ_0) , represent directions of reflection and incidence, respectively. The μ is a cosine of angle of incidence or reflection as measured from the outward normal to the layer (i.e., zenith angles). The ϕ is azimuth measured from a fixed reference in the plane of the layer. The functions R and T are reflection and transmission, respectively, whereby scattering is affected through an angle θ from (μ_0, ϕ_0) to (μ, ϕ) . The scattering angle θ is given by

$$\cos \theta = \mu \mu_0 + (1 - \mu_0^2)^{1/2} (1 - \mu^2)^{1/2} \cos (\phi - \phi_0)$$

The phase function (see section entitled "Aerosol Models and Phase Functions") was assumed to describe the reflection and transmission functions when the optical depth was sufficiently small that the intensity of light undergoing a single-scattering process predominated. Thus, computations begin by definition of the scattering functions (reflection and transmission)

for a specific phase function $p(\mu, \phi; \mu_0, \phi_0)$, optical depth $\tau_0 (\leq 2^{-25})$, and single-scattering albedo ω_0 by the expressions

$$R(\tau_0; \mu, \phi; \mu_0, \phi_0) = \frac{\omega_0}{4(\mu + \mu_0)} \left\{ 1 - \exp \left[-\tau_0 \left(\frac{1}{\mu} + \frac{1}{\mu_0} \right) \right] \right\} p(\mu, \phi; -\mu_0, \phi_0) \quad (9)$$

and

$$T(\tau_0; \mu, \phi, \mu_0, \phi_0) = \frac{\omega_0}{4(\mu - \mu_0)} \left[\exp(-\tau_0/\mu_0) - \exp(-\tau/\mu) \right] p(\mu; \phi; \mu_0, \phi_0) \quad (10)$$

In practice, the phase function expansion (eq. 6) is used, resulting in the generation of terms of a Fourier series so that the products of doubling are the functions of the zenith angles and the optical depth only. These functions can be combined in a Fourier series in cosines of the azimuth difference:

$$R(\tau; \mu, \phi; \mu_0, \phi_0) = \sum_{m=0}^{\infty} R^{(m)}(\tau, \mu, \mu_0) \cos m(\phi - \phi_0) \quad (11)$$

and

$$T(\tau; \mu, \phi; \mu_0, \phi_0) = \sum_{m=0}^{\infty} T^{(m)}(\tau, \mu, \mu_0) \cos m(\phi - \phi_0) \quad (12)$$

Using these functions to initiate the doubling (adding two atmospheric layers of the optical depth τ to obtain functions corresponding to one layer of optical depth 2τ), these functions can be generated, after repeated doubling, very accurately by comparison to other exact solutions.

After the approach of Lacis and Hansen (ref. 11), the algorithm is represented by a set of equations (with respect to the Fourier index m):

$$\left.
\begin{aligned}
Q_1 &= R_a \cdot R_b \\
Q_n &= Q_1 \cdot Q_{n-1}, \quad n \geq 2 \\
S &= \sum_{n=1}^{\infty} Q_n \\
D &= T_a + S \exp(-\tau_a/\mu_0) + S \cdot T_a U - R_b \exp(-\tau_a/\mu_0) + R_b \cdot D \\
R(\tau_a + \tau_b) &= R_a + U \exp(-\tau_a/\mu) + T_a \cdot U \\
T(\tau_a + \tau_b) &= D \exp(-\tau_b/\mu) + T \exp(-\tau_a/\mu_0) + T_b \cdot D
\end{aligned}
\right\} (13)$$

The subscripts a and b refer the R and T functions to the upper and lower layers, respectively. For all applications in this study, the layers were assumed to be homogeneous; therefore, there was no need to account for top and bottom illumination (except in the case of a composite atmosphere, which is discussed in the section entitled "Composition of Functions for Two Atmospheric Layers"). The dotted products in equation 13 are weighted integrals of the form

$$R_a \cdot R_b = (2 - \delta_{m,0}) \int_0^1 R_a(\mu, \mu') R_b(\mu', \mu_0) \mu' d\mu' \quad (14)$$

where

$$\delta_{m,0} = \begin{cases} 0, & m = 0 \\ 1, & \text{otherwise} \end{cases}$$

The sum S in equation 13 was terminated after four terms, and a geometric series (i.e., $Q_5(1 - \eta)^{-1}$ with $\eta = Q_5/Q_4$) was added as an error term.

Composition of Functions for Two Atmospheric Layers

Doubling was executed on atmospheric layers with Rayleigh and Mie phase functions to Rayleigh τ_r and aerosol τ_{ar} optical depths. The two layers were then combined using equation 13 with the Rayleigh layer associated with subscript a and the aerosol layer associated with subscript b. By this method, scattering functions were obtained for an atmospheric model composed of a Rayleigh (molecular) scattering layer overlying an aerosol layer. To obtain functions corresponding to the illumination of this same model atmosphere from below, the association of subscripts in equation 13 was reversed. These functions are required for completeness, because the underlying ground effectively illuminates the model atmosphere from below. In both cases (top versus bottom illumination), the single-scattering albedo for the Rayleigh layer was 1.0 and that for the bottom layer was a function of the wavelength (fig. 27).

Lambert Ground Reflectance

Estimation of the planetary albedo or the reflected field of radiation must include considerations about the effect of a ground surface lying below an atmospheric layer. Treatment must include computations to account for the way in which radiation reaches the ground and for the way in which it is reflected by the ground and transmitted to the sensor.

For the purposes of this study, the ground was assumed to reflect according to Lambert's law with albedo ρ , that is

$$I(\mu, \phi; \mu_0, \phi_0) = \mu_0 K \rho \quad (15)$$

This approach was used because of (1) a lack of bidirectional reflectance data for various surfaces that were directly related to this experiment and (2) no concurrent ground measurements.

Total reflectance at the top of the atmosphere is composed of skylight and attenuated earthlight given by

$$I(0, \mu, \phi) = \mu_0 K \left[R(\tau; \mu, \phi; \mu_0, \phi_0) + \frac{\rho}{1 + \rho S^*} \gamma_1^*(\mu) \gamma_1(\mu_0) \right] \quad (16)$$

where

$$\bar{s}^* = 4 \int_0^1 \mu \int_0^1 \mu' R^{*(0)}(\mu, \mu') d\mu' d\mu$$

$$\gamma_1(\mu) = \exp(-\tau/\mu) + 2 \int_0^1 T^{(0)}(\mu, \mu') \mu d\mu$$

The functions signified by asterisks refer to those functions for illumination from below. Note that the integrands are the zeroth terms in the Fourier series for the total functions. Additional reference may be made to Rainey and Marlatt (ref. 12) and Chandrasekhar (ref. 7) for further clarification of these expressions. The function $\gamma_1(\mu)$ represents the fraction of the total flux of incident radiation transmitted, both directly and diffusely, by the layer. The expression \bar{s}^* arises when light reflected from the ground is reflected by the sky back to the ground in the form of a flux. The first term in the braces (eq. 16) is the skylight or path radiance and the second term is the total contribution of earthlight.

Discussion of Solutions

Radiative transfer processes in light hazes are distinctly different from those involving clouds or optically thick scattering media. Transmitted light (fig. 28) retains the forward scattering feature instead of the trend toward isotropic scattering exemplified by transmission through optically thick clouds (e.g., stratus clouds) in which "skylight" appears to be uniformly distributed. Reflected light (fig. 29) behaves in a manner suggesting low-order scattering according to an anisotropic phase function.

Comparing the reflection function for a composite atmosphere (see section entitled "Composition of Functions for Two Atmospheric Layers") to the pure aerosol layer in figure 30, a profile suggesting low-order scattering is indicated. Raising of the left peak corresponds to additional Rayleigh scattering. The general rise in reflection values is due to the symmetry in Rayleigh's phase function. In general, these graphs indicate that transmitted light (at the bottom of a composite layer) displays haze characteristics more strongly than Rayleigh, whereas reflection shows a marked resemblance to Rayleigh reflection.

Reflected flux was computed for three cases (Rayleigh, aerosol, and composite), each having the same total optical depth. These calculations were performed using several Lambertian ground reflectances. The results of these calculations are presented in figure 31. For this example with optically thin layers, the effect of the atmosphere is diminished with increasing ground reflection - an effect that is also apparent for the

reflection function. Except for the grazing incidence (a large solar zenith angle), the reflected flux shows a minimum for the aerosol model when the Sun is at zenith with a totally absorbing ground. This feature is much diminished (but still visible) in the composite case.

Flux computations were also made according to the total optical depth (with single-scattering albedo) with the results displayed in figure 32. The transmitted and the reflected flux are illustrated. Note that total flux of radiation (reflected and transmitted) is equal to one only when single-scattering albedo is equal to one. Also note that the curves representing transmitted light include the flux of radiation directly transmitted through the layer undergoing no scattering.

The curves in figure 32 show the effect of an exaggerated single-scattering albedo corresponding perhaps to a large amount of water vapor in the atmosphere. These are curves for a composite atmosphere, thus the rise in the intensity of light toward the blue end of the spectrum.

ANALYSIS AND RESULTS

Recalling the expression for intensity of radiation reflected from the top of a layer of optical depth τ in a given direction (μ, ϕ)

$$I(0, \mu, \phi) = \mu_0 K \left[R(\tau; \mu, \phi; \mu_0, \phi_0) + \frac{\rho}{1 + \rho \bar{s}^*} \gamma_1^*(\mu) \gamma_1(\mu_1) \right] \quad (17)$$

we may solve for the Lambert ground reflectance obtaining

$$\rho = \frac{\eta}{1 - \eta \bar{s}^*} \quad (18)$$

where

$$\eta = \frac{1}{\gamma_1^*(\mu) \gamma_1(\mu_0)} \left[\frac{I(0, \mu, \phi)}{\mu_0 K} - R(\tau; \mu, \phi; \mu_0, \phi_0) \right]$$

and the reflection function R with its auxiliary functions and scalars γ_1, γ_1^* are computed by means of the doubling method described in the section entitled "Exact Solution." Parameters controlling the results of

the doubling algorithm are the Legendre series coefficients ω_i , optical depth, and single-scattering albedo. Functional dependence of reflection and transmission on wavelength is carried by these quantities. Distribution of light scattered once in a unit volume is given by the phase function. Attenuation and absorption of radiation in the atmosphere according to wavelengths are determined by optical depth (figs. 33 and 34) and single-scattering albedo (fig. 27). In this report, the absorption optical depth (fig. 34) and the single-scattering albedo - which is the ratio of the scattering albedo (fig. 33) to the sum of the scattering and absorption albedo - are determined subjectively. Reflection and transmission functions and auxiliary functions were used to examine two approaches for estimating reflection from the top of the atmosphere when (1) the ground reflects isotropically (Lambert) and (2) the ground reflectance alters according to $a + b\theta$ where a and b are constants and θ is the look angle. Figure 35 shows reflectances for White Sands sites computed from the S191 data based on the two models mentioned previously. The S191 data represent a noisy signal but the trend is plainly in accordance with that given by the anisotropic ground reflectance. This represents an extremely gross approximation shown only to suggest the effect of anisotropic surfaces underlying atmospheres. Marlatt and Solomonson (ref. 13) have studied bidirectional reflectance of several surfaces with features similar to those suggested by the second (anisotropic) reflectance model. Values of time computations of ground reflectance equivalent to bidirectional reflectance are shown in figure 36. Here the anisotropy in the ground reflectance as estimated from S191 (Rainbow Valley) observations is fully indicated. The similarity between this profile and the anisotropic ground model and between this profile and Marlatt and Solomonson's and arid grass-land observations is striking.

Ground spectra were also calculated and are given in figures 37 and 38. Low values of reflectance for the lava site for wavelengths below 0.675 micrometer result from overestimation of atmospheric reflectance probably because of overestimation of optical depth in these critical scattering wavelengths. Scattering by light hazes with particle diameters similar to wavelength is predominant.

Gypsum reflectances (fig. 35) are shown with a curve of reflectance measured independently (from fig. 39) and show fairly good agreement, at least for the target called "gypsum 1." The absorption phenomena visible between 0.6 and 0.7 micrometer are very close to water and molecular oxygen with water absorption bands, respectively. The 0.0185-micrometer bandpass for the S191 at these wavelengths could easily overlap some portion at either of these bands. These dips are considered to be residual effects of atmospheric absorption and can be removed with realistic values of absorption optical depth and single-scattering albedo. Special attention must be drawn to the depression that appears at 0.975 micrometer in figure 35. This depression is thought to be due to inappropriately high values at a single-scattering albedo resulting in underestimation of atmospheric absorption by this region.

By comparing all of the spectra from figures 37 and 38, the features that are unique to a given S191 scene are apparent. Similarities between desert sites persisted from Rainbow Valley to the White Sands desert site, while dissimilar backgrounds showed dissimilar spectra. Comparisons between

site reflectance spectra were conducted according to the method outlined in the section entitled "Data Analysis." The results of the computations are given in table VI. No comparisons were made using lava observations because of a lack of pertinent data. White Sands gypsum 1 and gypsum 2 are similar but not indistinguishable. In contrast, similarities between Rainbow Valley and Wittman are great, although Wittman is approximately 70 percent as bright as Rainbow Valley. These conclusions are based on the assumption that surface spectra are not strongly anisotropic. This assumption probably remains fairly valid for high Sun elevations (low zenith angle) but fails for low Sun elevations.

Other possible anomalies in the observed spectra of the Earth may be caused by peculiarities of the bidirectional reflectance of the ground. Two such anomalies, which have received some attention in the past, have come to be known as "hot spot" and "glint." Glint is an example of specular or mirror-type reflection. Hot spot reflection appears to be a possible combination of glint and diffuse scattering phenomena and depends on the texture of the reflecting surface. For example, a forest stand with strong sidelighting by the Sun appears brighter on the sunlit side than on the side away from the Sun. Glint is particularly obvious on water surfaces at all Sun elevations, while the hot spot (a backward-scattering phenomenon) appears more strongly on rough surfaces with low-Sun-elevation angles. Both phenomena are well known in photography and probably appear, in some way, in all photographs. Efforts are generally made to avoid geometrical configurations that might cause the measurement of spurious information because of these phenomena. These types of reflection by Earth surfaces represent parts of a continuous distribution of light (by incident and reflected directions) from a particular surface. The distribution is called bidirectional reflectance. These phenomena are, therefore, part of any measured spectrum of the surface and not some peculiarity that might cause a masking of the spectrum. Some investigators believe that a notable amount of information is to be found by examining photographs showing glint (ref. 14).

Linking our discussion to the areas under study, note the markedly higher reflectance by the desert at Rainbow Valley (fig. 37(a)) compared to the other two sites. When comparing reflectances estimated from helicopter data using an application of the two-stream approximation to the reflection of radiation from atmospheric layers (see appendix), the reflectances at the Rainbow Valley and Wittman sites are similar (fig. 40). Note the similarity between reflectances computed from the FSS data for Rainbow Valley (RBV-FSS) and for Wittman (WTT-FSS). The reflectance computed from the S191 data for the same two sites (RBV-S191 and WTT-S191) indicates that the RBV-S191 shows a strong effect of hot-spot-type reflection. Table VII lists the geometrical parameters for these sites. A full understanding of bidirectional reflection would contribute greatly to the uses and analyses of spectra measured from space.

CONCLUSIONS

Results of the preliminary analyses of the S191 spectrometer data have indicated the generally high quality of the data. Initial examination showed that if the scene being sampled is constant (i.e., the same from observation to observation), any difference from one observation to another can be predicted. Variations among such observations may be accounted for by variations in the geometry for the observation alone (once the characteristics of the atmospheric-scattering interface are established). When no knowledge of the atmospheric-scattering properties is available, the S191 spectrometer has been proven to provide repeatable spectra of the Earth.

The spectrometer data proved to be compatible with analytical methods, requiring no preconditioning. Features of the ground reflectance computed from the S191 data allowed distinguishing between desert sites at two widely separated areas (Phoenix and White Sands) despite the similarities in their spectra. Computed spectra generally agreed with known spectra for similar backgrounds measured independently.

Atmospheric variables (optical depth and single-scattering albedo) proved to be the most critical in computations of atmospheric effects of scattering on incident solar radiation. Although not studied, phase functions for the light hazes (with scattering optical depths <1.0) are not thought to account for much variability in reflected (or transmitted) radiation for the set of Sun and look angles studied. Thus, better data for total optical depth (i.e., for scattering by molecules, aerosol particles, and for attenuation by absorption) are required for all sensor bands in order to better determine the effect of the atmosphere on the attenuation of reflected solar radiation.

Future low-Earth-orbit missions may require the use of multisensor systems to obtain specific Earth applications data. A spaceborne spectrometer similar to the S191 can obtain detailed spectral information that cannot be provided by any other sensor. These data can be used to

1. Determine atmospheric water content
2. Evaluate spectral bands for obtaining specific data of interest in designing sophisticated scanner equipment
3. Determine the optimal look geometry for use in determination of orbits and instrument characteristics
4. Determine atmospheric optical depth (and the related problem of water turbidity)

Lyndon B. Johnson Space Center
National Aeronautics and Space Administration
Houston, Texas, February 17, 1978
652-01-82-00-72

TABLE I.- S192 MULTISPECTRAL SCANNER PARAMETERS

Scientific data output (SDO) no.	Band no. (a)	Peak response wavelength, μm	Lower 1/2 power, μm	Upper 1/2 power, μm
22	1	0.432	0.420	0.447
18	2	.470	.451	.503
1, 2	3	.526	.50	.55
3, 4	4	.562	.54	.586
5, 6	5*	.630	.599	.654
7, 8	6*	.685	.654	.734
9, 10	7*	.810	.770	.890
19	8	.970	.930	1.050
20	9	1.10	1.030	1.190
17	10	1.22	1.150	1.280
11, 12	11	1.64	1.550	1.730
13, 14	12	2.25	2.10	2.34
15, 16, 21	13	--	10.04	12.65

^aEREP 20 data included all bands; EREP 27 data were limited to those specified with an asterisk.

TABLE II.- DATA COLLECTED OVER NEW MEXICO AND ARIZONA

(a) EREP 20, White Sands, N. Mex., Aug. 12, 1973

Test site	Forward view angle	View angle	Time, universal time (UT)
S191 spectrometer			
Lava	45° to 18°		14:45:35 to 14:46:23
Desert	9° to -1°		14:46:36 to 14:46:48
Gypsum 1	-11° to -13°		14:47:02 to 14:47:05
	-21° to -22°		14:47:14 to 14:47:15
Gypsum 2	-14° to -17°		14:47:06 to 14:47:09
	-19° to -20°		14:47:11 to 14:47:13
Helicopter FSS ^a			
Lava		(a)	(a)
Desert		(a)	(a)
Gypsum 1		(a)	(a)
Gypsum 2		(a)	(a)
S192 spectrometer			
Lava			^b 14:46:40

^aData not processed.^bAll bands.

TABLE II.- DATA COLLECTED OVER NEW MEXICO AND ARIZONA - Concluded

(b) EREP 27, Phoenix, Ariz., Sept. 6, 1973

Test site desert targets at -	Forward view angle	View angle	Time, UT
S191 spectrometer			
Rainbow Valley	40° to 12°		21:23:48 to 21:24:31
Wittman	8° to -2°		21:24:41 to 21:24:53
Old Verde Canal	-7° to -24°		21:25:04 to 21:25:24
Helicopter FSS			
Rainbow Valley		Nadir	18:45:21 to 19:06:10
Wittman		Nadir	21:25:45 to 21:40:13
Old Verde Canal		Nadir	20:08:25 to 20:36:27
S192 spectrometer			
Old Verde Canal			^c 21:24:52

^cBands 5, 6, and 7.

TABLE III.- SCENE DIMENSIONS AND PRECIPITABLE WATER PROFILE AT
PHOENIX, ARIZONA, ON SEPTEMBER 6, 1973

Data acquisition altitude, m (ft)	Diameter of target area, m	Precipitable water in air column from surface to altitude, cm
Helicopter FSS with 22° FOV		
152 (500)	60	0.32
1524 (5000)	600	1.63
2750 (9000)	1060	2.39
3050 (10 000)	1200	2.53
3658 (12 000)	1420	2.80
S191 with 1-mrad FOV		
435 km (235 n.mi.)	^a 460	3.10

^aAt nadir.

TABLE IV.- FSS AND S191 SCAN ANALYSES AS A FUNCTION OF ALTITUDE

Altitude, m	Rainbow Valley ^{a,b}		Wittman ^{a,b}		Old Verde Canal ^{a,b}	
	μ	r^2	μ	r^2	μ	r^2
FSS scan analysis						
152	0.6353×10^{-2}	0.9976	--	--	0.5173×10^{-2}	0.9951
^c 1524	.6384	1.0000	0.5485×10^{-2}	1.0000	.5555	1.0000
2743	.6568	.9904	.5217	0.9974	.5596	.9931
3048	--	--	.5049	.9963	--	--
3658	.6133	.9487	--	--	.5252	.9796
S191 scan analysis						
435 000	0.7726×10^{-2}	0.9752	0.4914×10^{-2}	0.9752	0.5089×10^{-2}	0.9794

^a μ = mean radiance intensity and r^2 = standard error of correlation.

^bThe time difference between FSS and S191 for Rainbow Valley was 9125 sec; for Wittman, 94 sec; and for Old Verde Canal, 4233 sec.

^cReference scan for FSS.

TABLE V.- FSS SCAN ANALYSIS FOR THREE PHOENIX SITES

Rainbow Valley, 1524 m				Wittman, 1524 m				Old Verde Canal, 1524 m			
Time	μ	r^2	Time	μ	r^2	Time	μ	r^2	Time	μ	r^2
18:51:04	0.6480x10 ⁻²	0.9947	21:26:09	0.5098x10 ⁻²	0.9963	20:14:24	0.5391x10 ⁻²	0.9996			
18:51:05	.6506	.9943	21:26:10	.5097	.9977	20:14:25	.5417	.9986			
18:51:37	.6368	.9976	21:26:11	.5220	.9980	20:14:26	.5405	.9993			
18:51:38	.6387	.9976	21:26:12	.5337	.9972	20:14:27	.5475	.9984			
18:51:39	.6387	.9962	21:26:13	.5393	.9997	20:14:28	.5545	.9980			
18:51:40	.6370	.9977	21:26:14	.5419	.9995	20:14:29	.5538	.9991			
18:51:41	.6347	.9980	21:26:15	.5446	.9994	20:14:30	.5585	.9990			
18:51:42	.6386	.9915	21:26:16	.5485	1.0000	20:14:31	.5555	1.0000			
18:51:43	.6330	.9980									
18:51:44	.6384	1.0000									

TABLE VI.- LINEAR COMPARABILITY OF TWO SITE SPECTRA

Site 1 (a)	Site 2 (b)	r ²	Scale factor	Displacement	Comparison
WSD	WSG1	0.6241	0.9696	0.3980	Poor
WSG1	WSG1X	.9988	.9829	.0021	Excellent
WSG1	WSG2	.9659	.7777	.019	Fair
WTT	WSD	.9578	.9782	-.0188	Fair
WTT	WSG1	.6638	.9994	.3686	Poor
WTT	OVC	.9921	1.1511	-.017	Excellent
RBV	WTT	.9963	.6988	-.0254	Excellent
RBV	OVC	.9859	.8034	-.0458	Good

^aWSD = White Sands, desert; WSG1 = White Sands, gypsum 1 (first observation);
WTT = Wittman; RBV = Rainbow Valley.

^bWSG1X = White Sands, gypsum 1 (last observation); WSG2 = White Sands,
gypsum 2; OVC = Old Verde Canal.

TABLE VII.- GEOMETRICAL PARAMETERS FOR THE CURVES
PRESENTED IN FIGURE 40

Site sensor	Solar zenith angle, deg	Look angle, deg	Azimuth difference, deg
RBV-FSS	28.03	0	0
RBV-S191	34.50	41.93	173.89
WTT-FSS	38.25	0	0
WTT-S191	37.87	12.95	47.51

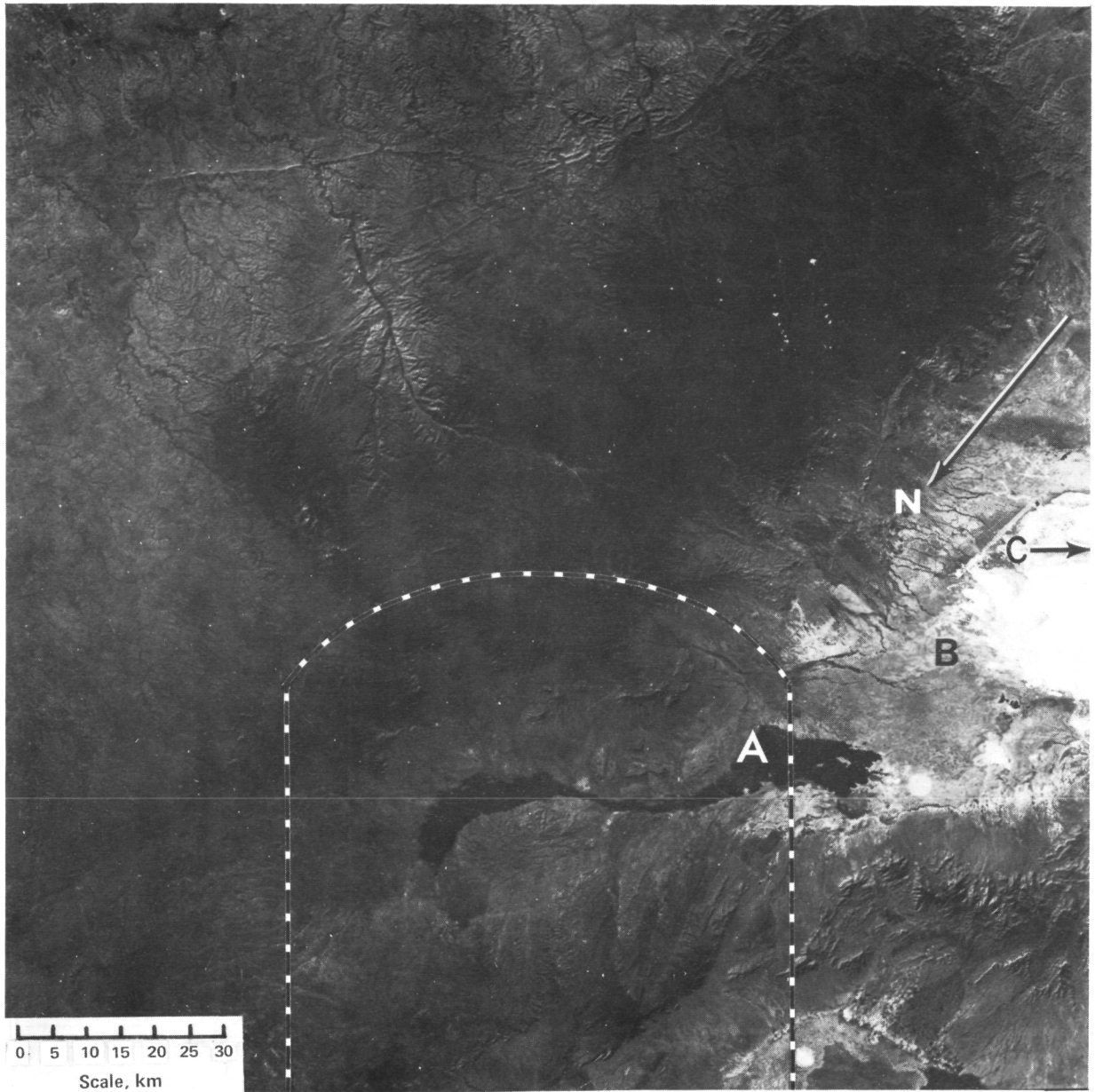


Figure 1.- S190A photograph (SL3-28-197) of lava bed near White Sands taken on August 12, 1973. Dashed line specifies S192 swath.

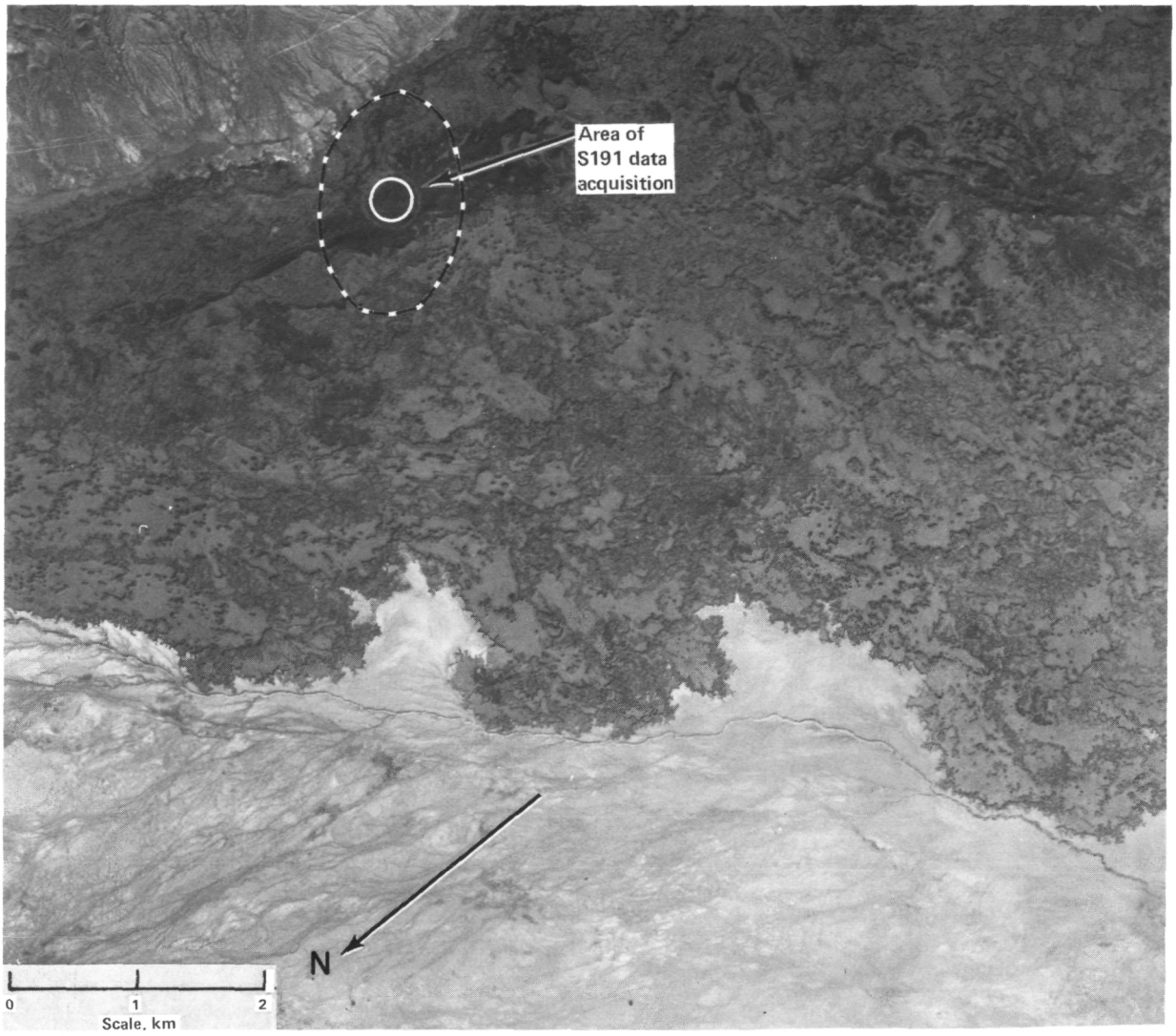


Figure 2.- RC8 aircraft photograph (mission 238, frame 74-0064) of lava site targeted by S191 during EREP 20 pass. Circle indicates S191 spatial resolution.

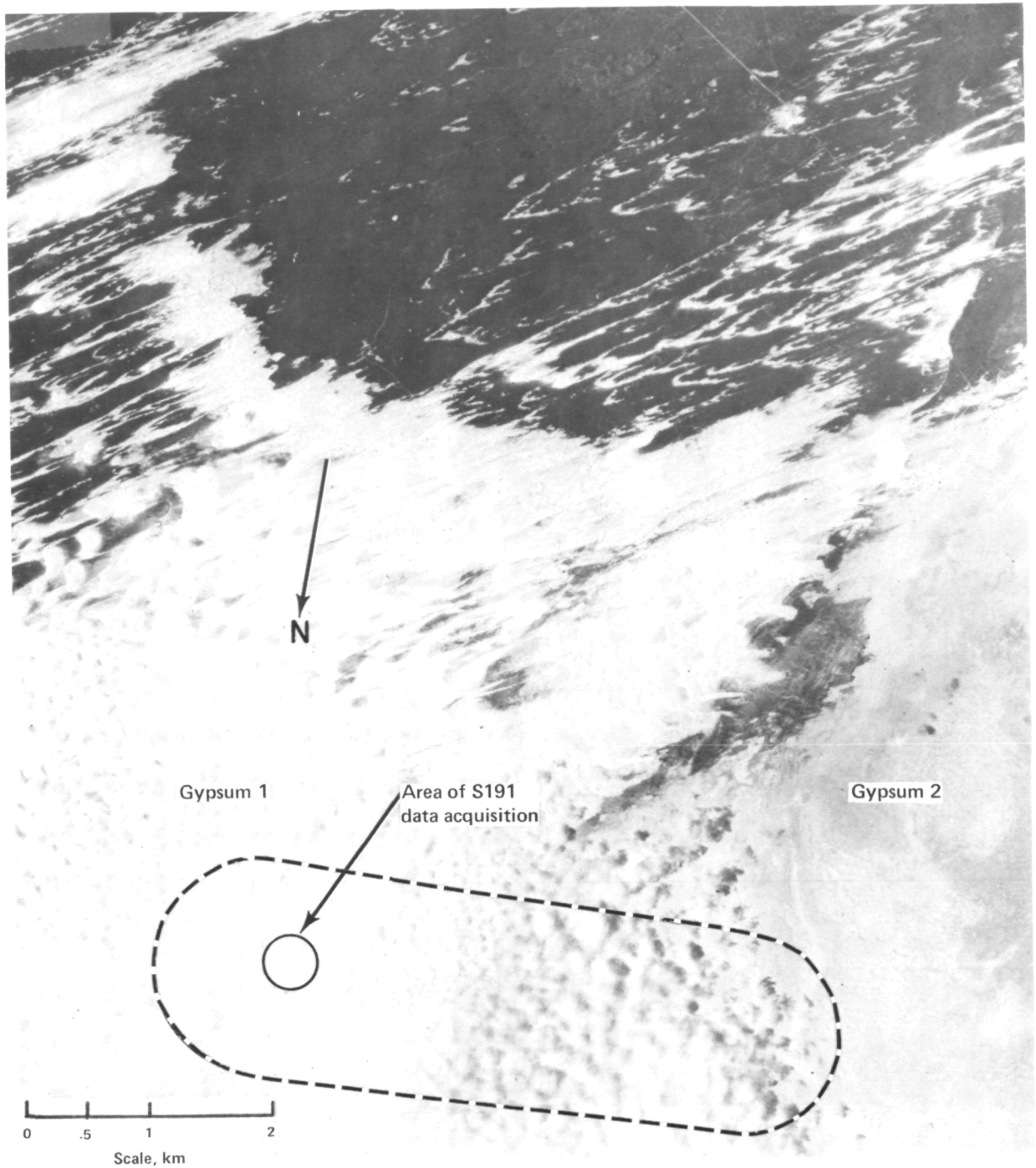


Figure 3.- RC8 aircraft photograph (mission 238, frame 74-0074) of gypsum sites. Dashed line outlines gypsum 1 and gypsum 2 as targeted by S191 VTS. Circle indicates S191 spatial resolution.

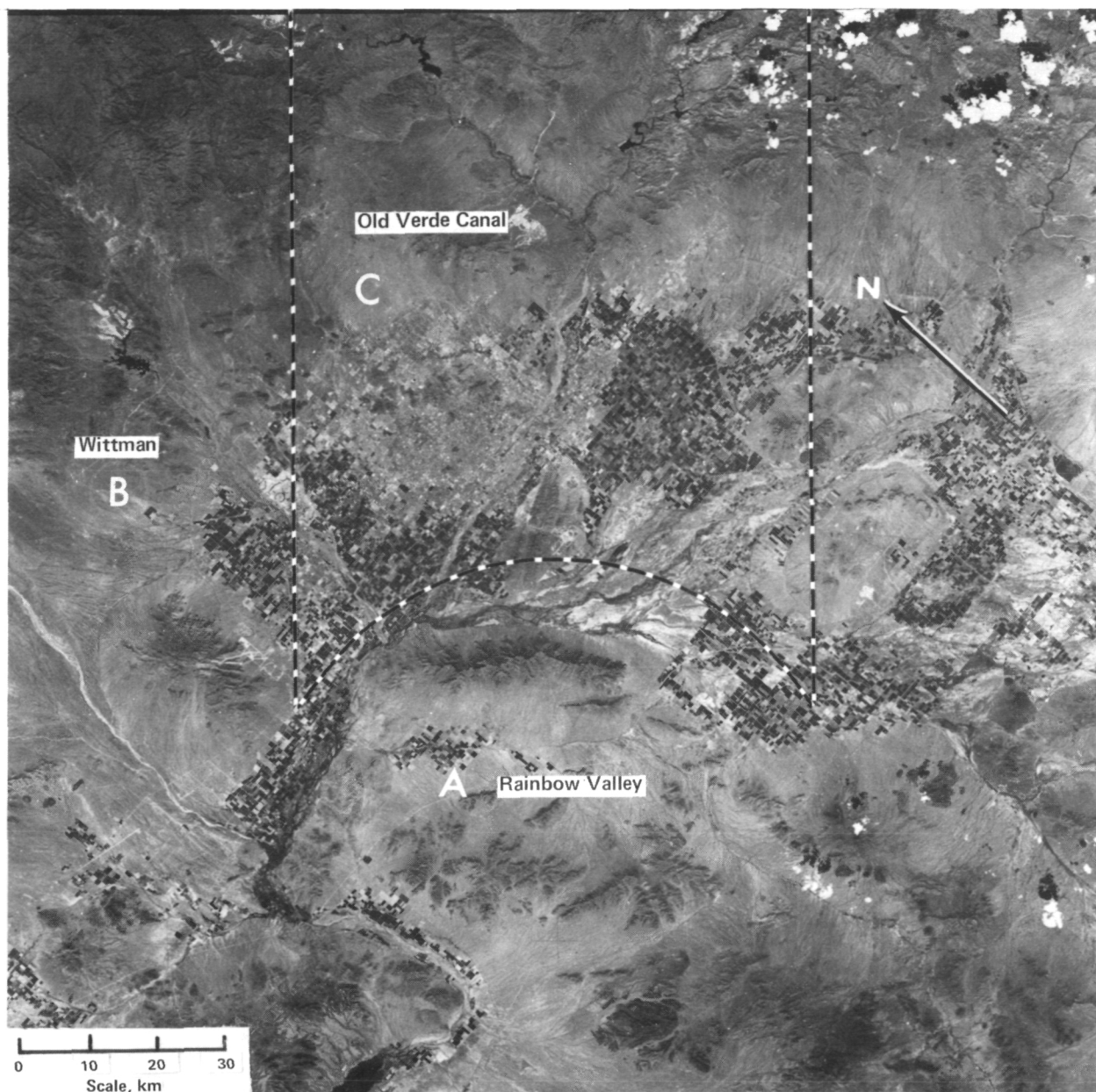


Figure 4.- S190A photograph (SL3-34-243) of Phoenix region taken on September 6, 1973. Dashed lines specify S192 swath.

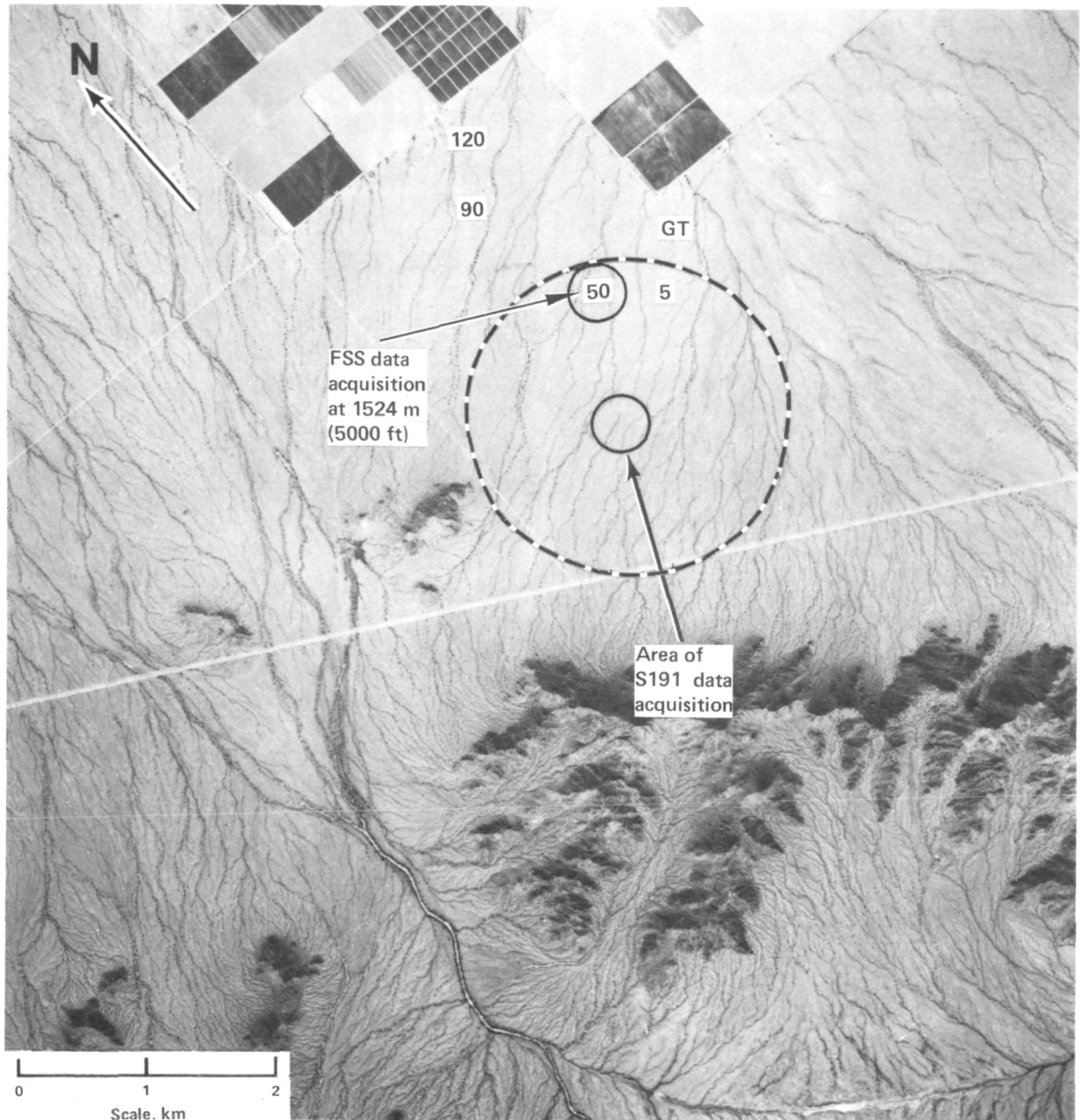


Figure 5.- RC8 aircraft photograph (mission 247, frame 123-0037) of Rainbow Valley. Dashed circle outlines site as targeted by S191 VTS during EREP 27 pass. Solid circles indicate spatial resolution of the S191 and the FSS data at 1524 meters (5000 feet). (GT = location of ground-truth team, digits = location of FSS data acquisition at altitude).

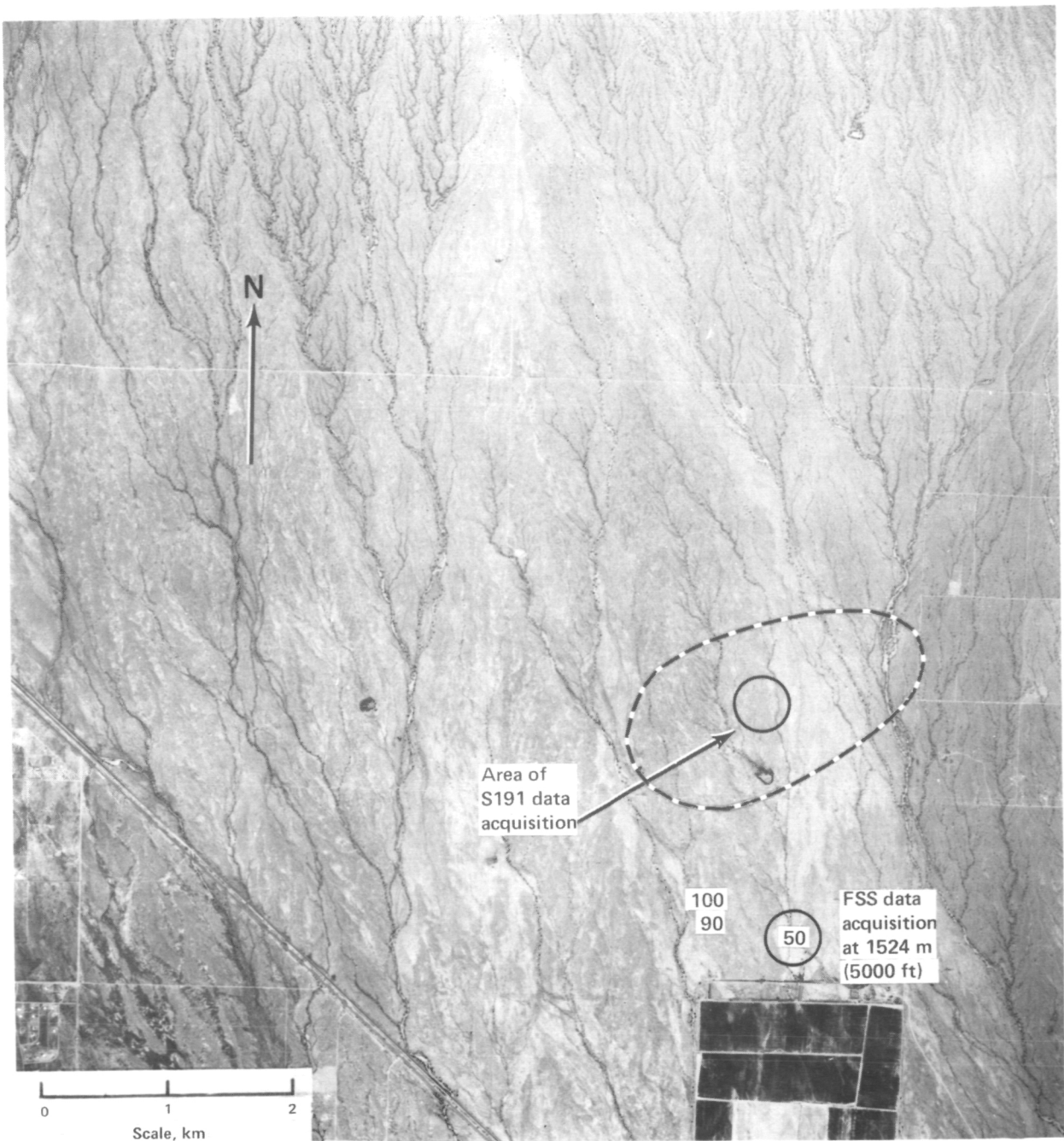


Figure 6.- RC8 aircraft photograph (mission 247, frame 123-0016) of Wittman as targeted by S191 VTS and the FSS. Circles indicate spatial resolution of S191 and FSS data taken at 1524 meters (5000 feet).

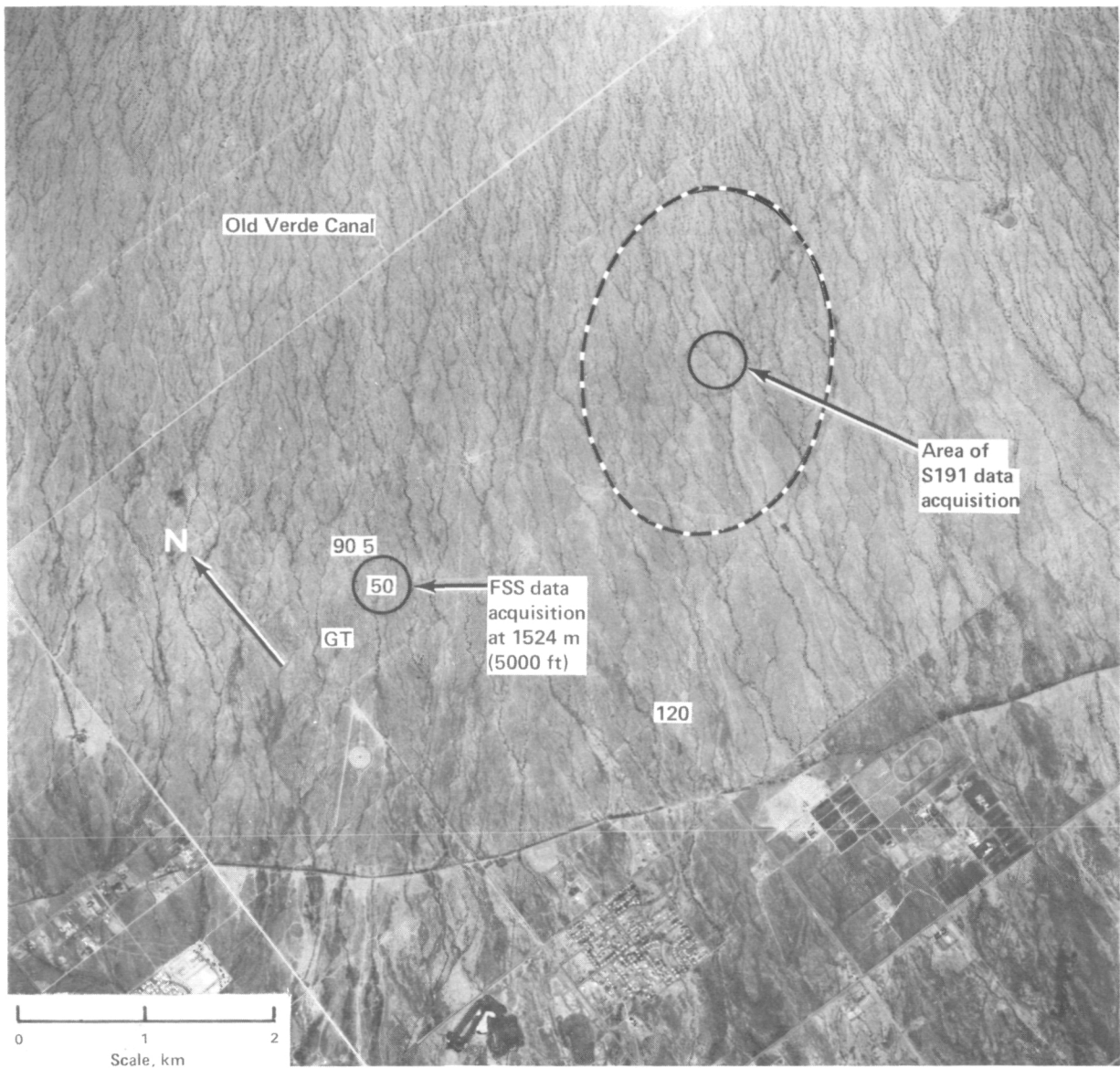


Figure 7.- RC8 aircraft photograph (mission 247, frame 123-0055) of Old Verde Canal as targeted by S191 VTS and the FSS. Circles indicate spatial resolution of S191 and FSS data taken at 1524 meters (5000 feet).

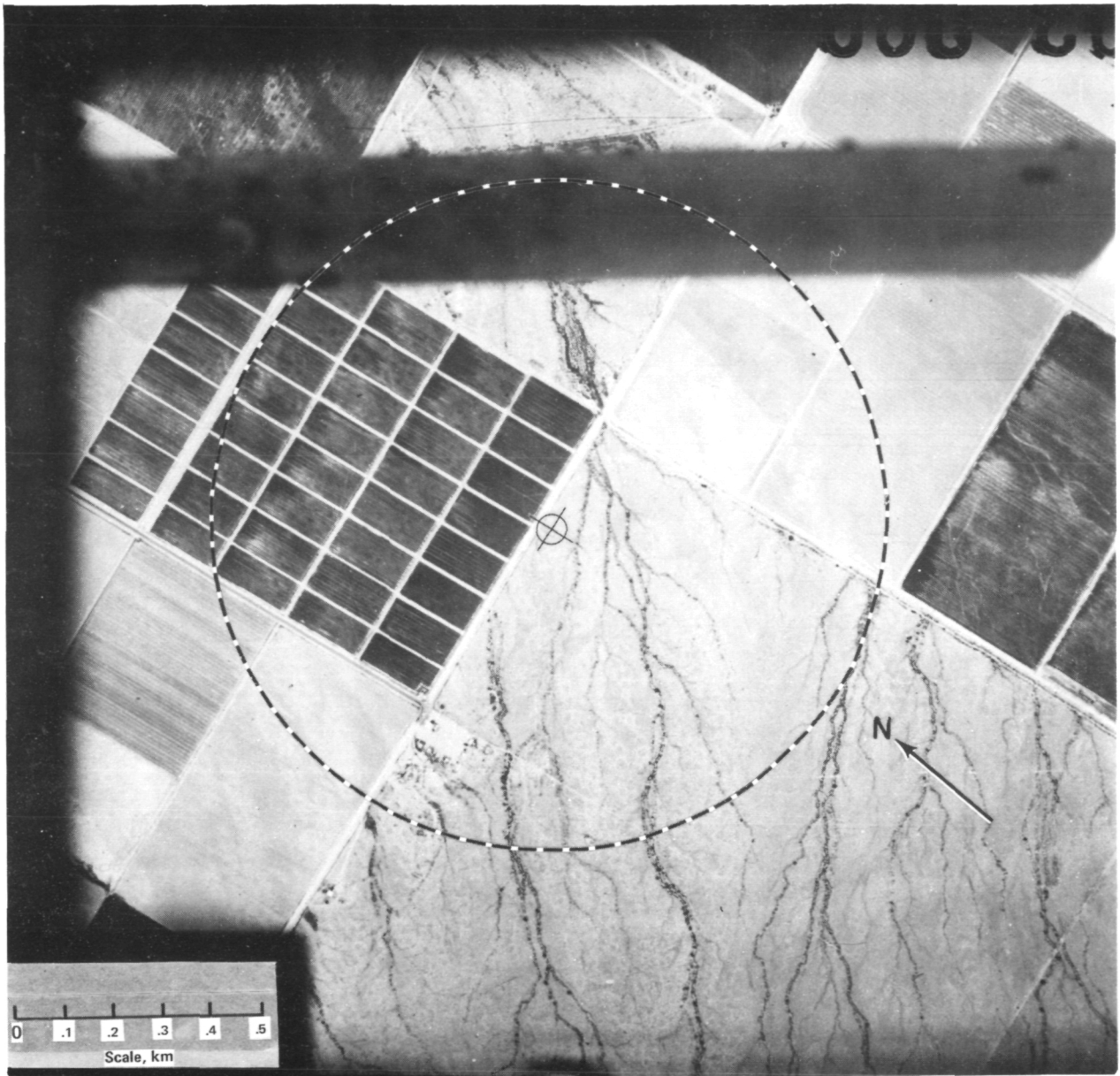


Figure 8.- vinten (helicopter) photograph (mission 252, frame 003-080) of Rainbow Valley as targeted by the FSS from an altitude of 3658 meters (12 000 feet). Dashed circle outlines FSS FOV.

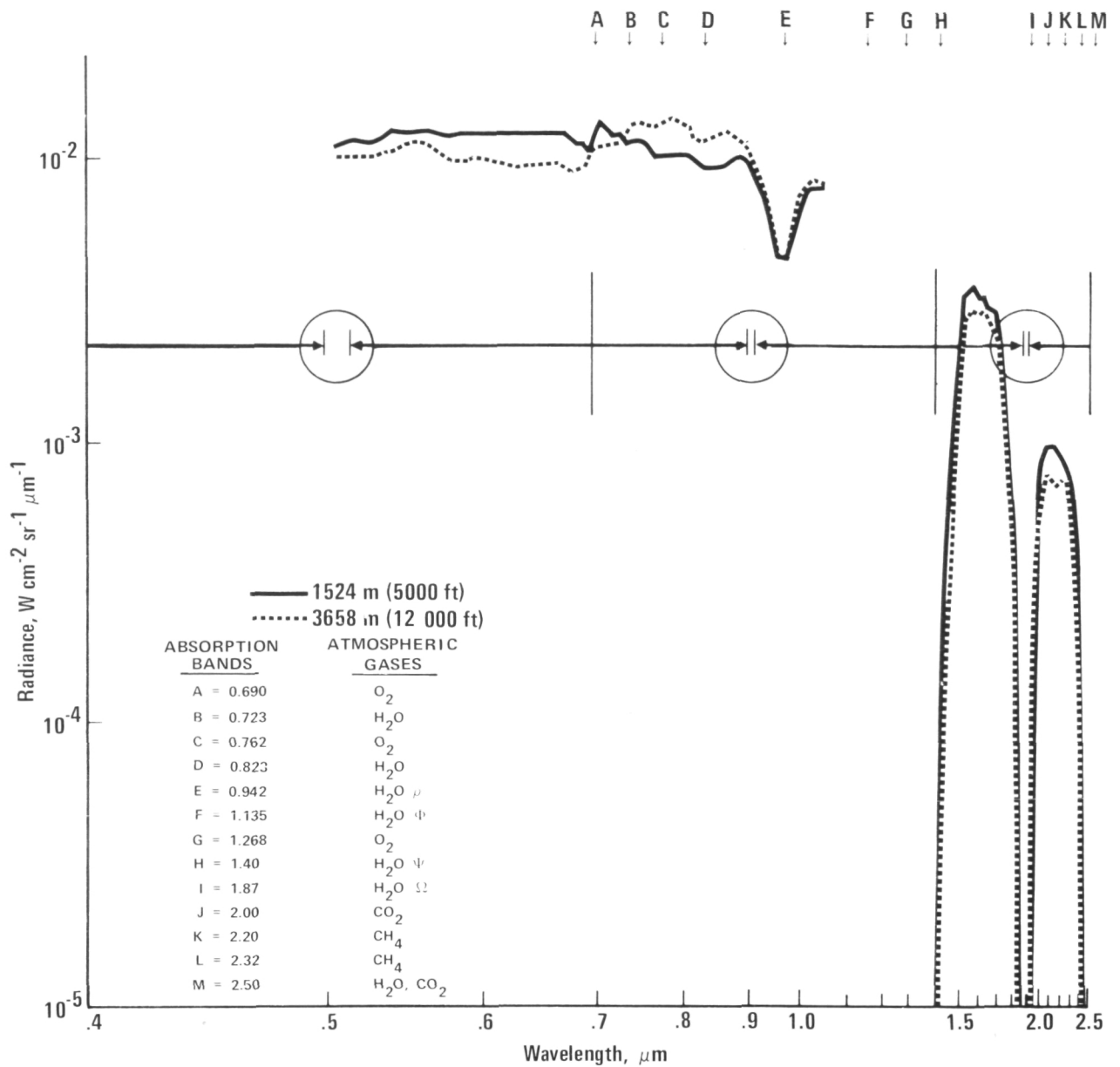


Figure 9.- Spectral profiles of radiance recorded by the FSS at altitudes of 1524 meters (5000 feet) and 3658 meters (12 000 feet) over Rainbow Valley on September 6, 1973. Letters A through M designate wavelengths of absorption bands of atmospheric gases. Circles show spectral resolution within the specified wavelength limits.

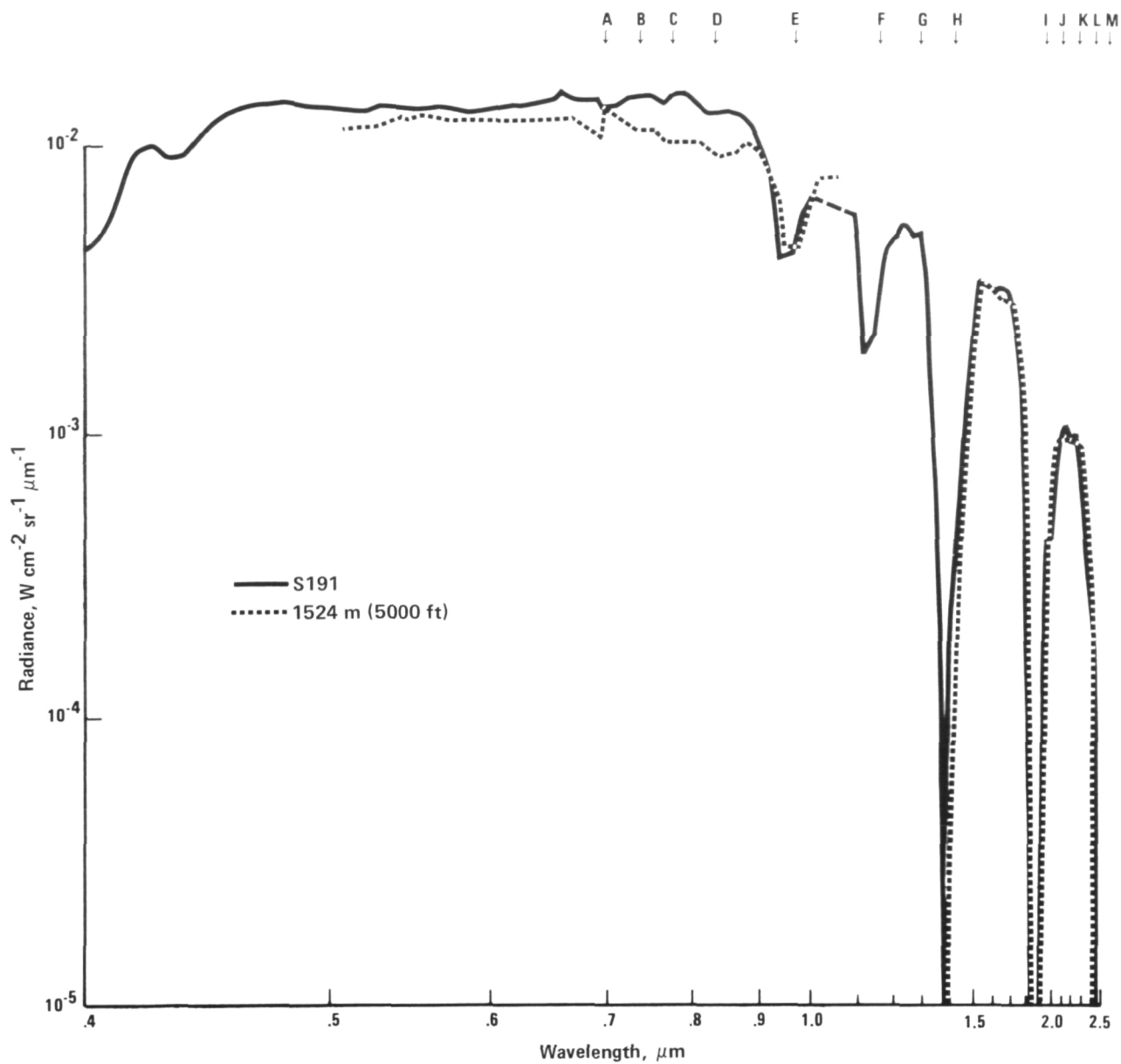


Figure 10.- Spectral profiles of radiance recorded by the FSS at an altitude of 1524 meters (5000 feet) and by the S191 over Rainbow Valley. (Absorption bands are defined in fig. 9.)

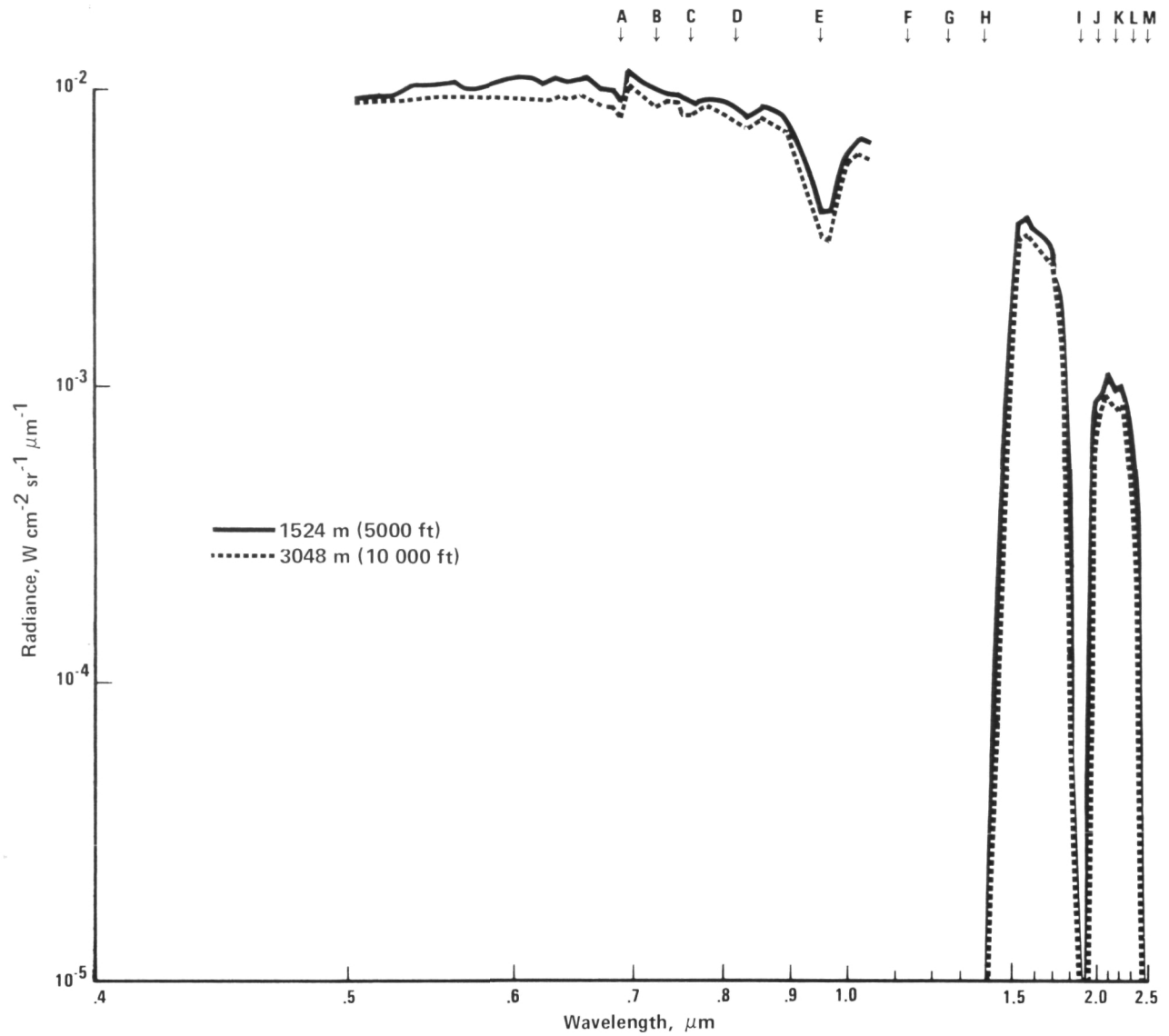


Figure 11.- Spectral profiles of radiance recorded by the FSS at altitudes of 1524 meters (5000 feet) and 3048 meters (10 000 feet) over Wittman on September 6, 1973. (Absorption bands are defined in fig. 9.)

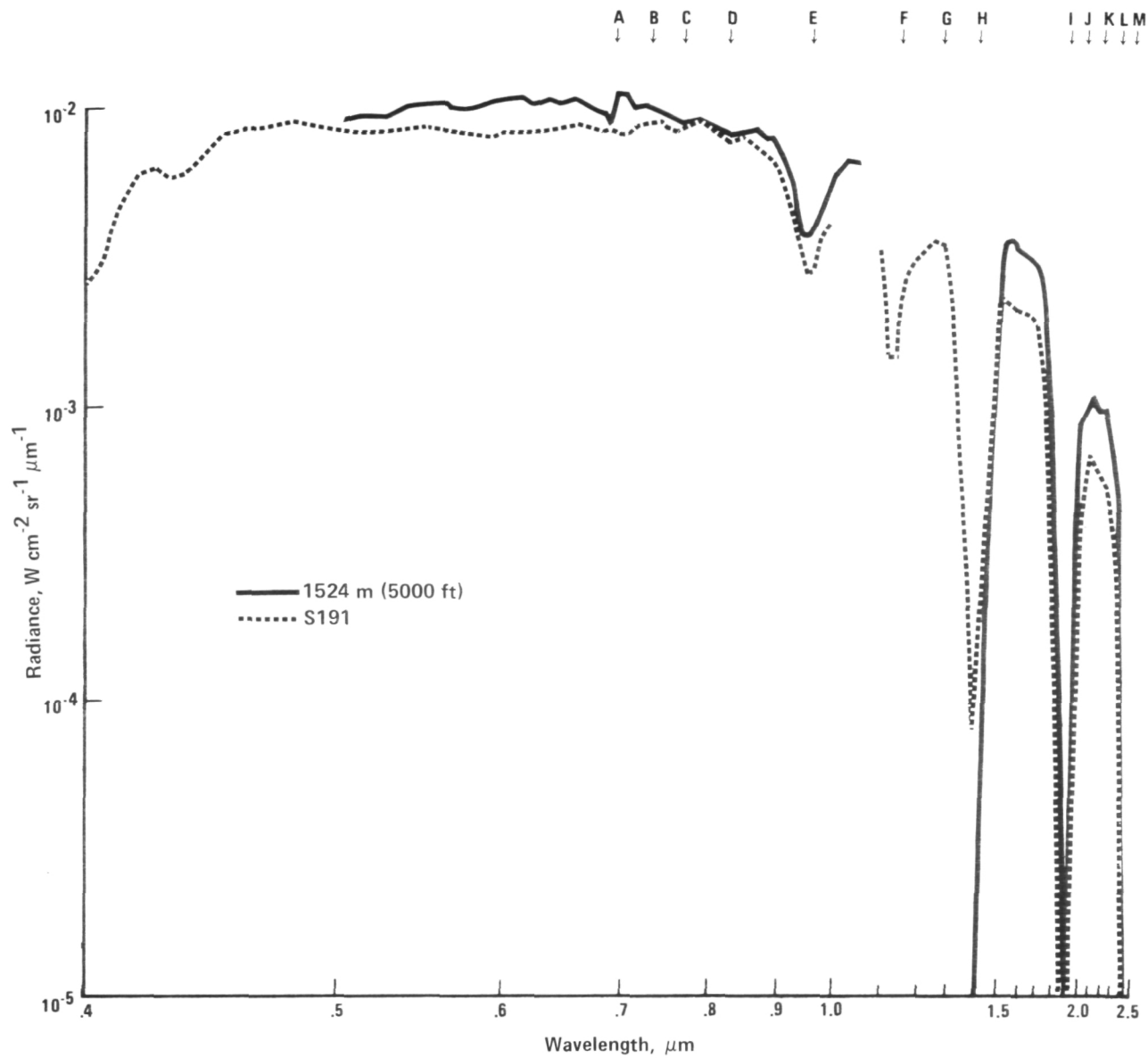


Figure 12.- Spectral profiles of radiance recorded by the FSS at an altitude of 1524 meters (5000 feet) and by the S191 over Wittman. (Absorption bands are defined in fig. 9.)

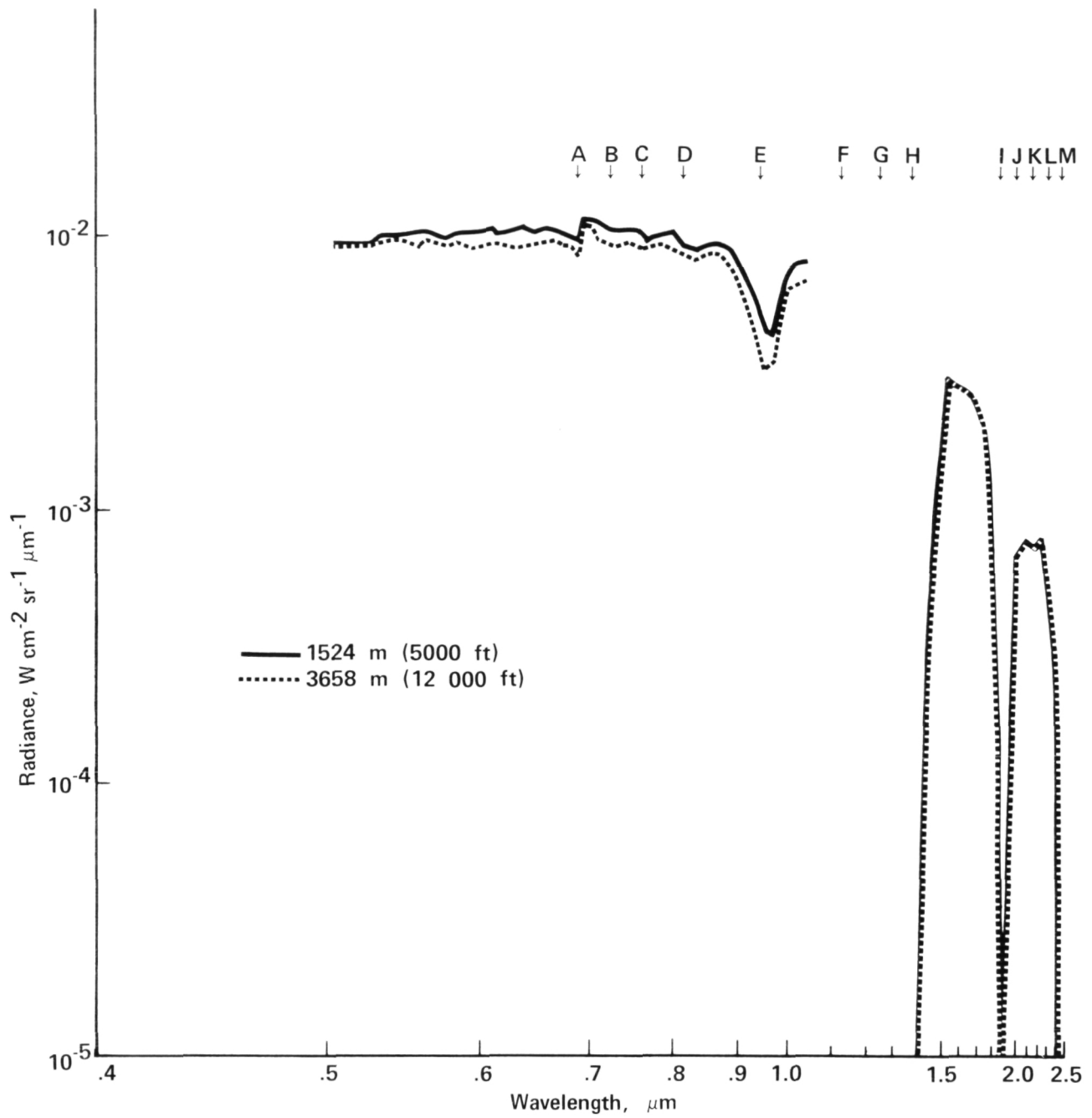


Figure 13.- Spectral profiles of radiance recorded by the FSS at altitudes of 1524 meters (5000 feet) and 3658 meters (12 000 feet) over Old Verde Canal. (Absorption bands are defined in fig. 9.)

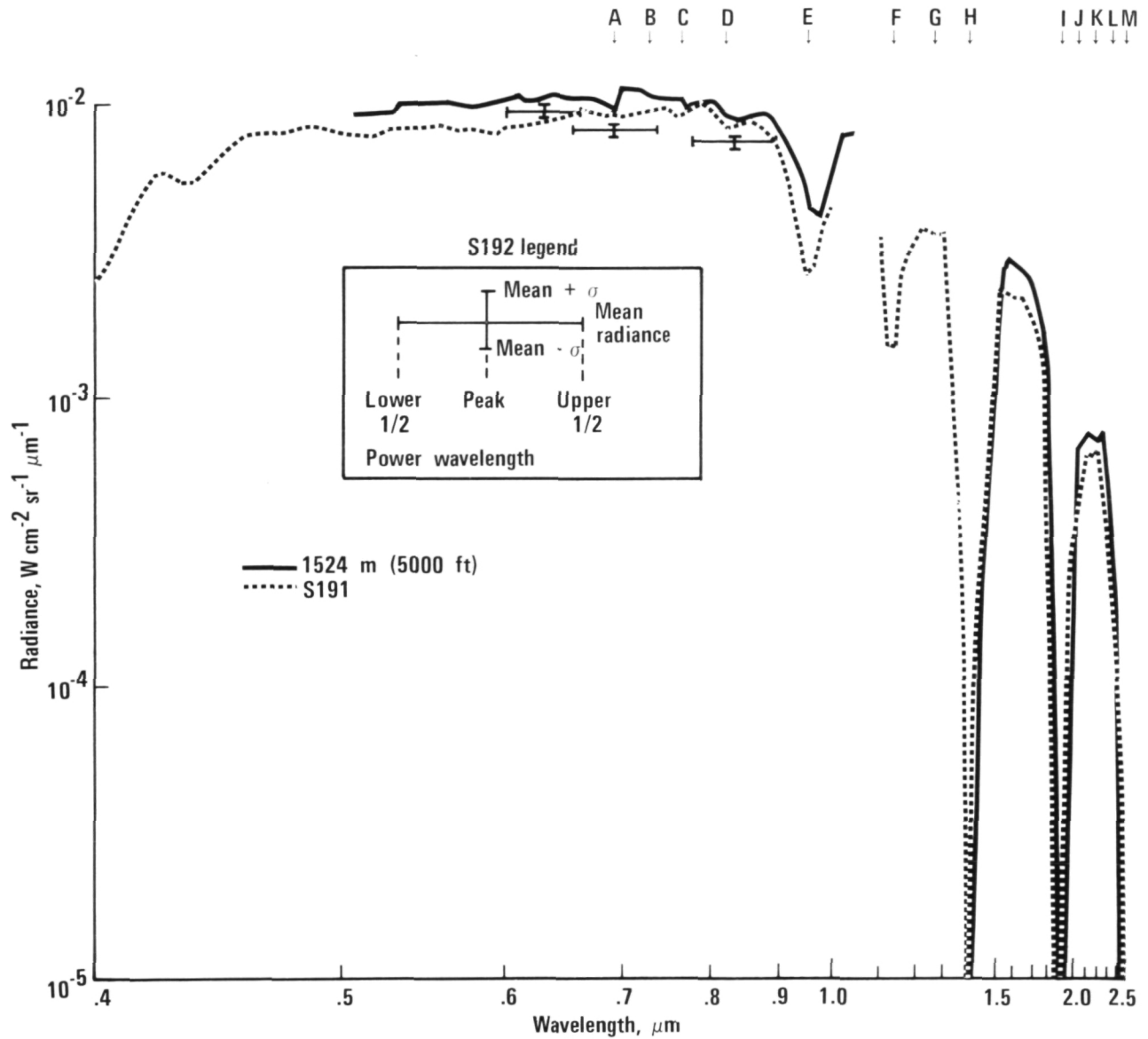


Figure 14.- Spectral profiles of radiance recorded by the FSS at an altitude of 1524 meters (5000 ft) and by the S191 over Old Verde Canal. The intersect diagram is composed of the S192 mean radiance value with standard deviations and one-half power spectral response wavelength limits. (Absorption bands are defined in fig. 9.)

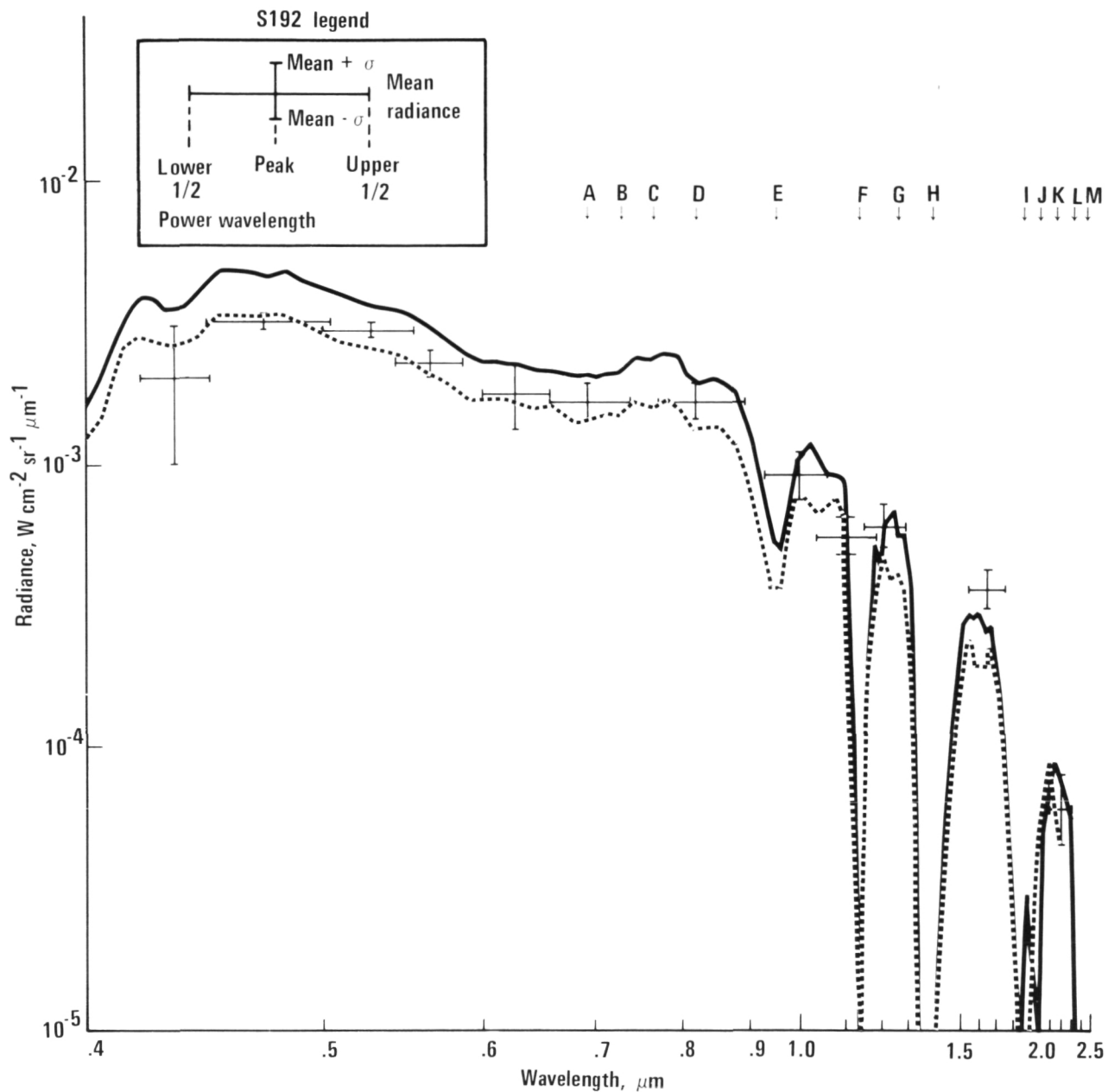


Figure 15.- Spectral profiles of radiance recorded by the S191 targeting lava (basalt) near White Sands at 14:45:37.66 UT (solid line) and 14:46:20.60 UT (dashed line). The intersect diagram is composed of the S192 mean radiance value with standard deviations and one-half power spectral response wavelength limits. (Absorption bands are defined in fig. 9.)

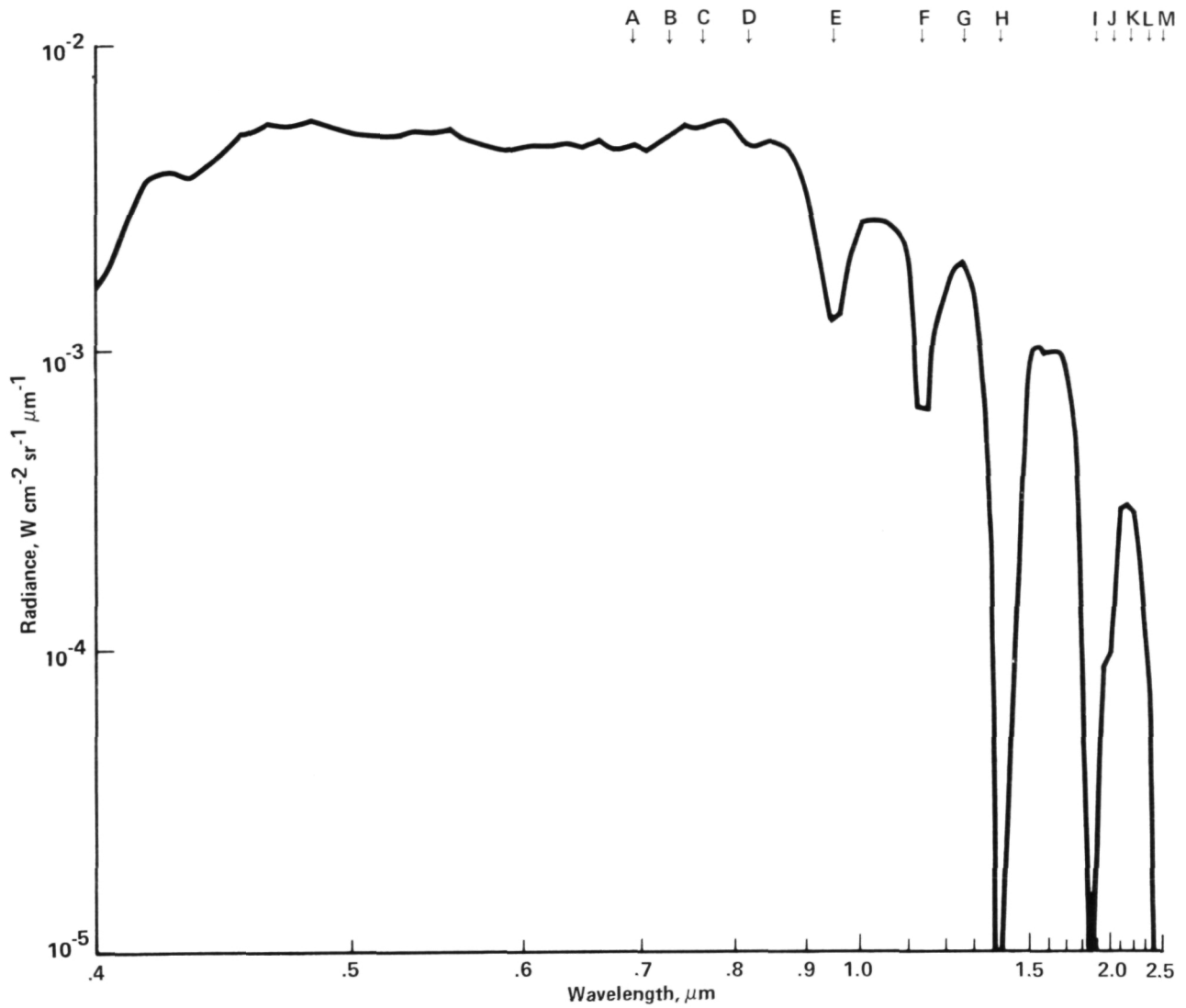


Figure 16.- Spectral profile of radiance recorded by the S191 targeting desert near White Sands at 14:46:36.47 UT. (Absorption bands are defined in fig. 9.)

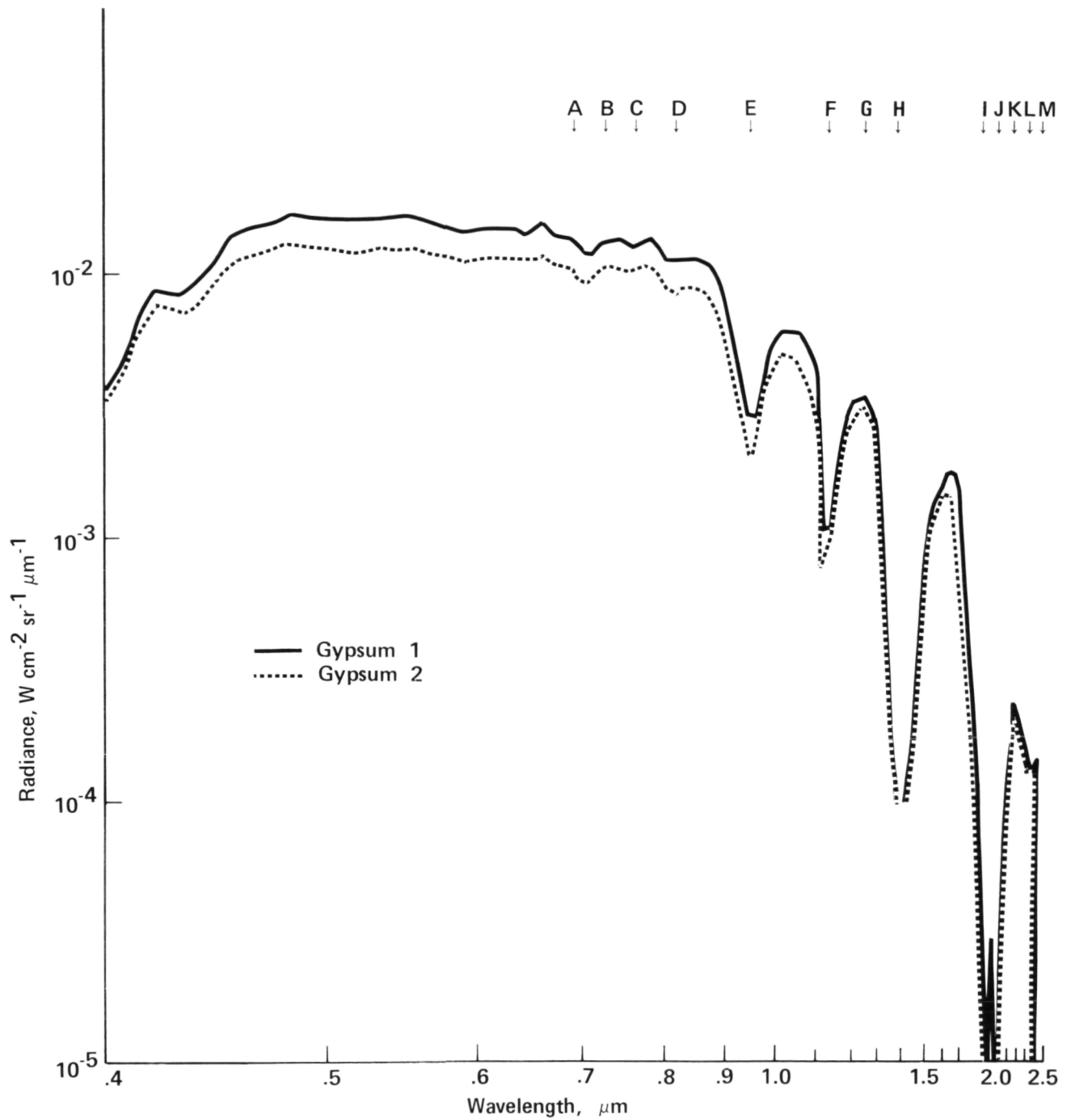


Figure 17.- Spectral profiles of radiance recorded by the S191 targeting gypsum 1 near White Sands at 14:47:02.60 UT and gypsum 2 at 14:47:06.33 UT. (Absorption bands are defined in fig. 9.).

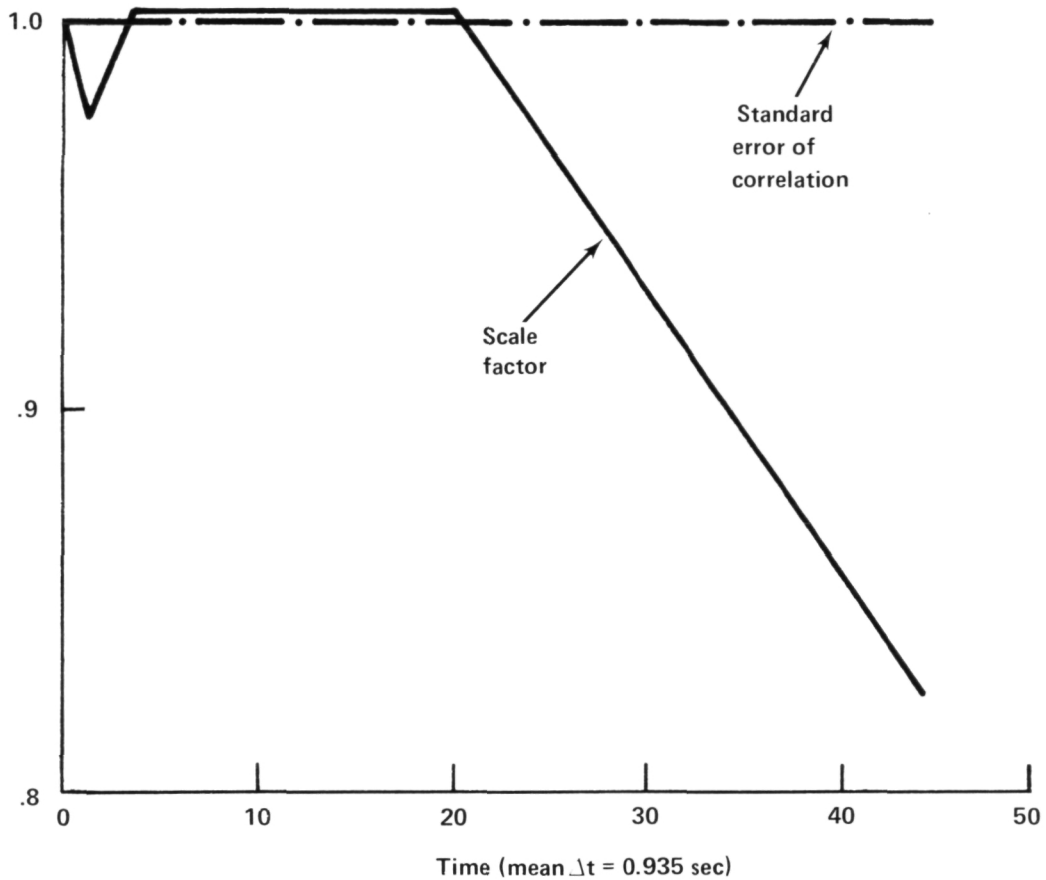


Figure 18.- Temporal comparison of the scale factor and the standard error of correlation (r^2) of consecutive S191 scans for Rainbow Valley. The dot-dashed line represents the computed scale values and the solid line is the scale trend or slope change line.

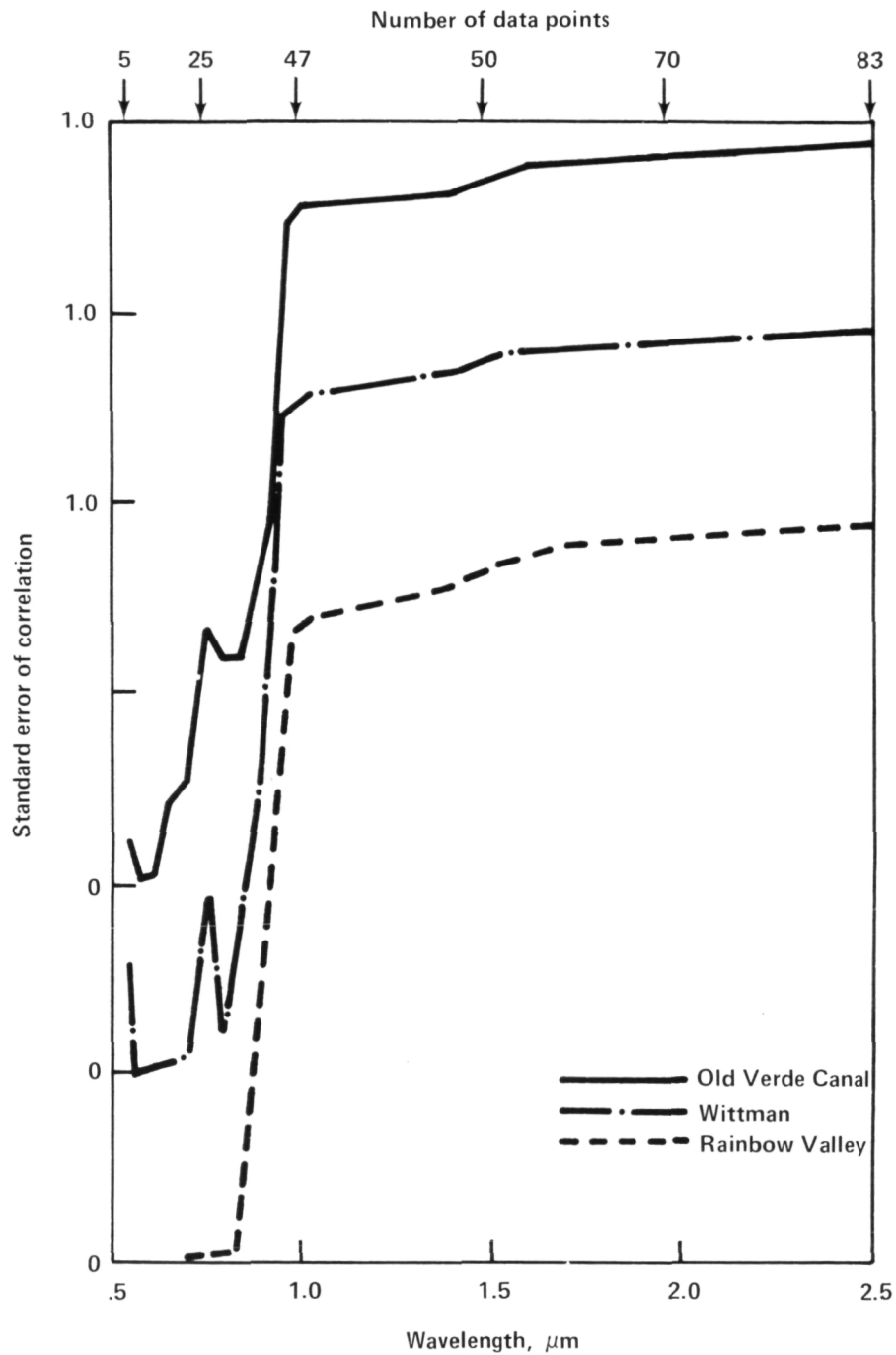
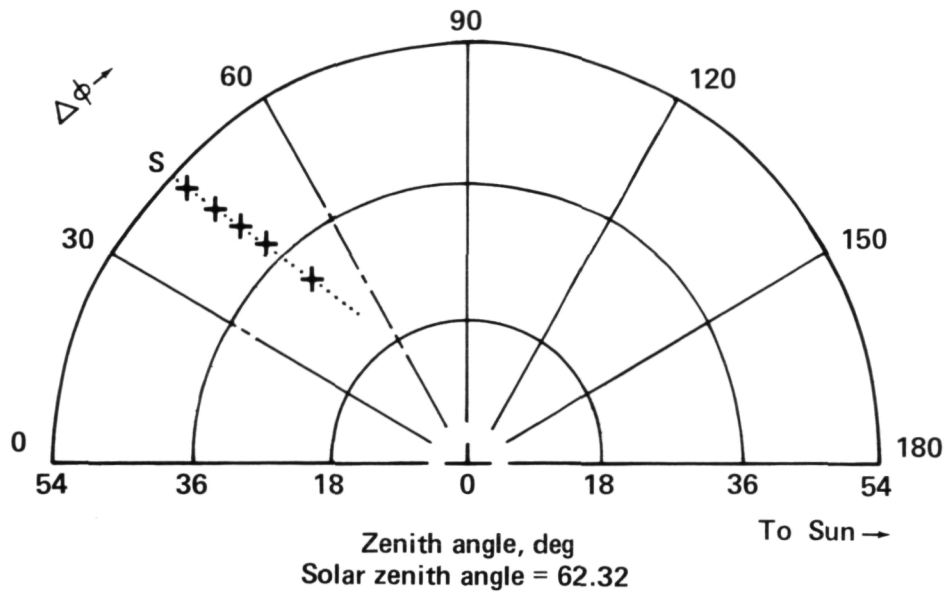
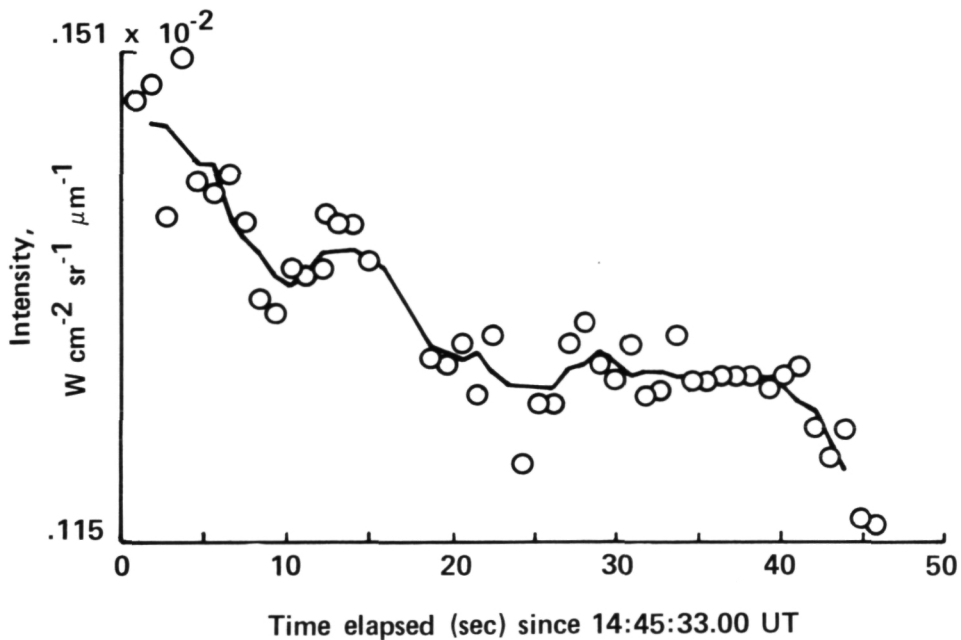


Figure 19.- The standard error of correlation between S191 and FSS data taken at an altitude of 1524 meters (5000 feet). The plotted values result from cumulative computations for data with wavelengths less than or equal to the abscissa value.

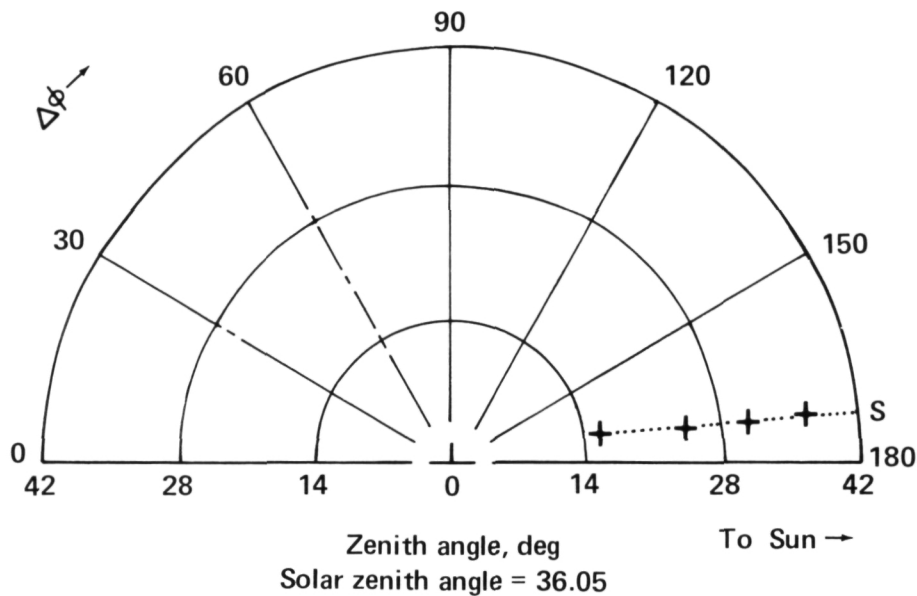


(a) Angular geometry with the spacecraft at the origin. Radial measure is look angle and angular measure is azimuth difference. Plot begins at "S" with 10-second intervals.

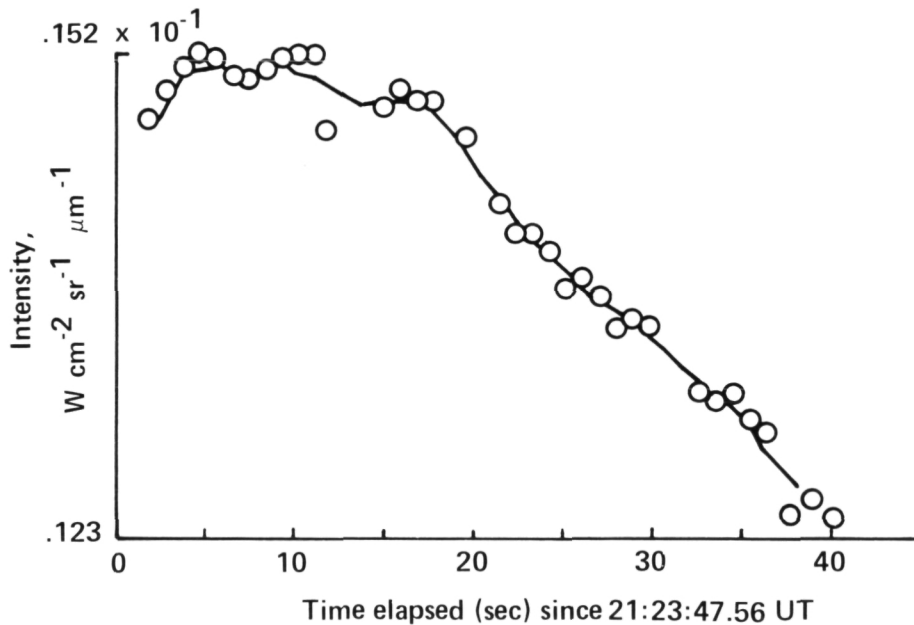


(b) Change of 0.7 micrometer radiance with time (Line = five-scan average).

Figure 20.- Lava (basalt) at White Sands from 14:45:33.0 to 14:46:22.47 UT on EREP 20.



(a) Angular geometry with the spacecraft at the origin. Radial measure is look angle and angular measure is azimuth difference. Plot begins at "S" with 10-second intervals



(b) Change of 0.7 micrometer radiance with time
(Line = five-scan average)

Figure 21.- Desert at Rainbow Valley from 21:23:47.56 to 21:24:31.38 UT on EREP 27. Plot format same as figure 20.



Figure 22.- S192 composite imagery of lava beds during EREP 20 (bands 20, 19, and 11) at White Sands. Distortion of image is due to conic scans presented as straight lines. Dashed square outlines area shown in enlarged photograph in figure 24.

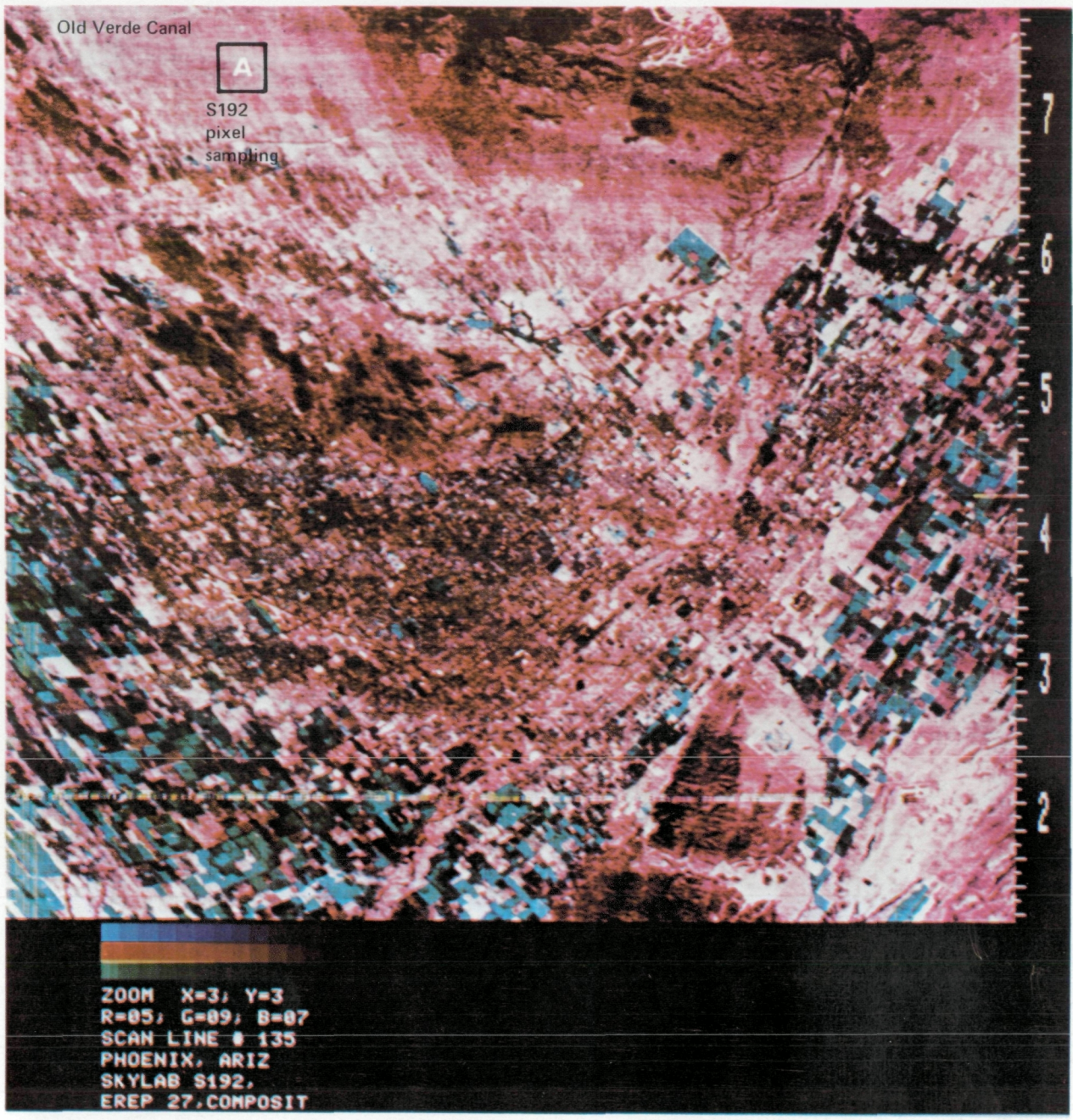


Figure 23.- S192 composite imagery during EREP 27 (bands 5, 7, and 9) at Phoenix. Distortion of image is due to conic scans presented as straight lines. Solid lines outline area of pixel sampling.

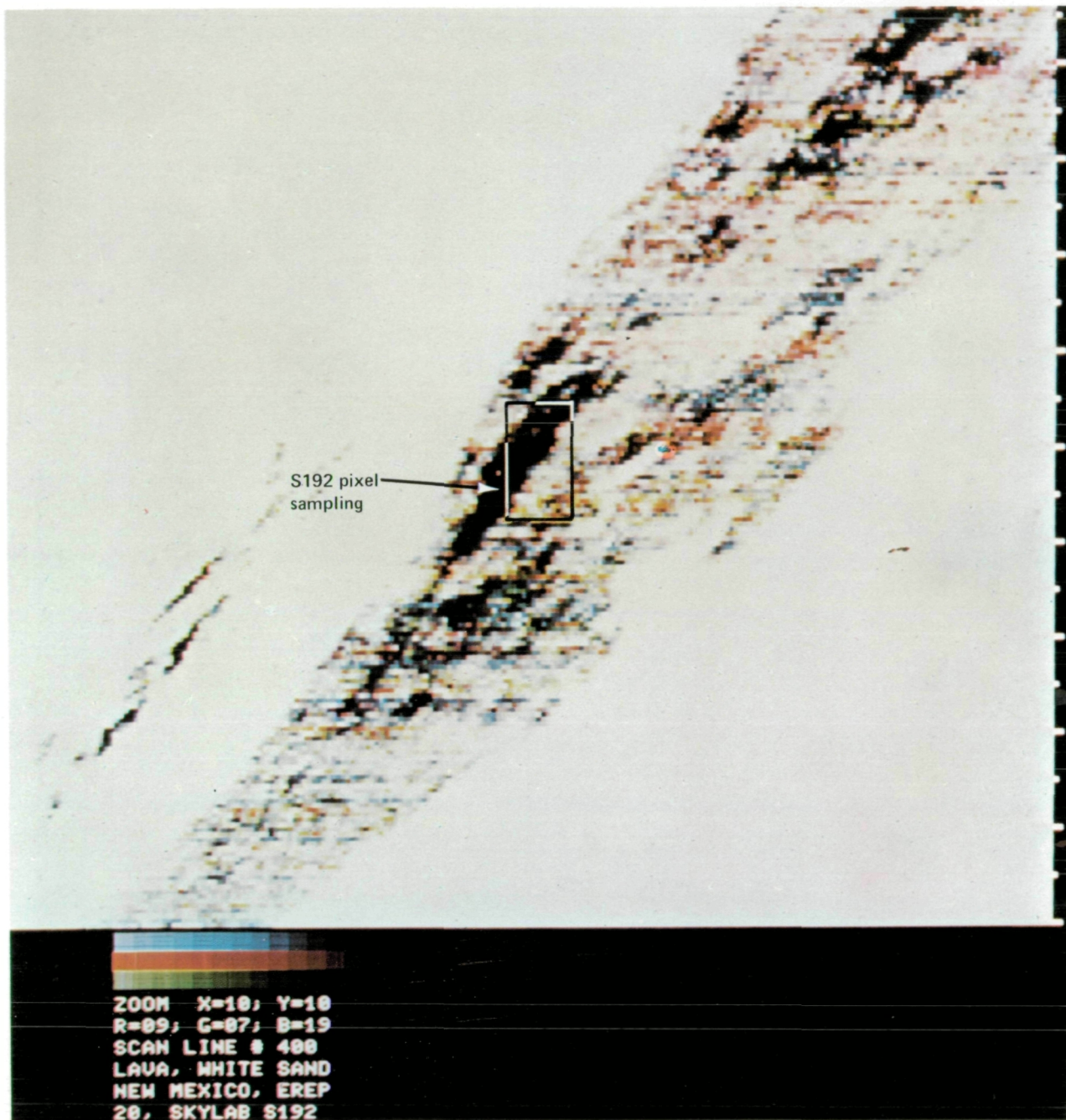


Figure 24.- S192 enhanced and enlarged composite image of lava flow (bands 7, 9, and 19). Solid lines outline area of pixel sampling and S191 targeting.

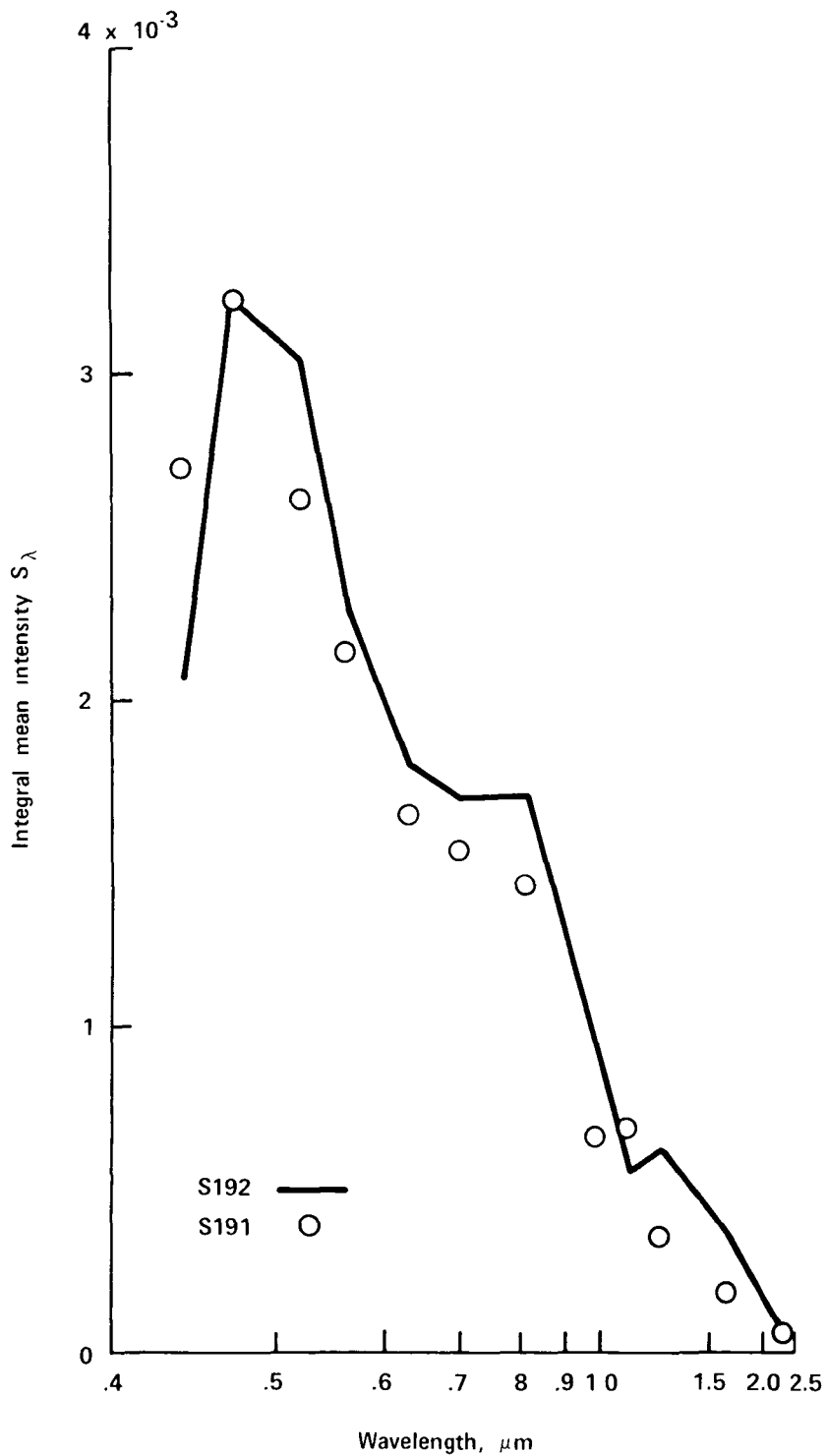


Figure 25.- Comparison of S192 and S191 data by computation of band mean intensity. Data taken from observations of lava at White Sands. Wavelengths are scaled according to wave number.

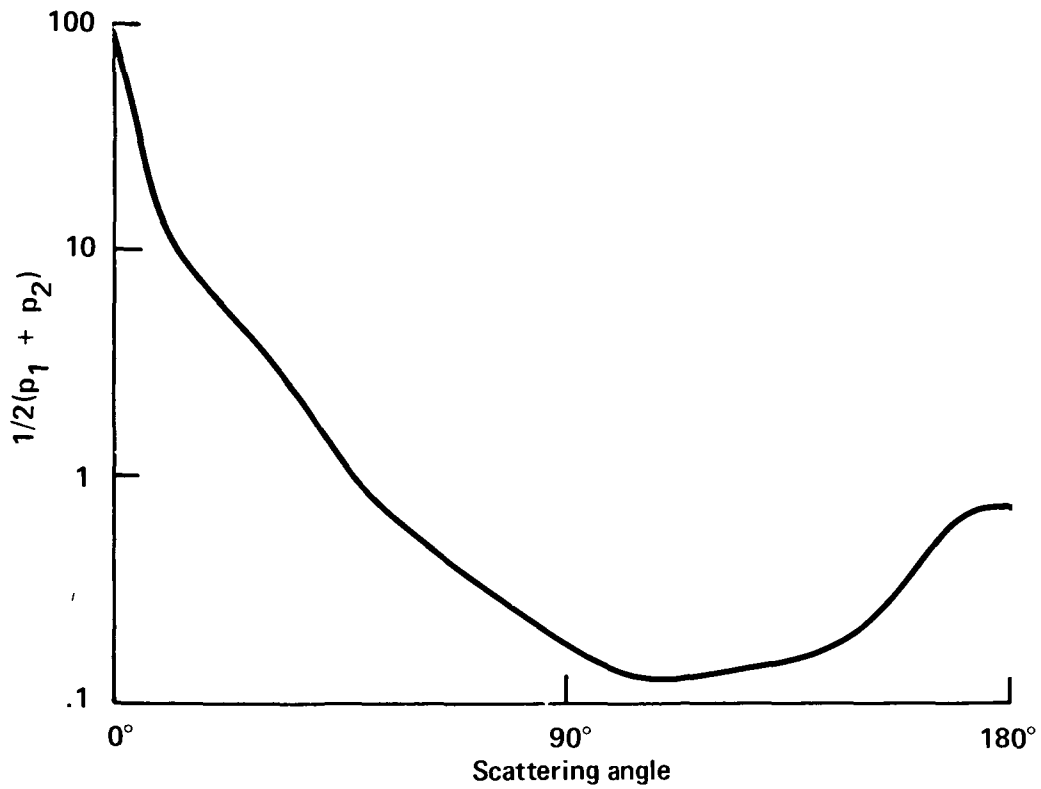


Figure 26.- Typical phase function for continental haze with particle refractive index of 1.55 ($\lambda \leq 0.75$ micrometer) and 1.539 ($0.75 < \lambda \leq 1.0$ micrometer).

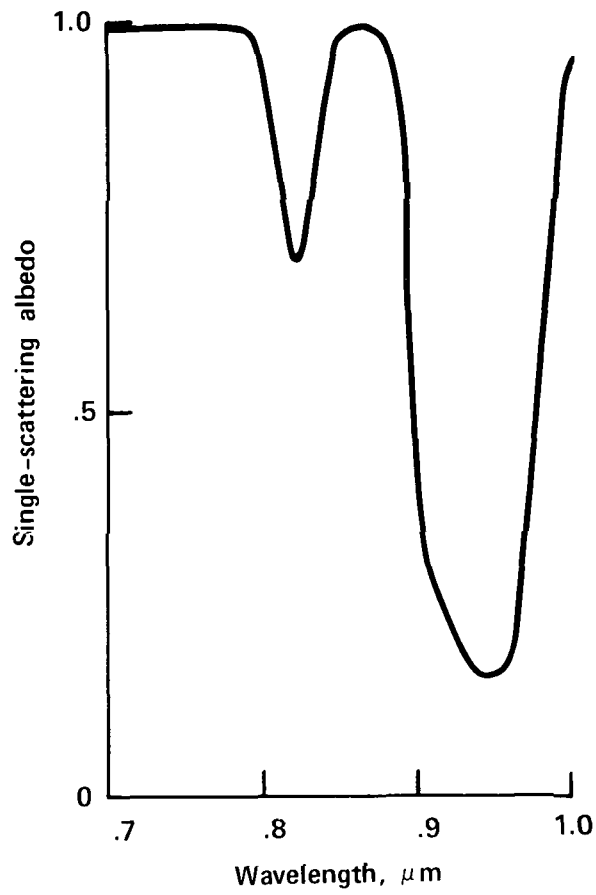


Figure 27.- Example of single-scattering albedo values used in computations.

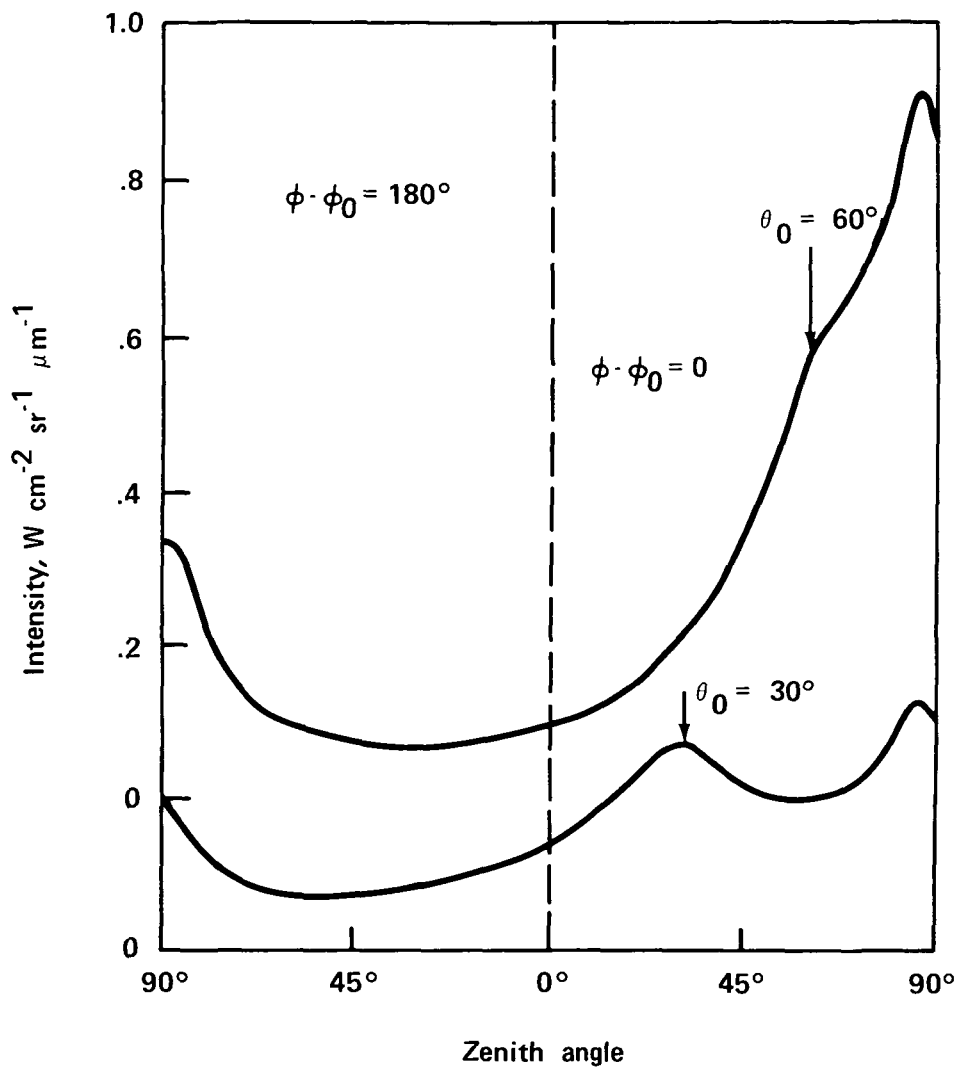


Figure 28.- Intensity of transmitted light in units of $\mu_0 K_0$ for plane containing the azimuthal differences, $\phi - \phi_0 = 0^\circ$ (forward scattering) and $\phi - \phi_0 = 180^\circ$ (backscattering). Plotted are values corresponding to two different solar zenith angles, ϑ_0 . The zero ordinate for $\vartheta_0 = 30^\circ$ is shifted downward for clarity.

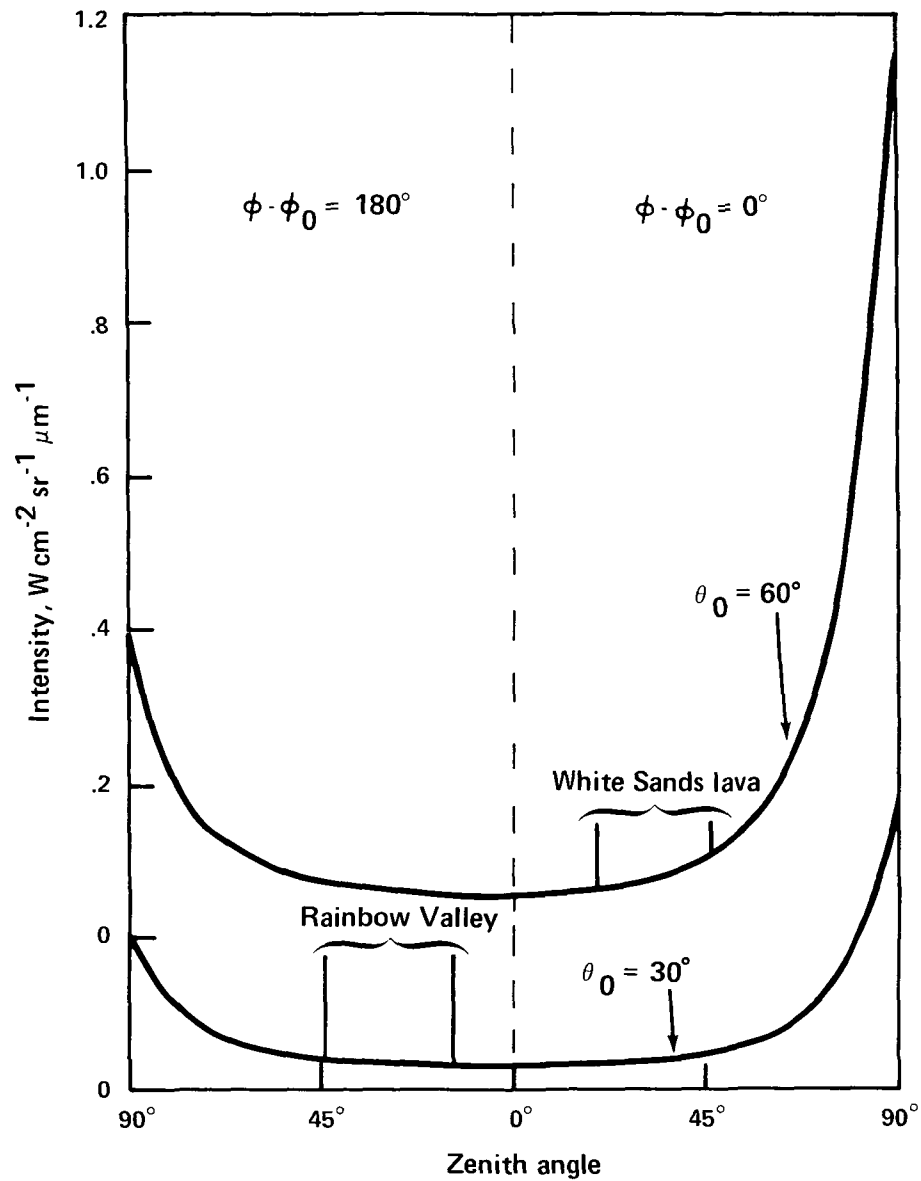


Figure 29.- Intensity of reflected light in units of $\mu_0 K_0$ for planes $\phi - \phi_0 = 0^\circ$ (forward scattering) and $\phi - \phi_0 = 180^\circ$ (backscattering). Plotted are values corresponding to two different solar zenith angles, θ_0 . The zero ordinate for $\theta_0 = 30^\circ$ is shifted downward for clarity.

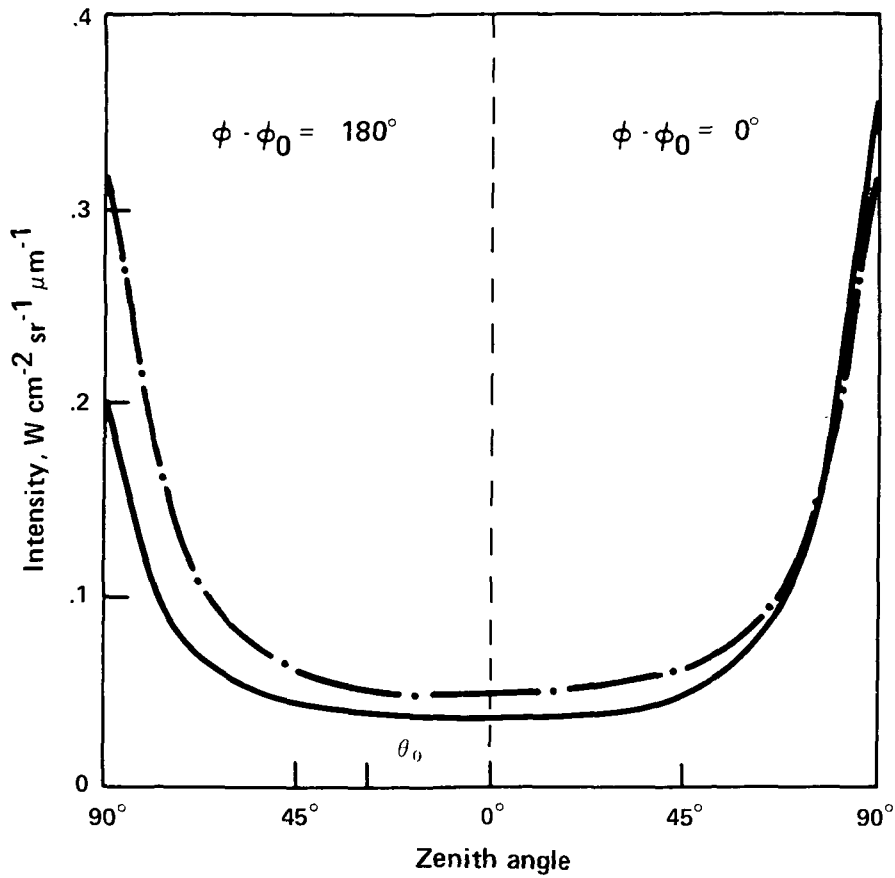


Figure 30.- Reflected intensity for an aerosol of optical depth, $\tau_a = 0.2$ (solid line), compared to that for a composite atmosphere of total optical depth, $\tau = 0.2$ (dot-dashed line); i.e., the layer is composed of a molecular layer ($\tau_r = 0.1$) and an aerosol layer ($\tau_a = 0.1$).

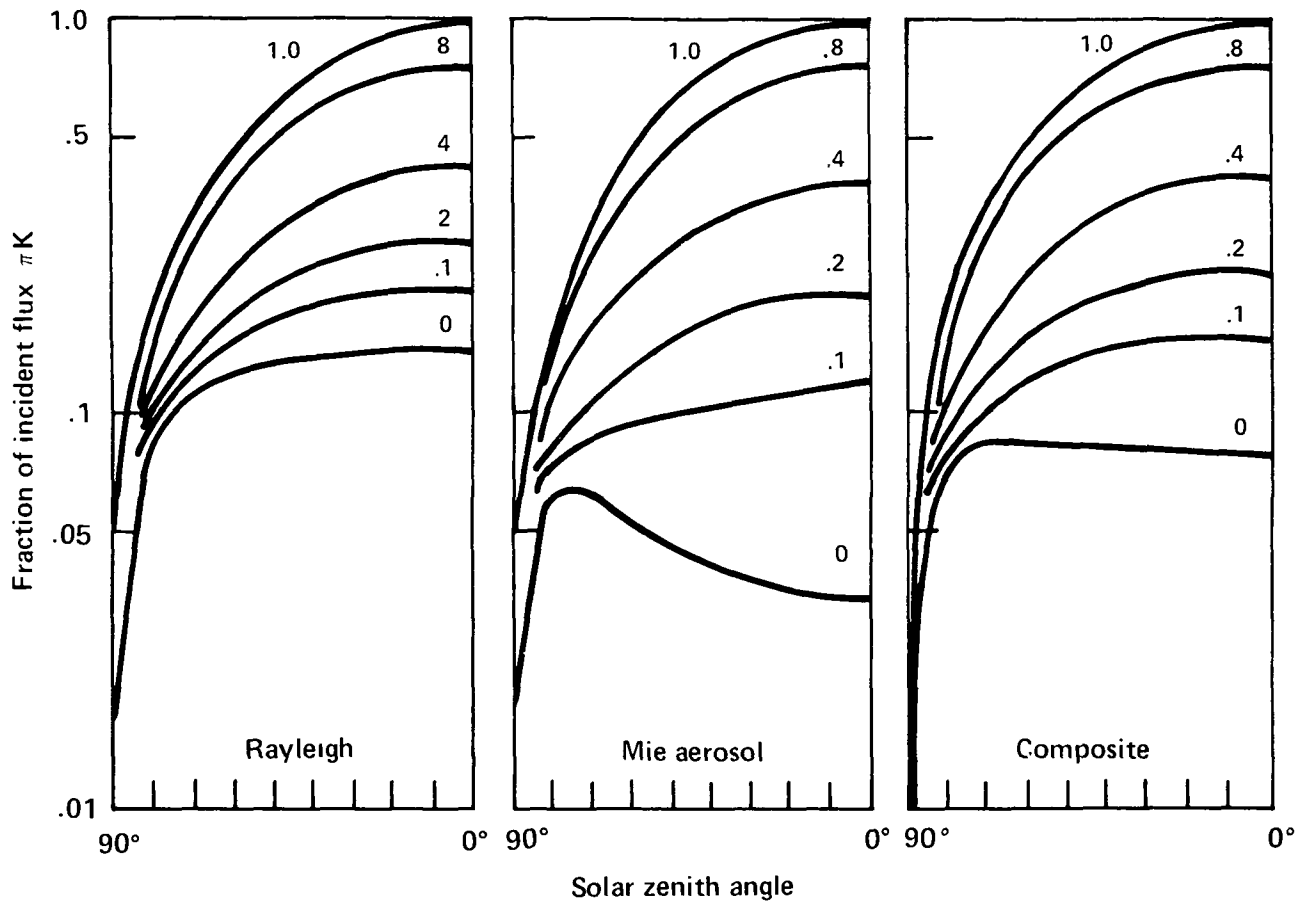


Figure 31.- Fraction of incident flux, πK , reflected for three atmosphere-ground systems. Note the effect of layer composition and varying ground reflectances (numbers on curves).

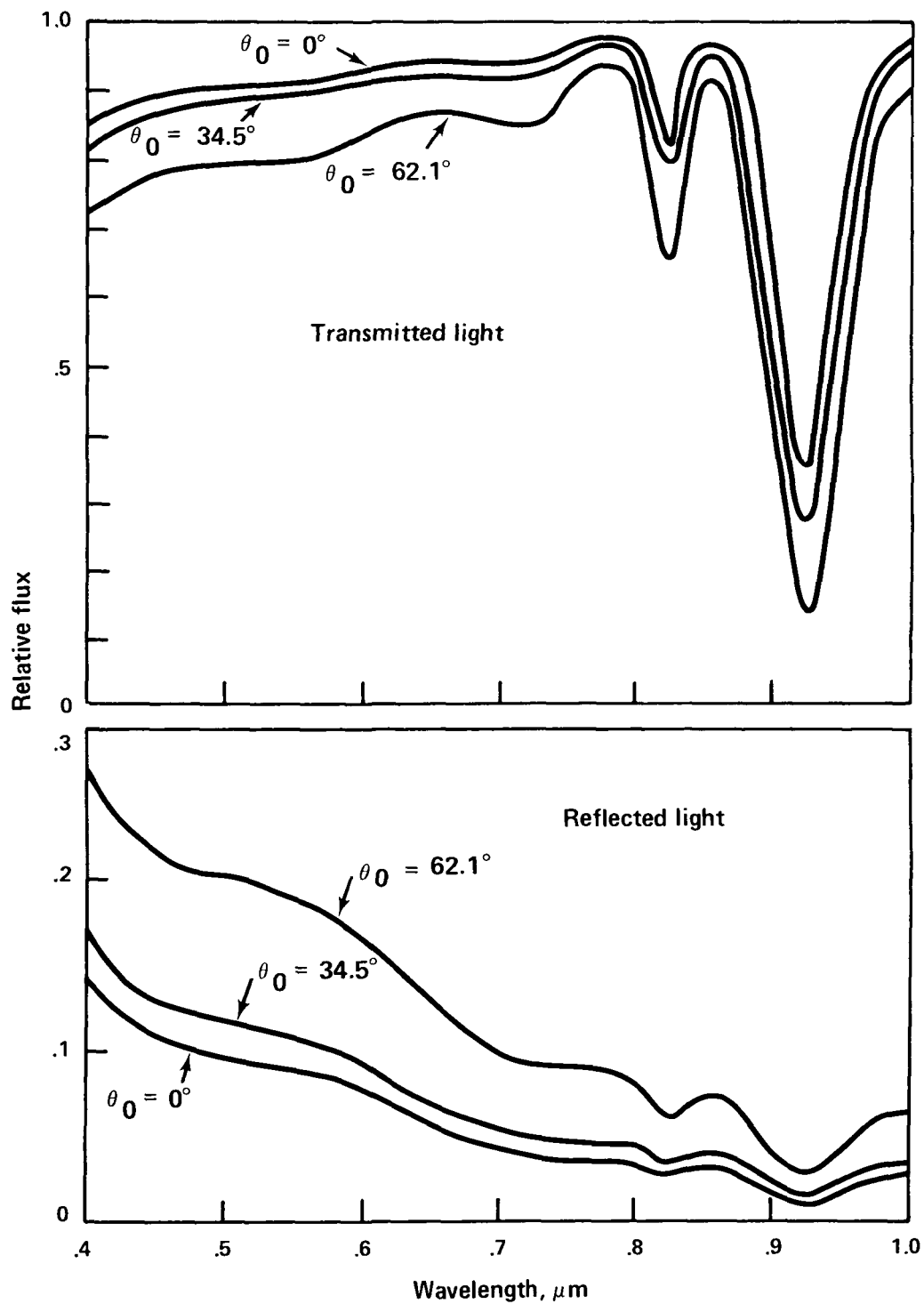


Figure 32.- Computed flux of transmitted and reflected energy for three solar zenith angles, θ_0 , for wavelengths 0.4 to 1.0 micrometer.

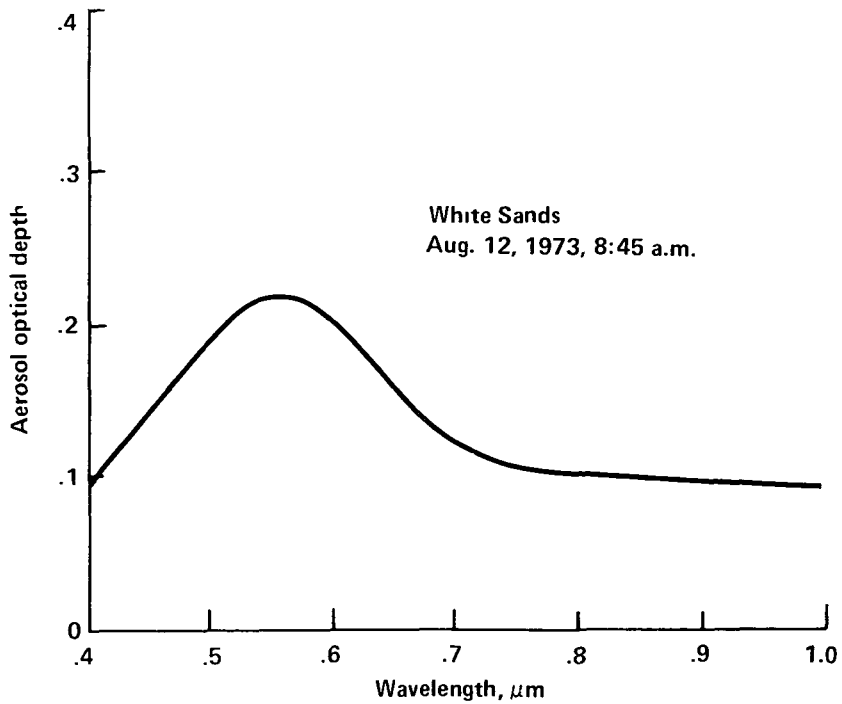
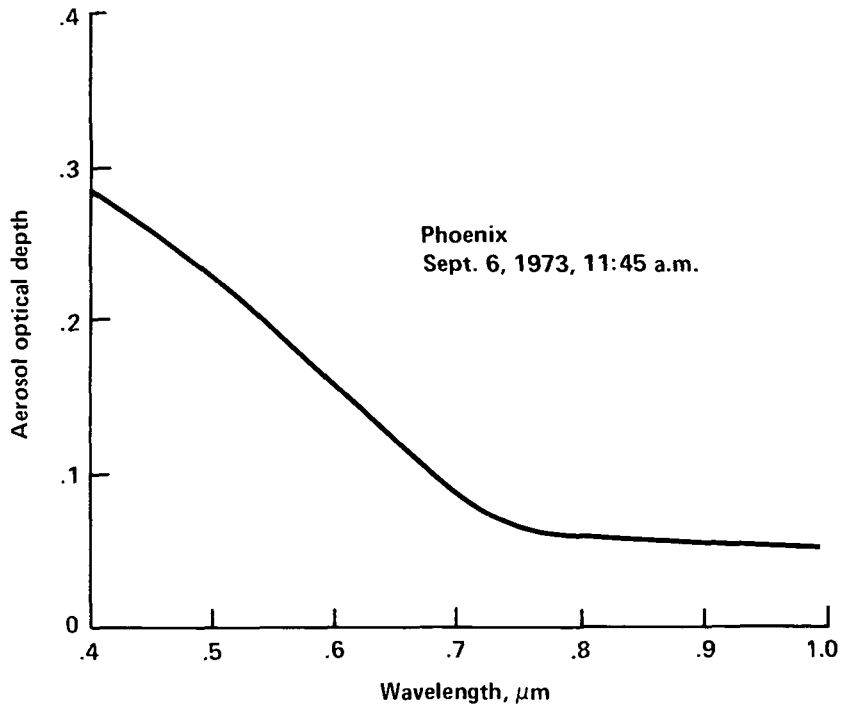


Figure 33.- Measured aerosol optical depths at Phoenix and White Sands for wavelengths from 0.4 to 1.0 micrometer.

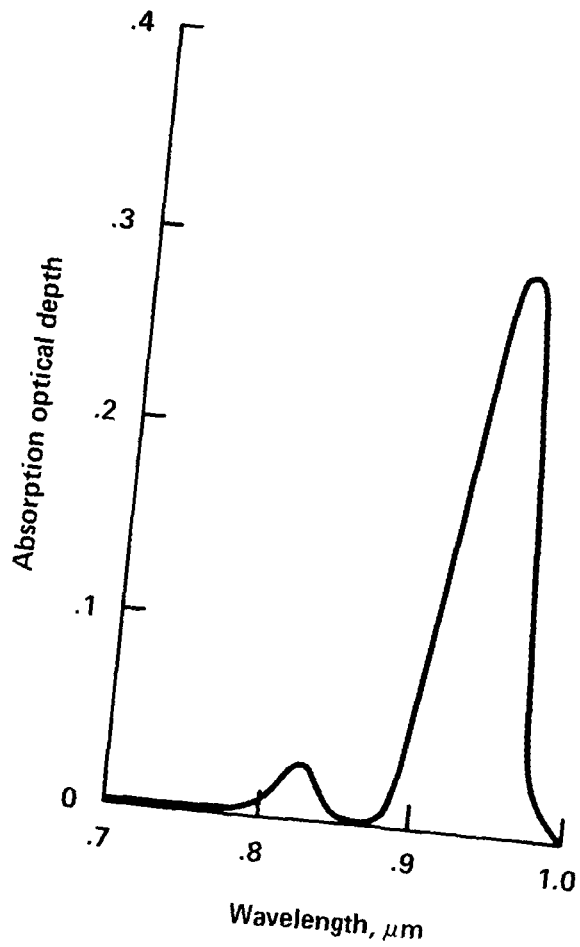


Figure 34.- Example of values of absorption optical depth used in model computations.

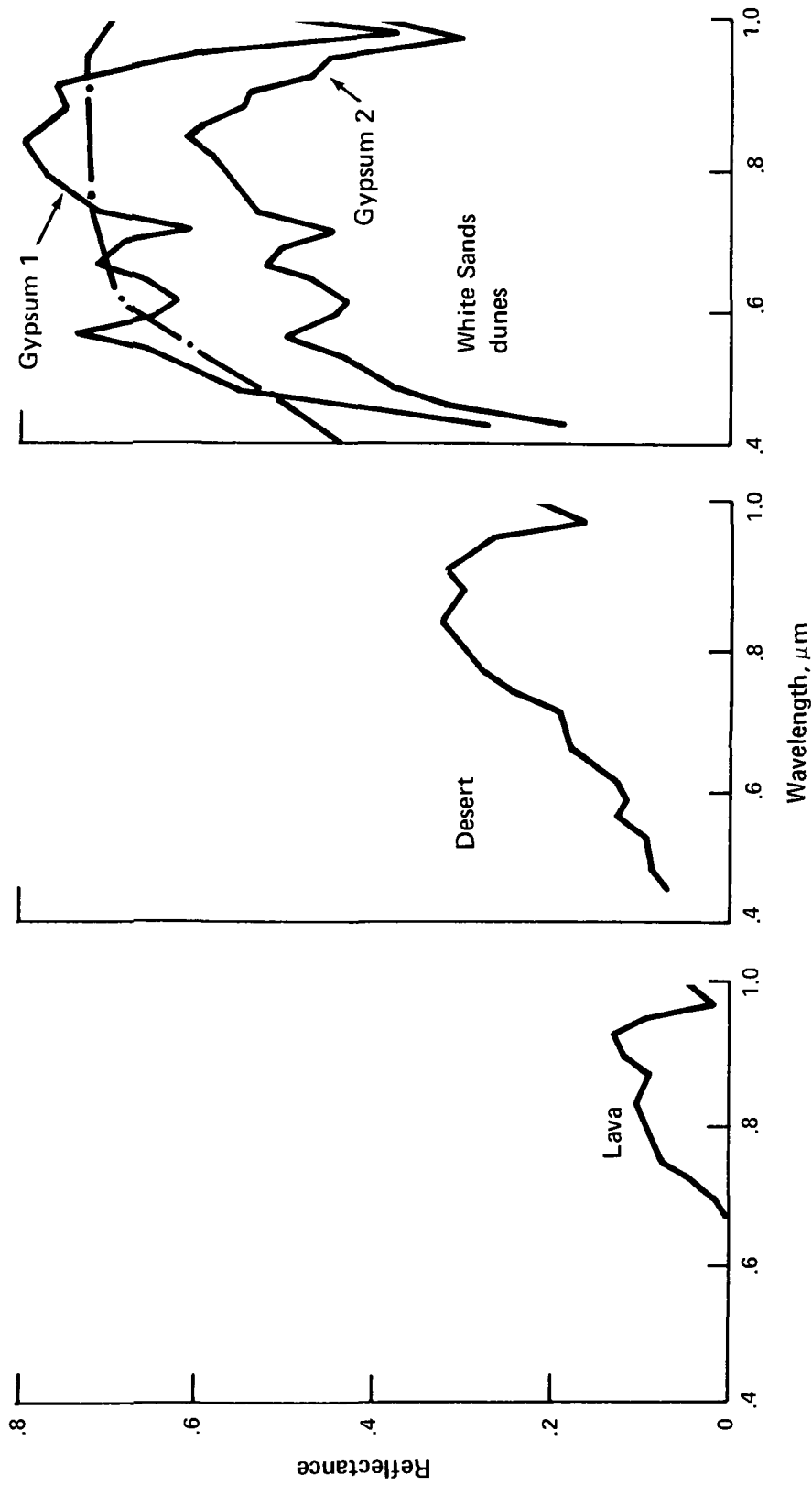


Figure 35.- Reflectances for the White Sands sites computed from S191 data. The dot-dashed curve is the measured reflectance for gypsum (ref. 16).

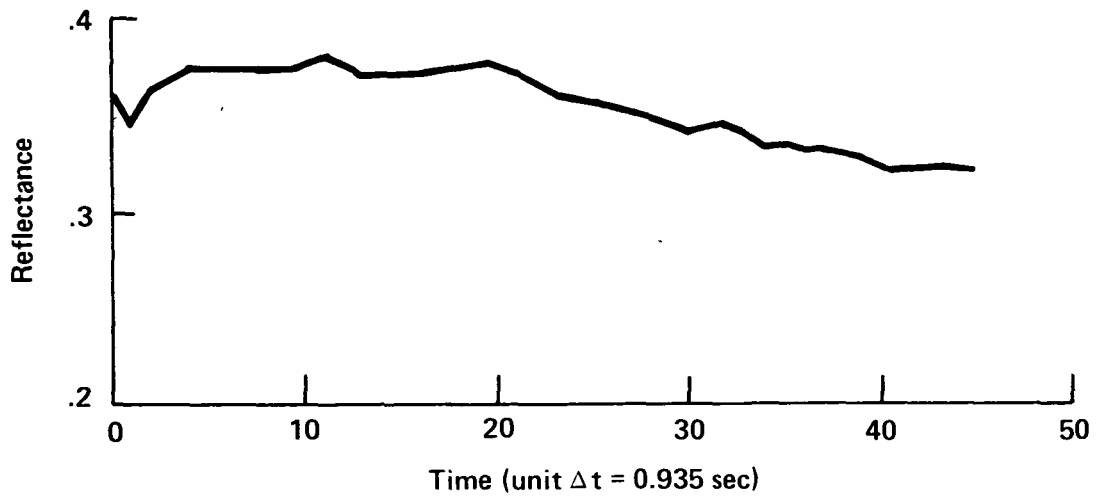


Figure 36.- Time plot of computed surface reflectances from S191 targeting at Rainbow Valley.

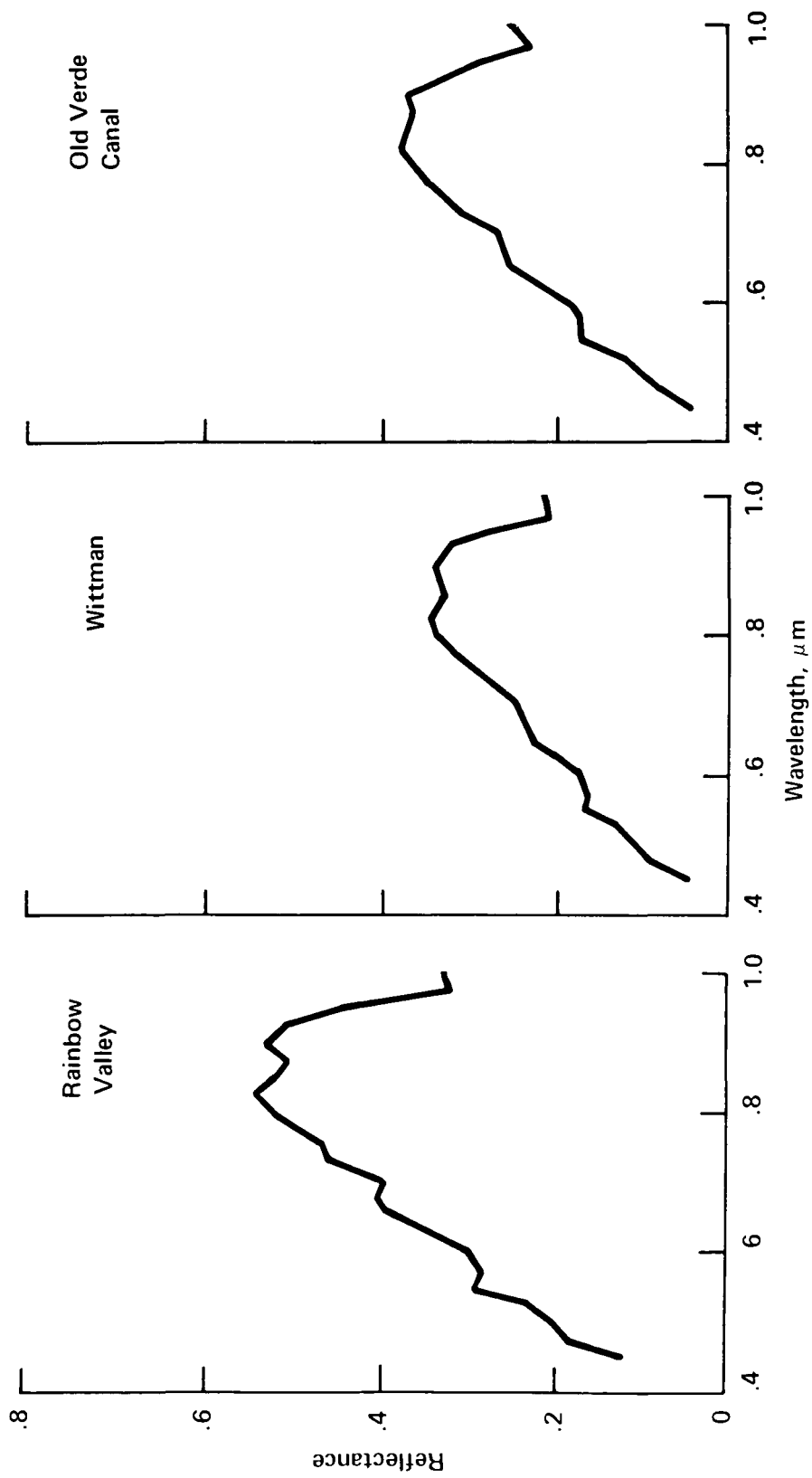
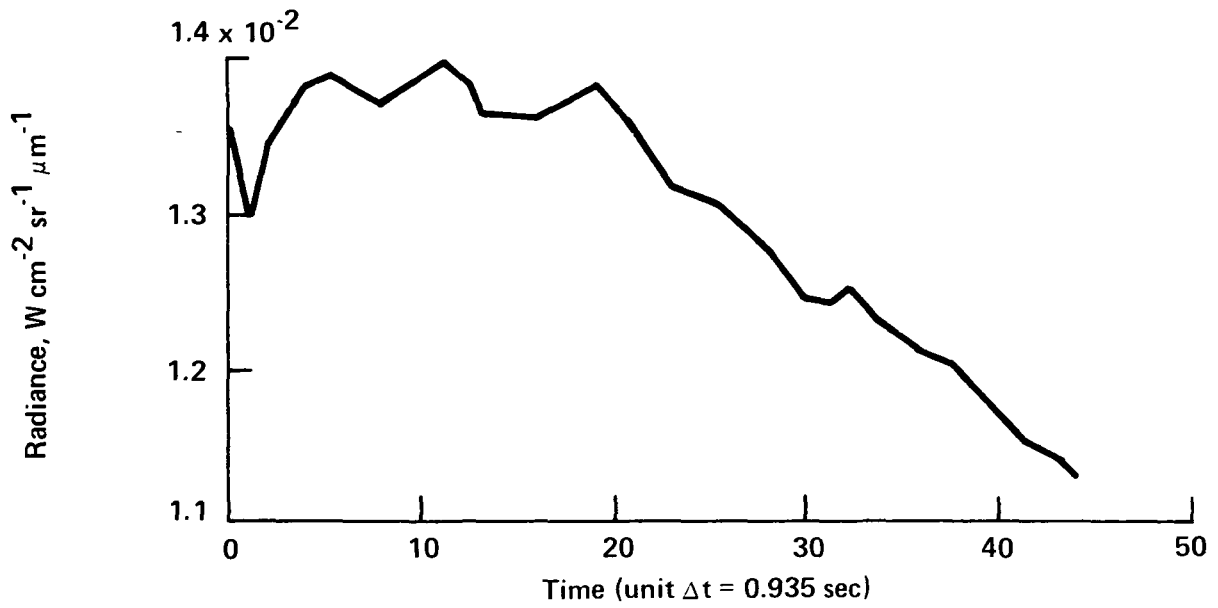
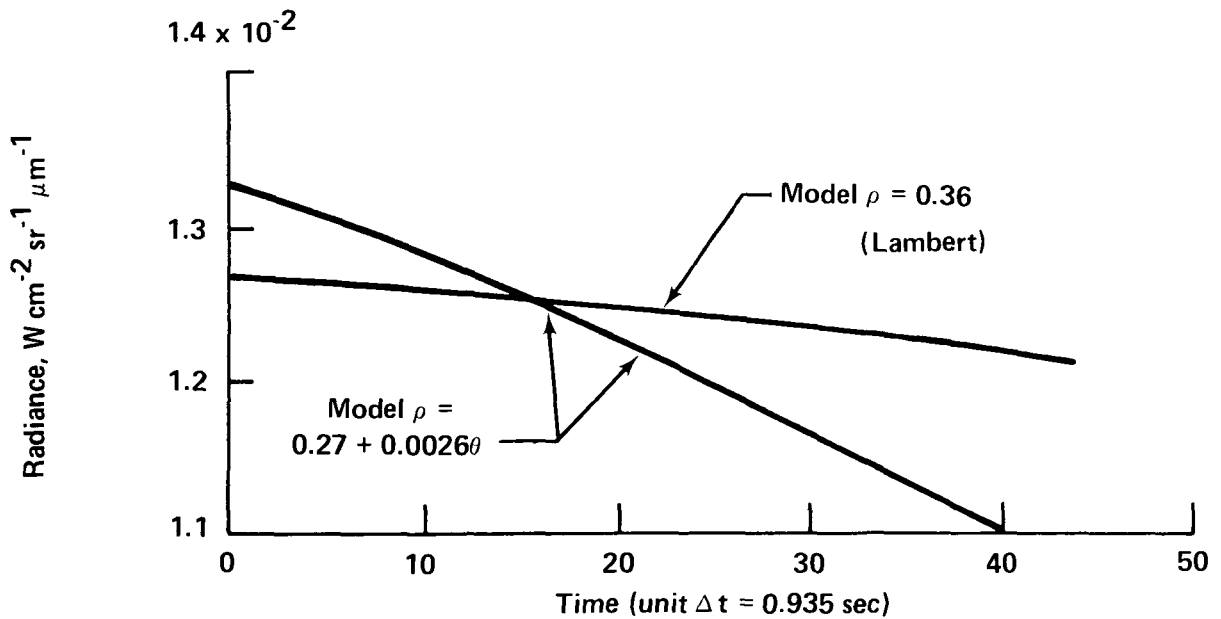


Figure 37.- Reflectances for Phoenix sites computed from S191 data.



(a) Time plot of radiance values.



(b) Radiance values computed from model with ground reflectance of 0.36 and model with ground reflectance of 0.27 plus look angle effect.

Figure 38.- Time plot of S191 radiance values recorded at 0.7 micrometer at Rainbow Valley and radiance values computed from models.

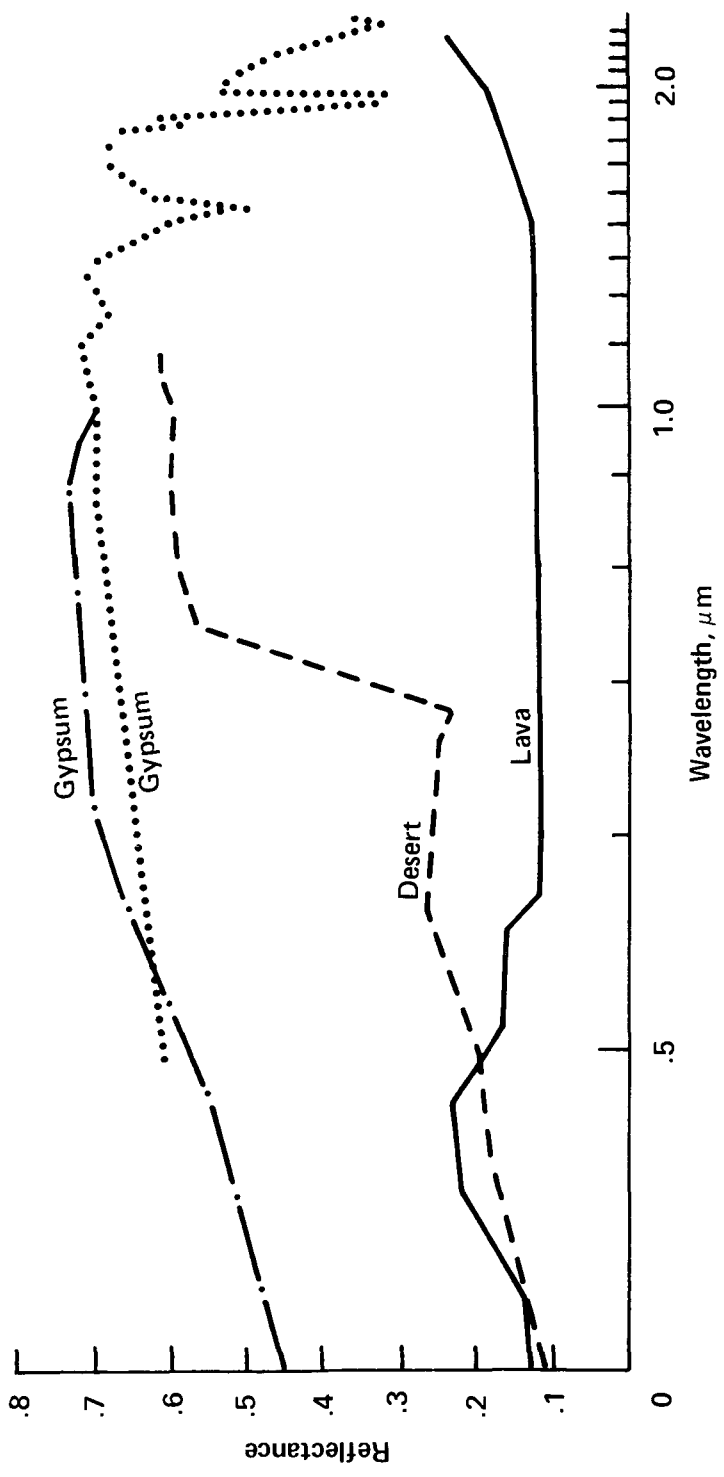


Figure 39.- Spectral profiles for lava, desert, and gypsum (ref. 16).

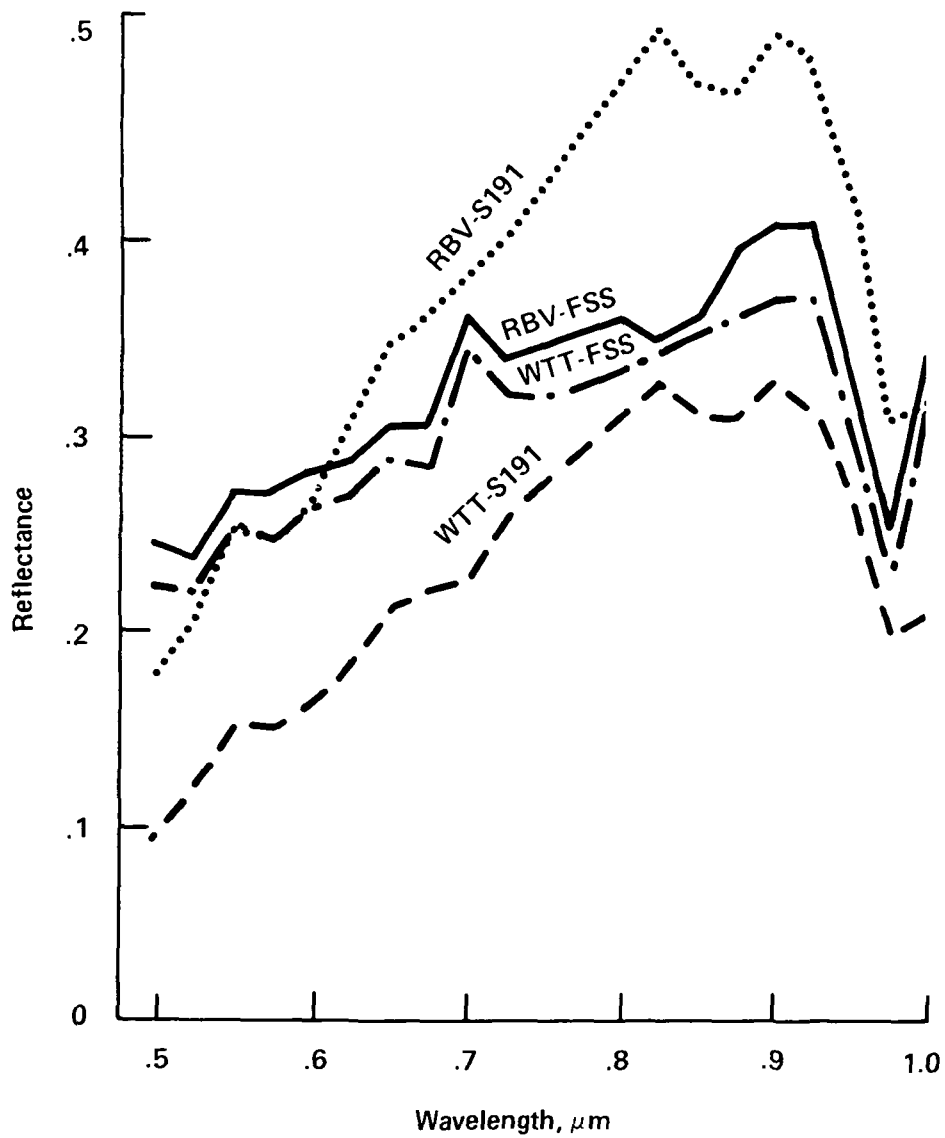


Figure 40.- Comparison of reflectances for Rainbow Valley (RBV) and Wittman (WTT) sites. Computations were made using S191 and FSS data taken at 1524 meters (5000 feet).

APPENDIX

THE TWO-STREAM APPROXIMATION

Flux model approximations are made for two cases: the field spectrometer and the S191 spacecraft spectrometer. These models use the estimate of layer albedo called the "two-stream" approximation of Chu and Churchill as described by Irvine (ref. 15). This is an approximation of radiative flux reflected by a layer of given optical properties.

The albedo of a plane-parallel layer of optical depth τ , single scattering albedo ω_0 , and solar zenith angle μ_0 is

$$R(\tau, \mu_0, \omega_0) = \frac{G \left[1 - \exp(-2s\tau/\mu_0) \right]}{1 - G^2 \exp(-2s\tau/\mu_0)} \quad (19)$$

where $\omega_0 \neq 1$

$$G = \frac{r - s}{r + s}$$

$$r = 1 - \omega_0 f + \omega_0 b$$

$$s = (1 - \omega_0 f)^2 - \omega_0^2 b^2$$

$$b = 1 - f$$

In the case $\omega_0 = 1$

$$R(\tau, \mu_0, \omega_0) = \frac{b\tau/\mu_0}{1 - b\tau/\mu_0} \quad (20)$$

The factor f is the fraction of singly scattered radiation scattered into the forward hemisphere. The factor f may be computed from a phase function Φ (chapter I, ref. 7).

$$f = \frac{1}{2} \int_0^1 \phi(\cos \theta) d \cos \theta \quad (21)$$

or

$$f = \frac{1}{2} \left\{ 1 + \frac{1}{2} \int_0^1 \phi(\cos \theta) \cos \theta d \cos \theta \right\} \quad (22)$$

Future references to the function R (eq. 19) are made with regard to the total optical depth of the layer to which it corresponds instead of the lengthy list of parameters it requires.

The functions for layer A are defined as follows. (See figure 41.)

$$\left. \begin{aligned} R_A(\mu_0) &= R(\tau_0, \mu_0) \\ D_A(\mu_0) &= \exp \left[(\tau_0 + \tau_{\text{abs}}) / \mu_0 \right] \\ T_A(\mu_0) &= \exp(-\tau_{\text{abs}} / \mu_0) - R_A(\mu_0) - D_A(\mu_0) \\ G_A(\mu_0) &= T_A(\mu_0) + D_A(\mu_0) \end{aligned} \right\} \quad (23)$$

Similar functions may be defined for each layer with corresponding optical depths for layers B and C.

The functions defined in the last paragraph correspond to diffuse reflection from $A(R_A)$, direct transmission through $A(D_A)$, diffuse transmission through $A(T_A)$, and total transmission through $A(G_A)$. This last function, $G_A(\mu_0)$, has the same intent as the function $\gamma_1(\mu_0)$ found in Chandrasekhar (ref. 7).

The flux of radiation at the level of the helicopter (field spectrometer) may be given by two components:

1. Incoming skylight and direct sunlight reflected diffusely by layer C

2. Incoming skylight and direct sunlight transmitted by layer C to the ground, reflected there, and again transmitted by C to helicopter level

Incoming diffuse and direct light at the helicopter level is given by

$$F_1 = T_A(\mu_0)G_B(1) + D_A(\mu_0)T_B(\mu_0) + D_A(\mu_0)D_B(\mu_0) \quad (24)$$

Here $G_B(1)$ is the total transmission of a flux normally incident on layer B.

For convenience we shall define the functions

$$\text{Diff}(F_1) = \text{diffuse part of } F_1 \quad (25)$$

and

$$\text{Dir}(F_1) = \text{direct part of } F_1 \quad (26)$$

These functions may be found, practically, by selecting those terms of the flux of F_1 having diffuse factors; e.g.,

$$\text{Diff}(F_1) = T_A(\mu_0)G_B(1) + D_A(\mu_0)T_1(\mu_0) \quad (27)$$

and terms having purely direct factors; e.g.,

$$\text{Dir}(F_1) = D_A(\mu_0)D_B(\mu_0) \quad (28)$$

Component 1 has as its complete expression

$$F_2 = \text{Diff}(F_1)R_C(1) + \text{Dir}(F_1)R_C(\mu_0) \quad (29)$$

The second component ρF_x is given by

$$\rho F_x = \rho [\text{Diff}(F_1)G_C(1) + \text{Dir}(F_1)G_C(\mu_0)] \quad (30)$$

where ρ is the Lambert ground reflectance.

The relative intensity of the radiative flux at the helicopter altitude with the incoming solar flux πK is estimated by

$$\pi I_H = \pi \mu_0 K (F_2 + \rho F_x) \quad (31)$$

Solving this expression for ρ , a formula is obtained for estimating the reflectance of the ground:

$$\rho = \frac{I_H / \mu_0 K - F_2}{F_x} \quad (32)$$

In the case of the S191 spacecraft spectrometer, all model references are made to figure 42, where the ground is assumed to lie under layer B. The three components of radiative flux using the S191 spectrometer are

1. Light diffusely reflected from layer A
2. Light diffusely and directly transmitted by layer A, reflected diffusely by B, and transmitted upward by A
3. Light diffusely and directly transmitted by layer A then layer B, reflected diffusely by the ground and transmitted diffusely by B then A upward to the spectrometer

The expression for the estimated ground reflectance is

$$\rho = \frac{\left[I_{S191} / \mu_0^k - R_A(\mu_0) - F_1 \right]}{F_2} \quad (33)$$

where

$$F_1 = G_A(1) \left[R_B(1) T_A(\mu_0) + R_B(\mu_0) D_A(\mu_0) \right]$$

and

$$F_2 = G_B(1) G_A(1) \left[T_A(\mu_0) G_B(1) + D_A(\mu_0) G_B(\mu_0) \right]$$

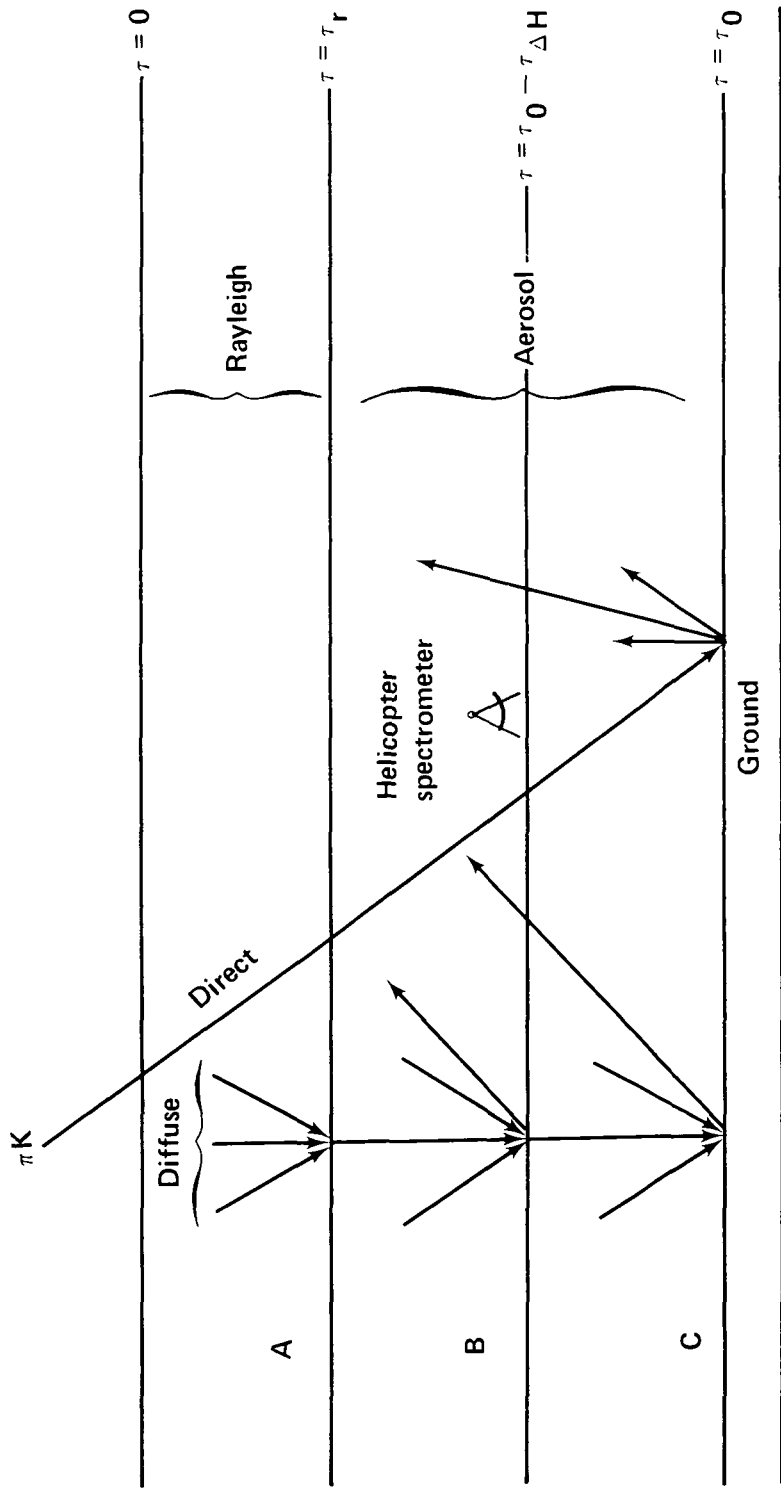


Figure 41.- Two-stream model for helicopter spectrometer.

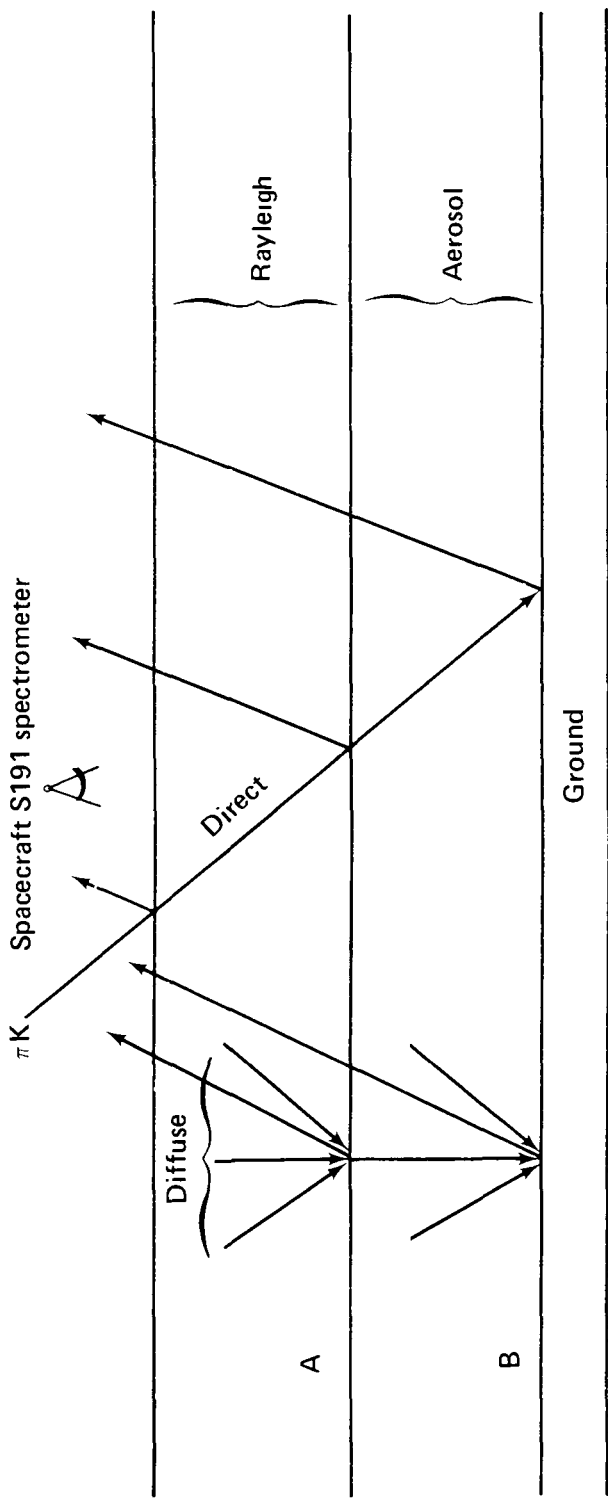


Figure 42.- Two-stream model for spacecraft spectrometer.

REFERENCES

1. Hughes, C. L.: S-191 Sensor Performance Evaluation, Final Report. LEC-5778, Lockheed Electronics Co., NASA Contract NAS 9-12200, June 1975.
2. Potter, A. E.; Williams, C. K.; et al.: Summary of Flight Performance of the Skylab Earth Resources Experiment Package (EREP). Proceedings of the Ninth International Symposium on Remote Sensing of Environment, Vol. III, Environmental Research Institute of Michigan, 1974, pp. 1803-1846.
3. Kuhn, P. M.; Marlatt, W. E.; and Whitehead, V. S.: The Skylab Concentrated Atmospheric Radiation Project, Final Report. NASA CR-144481, Sept. 1975.
4. Marlatt, W. E.; Rainey, D. A.; Reeser, W. K.; and Renne, D. S.: Skylab Concentrated Atmospheric Radiation Project, Executive Summary. NOAA Contract 03-3-022-85, Colorado State Univ. (Fort Collins), Oct. 1975.
5. Pitts, David E.; Lee, J. T.; and Johnson, W.: Remote Sensing of Atmospheric Water Vapor. Sec. 10, Severe Storm Environments: A Skylab EREP Final Report. NASA TM 58184 (in press).
6. Diermendjian, D.: Scattering and Polarization Properties of Water Clouds and Hazes in the Visible and Infrared. Applied Optics, vol. 3, no. 2, Feb. 1964, pp. 187-208.
7. Chandrasekhar, S.: Radiative Transfer. Dover Publications, Inc. (New York), 1960.
8. Van de Hulst, Hendrik Christoffel, ed.: Light Scattering by Small Particles. Wiley and Sons, Inc. (New York), 1957.
9. Diermendjian, D.; Clasen, R.; and Viezee, W.: Mie Scattering With Complex Index of Refraction. J. Optical Soc. America, vol. 51, June 1961, p. 620.
10. Hansen, James E.: Radiative Transfer by Doubling Very Thin Layers. Astrophys. J., vol. 155, Feb. 1969, pp. 565-573.
11. Lacis, Andrew A.; and Hansen, James E.: A Parameterization for Absorption of Solar Radiation in the Earth's Atmosphere. J. Atmos. Sci., vol. 31, Jan. 1974, pp. 118-133.
12. Rainey, David A.; and Marlatt, William E.: Spectral Estimates of Planet Albedo and Comparison to Skylab Observations, Final Report. NOAA Contract 03-3-022-85, Colorado State Univ. (Fort Collins), Aug. 1975.

13. Marlatt, W. E.; and Solomonson, V. V.: Airborne Measurements of Reflected Solar Radiation. Remote Sensing of the Environment, vol. 12, 1971, pp. 1-8.
14. Stevenson, Robert E.; Carter, L. David; et al.: Visual Observations of the Ocean. Skylab Explores the Earth, NASA SP-380, 1977, pp. 287-339.
15. Irvine, William M.: Multiple Scattering by Large Particles; II. Optically Thick Layers. Astrophys. J., vol. 152, June 1968, pp. 823-834.
16. Leeman, Virginia; Earing, Dianne; Vincent, Robert K.; and Ladd, Sharon: The NASA Earth Resources Spectral Information System: A Data Compilation. NASA CR-115757, May 1971.

1. Report No. NASA TM 58208		2. Government Accession No.		3. Recipient's Catalog No.	
4. Title and Subtitle The Skylab S191 Spectrometer Experiment Analysis of Data and Their Applications to the Earth Sciences				5. Report Date July 1978	
				6. Performing Organization Code JSC-13886	
7. Author(s) V. R. Wilmarth, JSC, and D. A. Rainey and W. R. Johnson, Lockheed Electronics Co.				8. Performing Organization Report No.	
9. Performing Organization Name and Address Lyndon B. Johnson Space Center Houston, Texas 77058				10. Work Unit No. 652-01-82-00-72	
				11. Contract or Grant No.	
12. Sponsoring Agency Name and Address National Aeronautics and Space Administration Washington, D.C. 20546				13. Type of Report and Period Covered Technical Memorandum	
				14. Sponsoring Agency Code	
15. Supplementary Notes As an aid to the reader, where necessary the original unit or units of measure have been converted to the equivalent value in the Système International d'Unitès (SI). The SI units are written first, and the original units are written parenthetically thereafter.					
16. Abstract The data in the visible and near-infrared portions of the spectrum as recorded by identical spectrometers on Skylab and on a helicopter are examined to establish the significance of spectral reflectances from the Earth surface as influenced by water vapor, atmospheric gases, and aerosols. Models of radiation transfer show good agreement of theoretical computations and observed measurements.					
17. Key Words (Suggested by Author(s)) Skylab Program EREP Earth Resources Infor- Terrestrial radiation mation System Spectral emission Infrared spectrometers Radiation measurement Spectral reflectance			18. Distribution Statement STAR Subject Category: 43 (Earth Resources)		
19. Security Classif. (of this report) Unclassified		20. Security Classif. (of this page) Unclassified		21. No. of Pages 89	22. Price* \$5.00

*For sale by the National Technical Information Service, Springfield, Virginia 22161

National Aeronautics and
Space Administration

SPECIAL FOURTH CLASS MAIL
BOOK

Postage and Fees Paid
National Aeronautics and
Space Administration
NASA-451



Washington, D.C.
20546

Official Business
Penalty for Private Use, \$300

12 1 10, E, 070778 S00673HU
NORTHROP UNIV
ATTN: ALUMNI LIBRARY
1155 WEST ARBOR VITAE ST
INGLEWOOD CA 90306

NASA

POSTMASTER: If Undeliverable (Section 158
Postal Manual) Do Not Return